Surface Modification of Ti Implant for Enhancing Biotribology and Cells Attachment

Jiajun Luo

A dissertation submitted in partial fulfillment

of the requirement for the degree of

Doctor of Philosophy

of

University College London

Division of Surgery & Interventional Science

University College London

September 5, 2019

Declaration

I , Jiajun Luo, confirm that the work presented in the thesis is my own. Where information has been derived from other sources, I confirm that this has been indicated in the work.

Sign:

Abstract

Implant success strongly depends on the proper integration of bone to biomaterial surface. By the selected retrieval cases, inadequate integration of bone screws was a dominated factor caused failure. The surface modification technology that improve osteointegration by inducing TiO_2 nanotubes (NT) on Ti-based implants has a potential applications in orthopaedic implants. NT generated by anodization method provide a vertically aligned nanotube structure that enhances the integration between bone tissue and implant surface by improving osteoblasts attachment. Although cells to NT is positive, the mechanical weakness of NT has also been well-documented and is an obstacle to its applications.

The thesis comprise a detailed method to improve NT mechanical stability, by introducing an interfacial bonding layer at NT bottom and Ti substrate, and retaining vertically aligned nanotubes. The physicochemical properties of this structure optimized TiO_2 nanotubes (SO-NT) was systematically characterized, the SO-NT has been demonstrated with improved biotribological and biocorrosive performance. The uniform hyperfine interfacial bonding layer with nano-sized grains exhibited a strong bonding to NT layer and Ti substrate. It was observed, the layer not only effectively dissipates external impacts and shear stress but also acts as a good corrosion resistance barrier to prevent the Ti substrate from corrosion. The SO-NT modified bone screw has also demonstrated with enhanced fretting corrosion resistance than NT and pristine Ti_6Al_4V on screws.

Since the elongated osteoblasts were observed on NT and SO-NT compared with Ti surface, the nanotubes structure has been shown with promoting of osteoblasts attachment. However, the mechanism of cell nanotubes interactions are largely in controversial. In order to reveal the cell-nanomaterial interactions, nanotopographies including Nanoconvex, Nanoconcave and Nanoflat were generated and characterized to evaluate the cell initial attachment behaviour. Human osteoblasts were observed with spindle shape on Nanoconcave, cells on Nanoflat were well-spreading but in sphere shape, while the osteoblasts on Nanoconvex were with the minimum spreading areas. Cell-materials interface is mediated and influenced by the adsorption of ECM on nanomaterials. Thus, a novel fibronectin adsorption model was proposed by calculating Coulomb's force to illustrate the interact mechanism between protein and material that influence cell behaviours.

The achievements of thesis are;

1. Retrieval analyzed two cases of implants failure and pointed out one of dominated failure factor, the lack of osteointegration.

2. Introduce the interfacial bonding layer that significantly improve the biotribological and biocorrosive performance of NT, and generated SO-NT.

3. Systematically evaluated the biotribological performance of Ti, NT and SO-NT, and propose a novel methodology to quantify the fretting degradation on bone screws.

4. Propose a novel model to estimate the fibronectin adsorption on Nanoflat, Nanoconvex and Nanoconcave by the Coulomb's force calculation.

Impact Statement

Infection and aseptic loosening are two major factors lead to implant failure. These two factors have different mechanisms, one reason is the lack of osteointegration. This work was dedicated to research next generation implant surface–nano featured surface technique, to avoid orthopaedic implant failure. The impacts of this work have shown below;

1. Developed a nanofeatured surface technology (SO-NT) could be applied on implant. The SO-NT is featured with improved biotribological performance, which can extend the service longevity of orthopaedic implant and decrease the revision of failed implants.

2. Expand the knowledge of cell-material interactions. An ECM-nanomaterial interaction model was proposed to estimate the interaction between protein and nanomateirals, this model is valuable to reveal cell responses to biomaterials.

This work is dedicating to develop novel healthcare technologies to improve quality life of patient, and improve the understanding of cell-materials interactions.

Acknowledgement

Time flies, until I started writing this part, I still do not realize that my Ph.D life is coming to end. During the past four years, I have obtained numerous kindly help from people around me. Firstly, I would like to express my sincere gratitude to my supervisor Prof. Chaozong Liu for the continuous support during my Ph.D study. In particular, he has developed my independent research skills which are the most important ability for academic scholar life. Besides my first supervisor, I would like to thank my second supervisor, Prof. Anne Young who spend much time to guide and help me, especially for my poor academic writing skills.

My sincere thanks also goes to Prof. Feng Zhou Dr. Shuanhong Ma and Prof. Wenhui, who provided me an opportunity to join their team as intern, who gave access to the lab and facilities. Without these supports it would not conduct this thesis.

I also need to thank my lab mates cooperated with me, we worked together in lab and have fun in life. They are Dr. Sara, Dr. Maryam, Dr. Sammy, Dr. Elena, Mr. Ziyu, Ms. Yingying, Mr. Jianshu, Mr. Ata, Prof. Xiangsheng and Mr. Shudong.

Finally, I would like to thank my parents who give me continuously spiritual supporting and sponsored my all over cost during Ph.D. I also want to Siqi who gave me love and support, for all late night and early morning, thank you for being my best friend.

Table of content

List of Figures

pristine screws (A) and retrieval screws discoloration located on both shaft and thread areas (B)

Figure 3. 3 Schematic images of insertion wear, schematic illustration of insertion wear mechanism at thread tip (A), SEM images of wear scar on the threads tip (B) and (C), optical image and EDX analysis of thread tip on area a and b, (D, D1 and D2)

Figure 3. 4 Fretting corrosion wear scars, a, a1, a2 and b, track formation, c

Figure 3. 5 Fretting corrosion morphology features on screw 1 and 2 shinny (burnished) areas, screw 1 widely distribution (A) and specific features on screw 2, (A1) and (A2)

Figure 3. 6 Stress corrosion on screw 3, Optical image (A), SEM images of stress corrosion areas (A1 and A2), and chemical composition of area a and b (B-a and B-b).

Figure 3. 7 Comparative SEM images, stress corrosion topography featured with angel edge cracks (A) and fretting corrosion topography (B)

Figure 3. 8 CT scan images of internal plate and screws fixator inserted in right femur in patient, by as inserted, after healing 14 months and before 19 months retrieval. Femur fracture area is marked with white arrow, and the fractured screw is marked with red arrow

Figure 3. 9 Optical image of as-retrieved screws and plate fixation system, fracture screw (red arrow), breakage screw part thread was locked with plate thread (white arrows)

Figure 3.10 The SEM images of fracture topography. Shear applied from femur to knee, the opposite direction z axis, shown in a. The initial fracture area (b), magnified

fracture topography shown typical fatigue breakage (c). Breakage end topography with step topography, magnified step and worn areas, marked with black arrows (d)

Figure 3. 11 SEM images of worn areas. Worn areas are widely distributed at fracture surface (a), the magnified image of disorder arranged wear tracks, and the longest track (black arrows), approx 100 μm (b). Worn areas in other locations (c), order arranged wear track (d)

Figure 3. 12 Cracks were observed on the femur side of broken screw head. The crack generated and extent along with thread root (a), detailed image of crack (b), tiny fatigue cracks were arranged adjacent the fracture surface (c) and magnified image of fatigue crack (d)

Figure 3. 13 Finite element analysis (FEA) model shows the mesh of screw (a), and conditions of FEA, 800 N equivalent force applied on the area close to plate and inside the bone. Fixed support was imposed on the surface of the screw head.

Figure 3. 14 FEA shows the stress distribution on the screw (a), the maximum value of stress exhibits 1141.5 MPa at thread root on bond area of head and screw (b) and section view of stress concentration (c)

Figure 3.15 Image of longest consecutive wear scar on the fracture surface with 110-120 μm in length (a), the magnified image of the wear scar (b) and FEA elastic strain with 0.01mm in maximum value of fracture surface

Figure 4. 1 The optical image of TiO_2 nanotubes (NT and SO-NT) and nanotubes structure top view

Figure 4. 2 TiO_2 nanotubes (NT) cross section view

steel ball

Figure 5. 8 Friction coefficient of NT with 2000 cycles countering stainless steel ball

Figure 5. 9 Friction coefficient of Ti with PTFE ball on disk (7 × 1000 cycles) and magnified coefficient from 1800-1900 cycles

Figure 5. 10 Friction coefficient of NT with PTFE ball on disk (7 × 1000 cycles) and magnified coefficient from 1800-1900 cycles

Figure 5. 11 Friction coefficient of SO-NT with PTFE ball on disk (7 × 1000 cycles) and magnified coefficient from 1800-1900 cycles

Figure 5. 12 Optical image of pristine Ma, NT and SO-NT screws (a1), after fretting (a2) and thread image after fretting b1 machined, b2 NT and b3 SO-NT

Figure 5. 13 Morphology after fretting on drill tapping plane, Ma screw a1 and a2, NT screw b1 and b2, SO-NT screw c1 and c2

Figure 5. 14 Each SEM observation point on thread of machined (Ma 1-5) NT (NT 1-5) and SO-NT (SO-NT 1-5) screw, bar=300 μm

Figure 5. 15 Lift off areas of nanotubes layer on thread for NT and SO-NT decorated screw, ＊＊, $p<0.01$. p value: 0.0051, Error bars represent standard error with the mean (s.e.m)

Figure 5. 16 Thread width measure point (white bar areas) of Ma(a), NT(b) and SO-NT(c), bar=300 μm

Figure 5. 17 Thread width of Ma, NT and SO-NT after fretting, ＊, $p<0.05$, ＊＊, $p<0.01$, ＊＊＊, $p<0.001$.

Figure 5. 18 Open circuit potential of Ma, NT and SO-NT before and after fretting (a)

Figure 6. 6 Osteoblast cell morphological characterization of spreading on Ti, NT and SO-NT for 24 h and 72 h

Figure 6. 7 Topographical characterization of Nanoflat, Nanoconvex and Nanoconcave. a, arrangement of nanoflat, nanoconvex and nanoconcave surfaces by SEM. b, Three-dimensional illustration of nanoflat, nanoconvex and nanoconcave surfaces by AFM. c, Sectional dimensions of three topographies. d, Based on AFM section measurement, the statistical dimensions of nanoflat (height), each nanoconcave subunit (height and width) and each nanoconcave subunit (height and width). e, Surface area of nanoconvex and nanoconcave surfaces)

Figure 6. 8 Topographies of Nanoflat, Nanoconvex and Nanoconcave and corresponding surface charge. a, AFM topographical characterisation of nanoflat, nanoconvex and nanoconcave. b, Surface potential distribution measured by Kelvin probe force microscopy (KPFM). c, Sectional potential distribution in relative value on nanoflat, nanoconvex and nanoconcave surfaces. d, The absolute potential difference on each subunit of nanoflat, nanoconvex and nanoconcave surfaces. e, Schematic illustration of correlation between topography and surface potential distribution on nanoconvex and nanoconcave surfaces

Figure 6. 9 The calibrated with HOPG absolute surface potential value of Nanoconvex

Figure 6. 10 The calibrated with HOPG absolute surface potential value of Nanoconcave

Figure 6. 11 Actin (red), vinculin (green), and cell nucleus (blue) fluorescence images of osteoblasts after culture 3 h. a, cytoskeleton arrangement. b, c, d, e, f and g,

List of Tables

Abbreviation

Ti	Titanium
HAp	Hydroxyapatite
Ca	Calcium
AMP	Antimicrobial peptides
NT	TiO_2 nanotubes
MSC	Mesenchymal stem cells
EG	Ethylene glycol
FTIR	Fourier-transform infrared spectroscopy
BIC	Bone implant contact
hMSCs	Human mesenchymal stem cells
Osx	Osterix
ALP	Alkaline phosphatase
COL 1	Type 1 collagen
TRAP	Tartrate-resistant acid phosphatase
TEM	Transmission electron microscope
BMP2	Bone morphogenetic protein 2
TNF-α	Tumour necrosis factor α
SO-NT	Structure optimised TiO_2 nanotubes
SEM	Scanning electron microscopy
EDX	Energy dispersive X-ray spectroscopy
XRD	X-ray diffraction
XPS	X-ray photoelectron spectroscopy
DI water	Distilled water
HV	Hardness vickers
FE	Finite-element
THA	Total hip arthroplasty
ALVAL	Aseptic lymphocytic vasculitis associated lesion
ARMD	Adverse reactions to metal debris
VL	Volume loss
COF	Coefficient of friction
OCP	Open circus potential
SBF	Simulated body fluid
DHS	Dynamic hip screw
PMMA	Polymethylmethacrylate
LCP	Locking Compression Plate
ESR	Erythrocyte sedimentation rate
CRP	C-reactive protein
AVN	Avascular necrosis
ASD	Anodic spark deposition
MAO	Micro arc oxidation

Ma screw	Machined surface screw
ECM	Extracellular matrix
RGD	Arginine, glycine and aspartic acid
FAK	Focal adhesion kinase
ROCK	Rho-associated protein kinase
EBL	Electron beam lithography
NSQ50	Nanopits on silicon surface with 120 nm in diameter and 100 nm in depth with a randomly displacement in ± 50 nm
FBS	Fetal bovine serum
KPFM	Kelvin probe force microscopy
AFM	Atomic force microscopy
HOPG	Highly oriented pyrolytic graphite
PBS	Phosphate buffered saline

Chapter 1

1. Introduction

1.1 Titanium applications in orthopaedic implant

Orthopaedic implant used for joint replacement has been on rise, with significant increases still projected over the next 15 years [1]. Driven largely by the aging population and patient's desire to maintain an active lifestyle, the global orthopaedic market was valued at $52.7 billion/year in 2017. The Global Data expects that this market will grow to $66.3 billion/year in 2023 at a steady compound annual rate of 3.9% [2].

In orthopaedic and dental medical device applications, commercial pure titanium and its alloys are widely used for many implant to replace human tissue, such as artificial hip joint, artificial knee joint, artificial bone disk, screws and other artificial implants [3]. Owing to the formation of TiO_2 film on titanium (Ti), which features excellent corrosion resistance, Ti is considered to be an excellent biomaterial. Ti and its alloys are the most common materials for orthopaedic application and are classified as having high biocompatibility, are bio-inert and do not induce allergies when implanted into the human body [4, 5].

Johansson et al. noted that TiO_2 film can exhibit different behaviour than metallic biomaterials such as CoCr alloys, and stainless steel 316, as a film of proteoglycans generated at the bone implant's interface in *in vivo* animal model studies [3]. The

implant's surface topography, surface charges and chemical component are the factors that can interact with adjacent cells. It is generally accepted that rough, textured and porous surfaces are able to stimulate cell attachment, differentiation and the formation of an extracellular matrix [6]. The aforementioned titanium oxide film would be the most suitable biocompatibility film, with high resistance to corrosion and low ion-formation tendency in aqueous situations [3].

In orthopaedics, it is clear that the attachment of osteoblasts to the implant is a crucial requirement for subsequent cell functions, formation of mineral deposit, osteointegration and the bone healing process. However, this formed natural oxide layer being bioinert leads to a lack of tissue bonding ability by the implant [7]. Due to the *in vivo* environment is featured with bio-corrosive and bio-tribological degradations, Titanium-based materials lack the fundamental proactive ability to sustain long-term bone growth, and therefore the current Ti-based orthopaedic implant have a limited effective lifetime of only 15 years [8]. TiO_2 films, however, are dense and smooth and are susceptible to the formation of fibrous tissue that prohibits osteoblasts attaching onto surfaces, an issue which can cause loosening and inflammation [9].

Brånemark first stated the concept of osteointegration. Due to enabling structural and functional coexistence, biological tissues and strictly defined and controlled synthetic component provide lasting, specific clinical functions without initiating rejection mechanisms [10, 11]. Currently, osteointegration means that the implantations are without any relative micro motion and instead have direct contact. Moreover, the process reflects an anchorage mechanism although no vital implanted component

can be continuously incorporated with living bone tissue that has persisting loading [12]. After being implanted, the first stage of major tissue reactions of the skeletal response to implantation related to injury and key histological event include haematoma formation through the intramembranous pathway, and lamellar bone formation on the spicules of woven bone. Osteoblasts and mesenchymal cells can migrate and attach to the implant surface from day 1 after implant insertion, depositing bone-related proteins and creating a noncollagenous matrix layer on the implant surface. Success requires good cell attachment and binding minerals. This matrix is an early formed calcified fibrillar layer on the implant surface, involving poorly mineralized osteoid similar to the bone cement lines and limited laminae that forms a continuous, 0.5–mm thick layer that is rich in calcium, phosphorus, osteopontin and bone sialoprotein [13-15]. Osteogenesis occurs during the next stage at the bone implant interface and can be at a distance or in contact. Distance osteogenesis refers to trabecular growth to the implant surface, whereas contact osteogenesis relies on the newly formed pre implant bone towards the host bone tissue [16]. A few days after implantation, osteoblasts in direct contact with the implant surface begin to deposit collagen matrix, and the process follows the arrangement of woven bone and bone trabecular. Woven bone and trabecular bone with a three dimensional biological scaffold fill the initial gap at the bone implant interface and offer high resistance to early implant physical loading [16, 17]. The scaffold structure also helps in terms of cell adhesion and tissue anchoring, with the process of biofixation beginning after implantation in tissue at 10 to 14 days. Next, woven bone is progressively remodelled and substituted by lamellar bone. The

mature bone around osteointegrated implant is confirmed by the presence of medullary or marrow spaces containing osteoclasts, osteoblasts, mesenchymal cells and blood vessels.

During the aforementioned process, many factors affect osteointegration including properties of implantation and host conditions. However, many clinical failure cases point out the implant surface properties as being one of the main factors influencing osteointegration. Further, the natural, dense and smooth titanium oxide film is featured by lacking osteoblast attachment, and poor bone integration properties. Inadequate osteointegration causes fibrous membrane formation around the implant. This issue ultimately leads to implantation displacement, aseptic loosening and failure of the implant [18].

1.2 Surface modifications to promote osteointegration

Various methods to make titanium implant more bioactive have been developed. Surface engineering can play a significant role in extending the performance of orthopaedic implant made of titanium beyond its natural capabilities. Researchers have placed significant effort into surface modification to improve cell-material interactions and the osteointegration process [19]—examples include plasma-sprayed hydroxyapatite and other ceramics through to the more recent and likely future generation of biomimetic-engineered, nano-texturised surfaces.

1.2.1 Calcium phosphate coatings

Over recent decades, calcium phosphates such as hydroxyapatite (HAp) coating have been widely used to endow bioactive properties on titanium surfaces. Such coatings have the capability to mimic natural bone micro structure and chemical composition. Methods that have been used for coating with Ca and phosphate include dip coating, electron beam deposition, pulsed laser deposition and plasma spraying [20]. Calcium phosphate coating helps early fixation into bone and has demonstrated improvement in osteointegration compared with untreated surfaces when tested *in vivo* [21]. The improved osteointegration was attributed to a rough porous oxide layer in which Ca and P ions were incorporated. Recently, calcium phosphate coatings have been combined with additives to improve antibacterial properties and osteointegration, such as doped HAp with Ag and strontium [22]. Another strategy is combined HAp with antimicrobial peptides (AMP). AMPs were physically adsorbed onto the coatings and the AMP-CaP was adhesive to osteoblasts, exhibiting the capability of killing *S. aureus* and *P. aeruginos*a [23].

However, defects associated with HAp coating have also been reported by researchers. One of the main weakness is that the coating creates a strong bonding on the interface of implant and tissues, and weak bonding of the interface of coating and substrate leads to the coating layer being destroyed, together with the progression of fracture or delamination [24-28]. Fragment and debris generation at the bone implant interface may significantly improve the lifespan of implant, leading to

aseptic loosening.

1.2.2 Engineering surface topography

Engineering of micro or nano-patternings on implant surfaces have also been attempted by researchers to improve interactions with osteogenic cells while simultaneously inhibiting bacterial adhesion. The engineered surface can increase surface area and porosity of the implant to improve bone growth and the coefficient of friction between the bone and implant, thereby reducing micromotion at the bone implant interface and increasing osseointegration. For example, an anchor-like structure was generated on an implant surface using a laser sintering process. The laser-patterned surface combined with a secondary interconnected pore coating, significantly improving primary fixation and bone growth and decreasing micromotion amplitude in both *in vitro* and large animal *in vivo* tests [29]. Chemical etching is another method used to create porosity on implant surfaces; the featured surface has both antibacterial and long-term osteointegration capabilities [30].

The technology of engineering surfaces is limited. First, one of the main limitations is manufacturing. Many implant have complicated curved surfaces that are hard to machine; examples include artificial skull, threads on bone screws and titanium mesh implant. Second, etching can damage the implant surface—acid etching can generate a metal surface with micro pits that enhance the surface ratio; however, the etched surface is also featured with micro channels that can release ions from a substrate and compromise the application of implant. Laser patterning improves the wear and

corrosion resistance of implant surfaces due to the associated high energy causing phase transfer in patterned areas. However, researchers have pointed out that the pattern edge has poor mechanical stability—after the strengthened surface becomes worn, the patterned area develops weaknesses.

Above all, in past decades, implant surface modifications methods were attempted using simply machinery (macro) to improve roughness, developed to create porous HAp and therefore mimic bone structure (micro). The underlying concept of the bone implant interface issue was from being simply mechanical to a biomimetic bone structure. However, a breakthrough occurred while researchers were focusing on the nanoscale. The bone implant interface issue was firstly stated as being related to how the nanotopography interacts with the cell, with the mechanism of nanotopography affecting cell behaviour, such as cell migration, proliferation and differentiation. The development of nanotechnology also provides an angle with which to understand the behavioural mechanism of parts of a single cell from the nanoscale. Base on this understanding, the design and manufacture of implant down to the nanoscale is meaningful, influencing cell behaviour towards being conducive to successful implant. This understanding is in line with the concept of third-generation biomaterials where reproducible molecular control is desirable—that is, the same response occurs each time [31].

1.3 Titanium dioxide nanotube

1.3.1 The nano trend

Nanotechnology has recently emerged as an exciting way to modify titanium substrates to provide good integration with bone tissue [32-34]. In particular, TiO_2 nanotubes (NT) fabricated by anodization have attracted researchers due to their unique morphology, physical and chemical properties, ability to enhance adhesion and accelerate cell growth in addition to their ease of production [8, 35].

Anodization is a feasible fabrication method used to generate NT on titanium substrates. In contrast to other coating technologies, one of the main advantages of anodization is its universal applicability. Due to the electrochemical reactions, NT growth and arrangement occurs vertically from the substrate spontaneously, leading to the NT layer being able to grow on various types of titanium implant surfaces. Further, the anodization process is easy to implement. Compared with laser texture and HAp plasma spray, anodization requires less external energy and production facilities.

The NT chemical composite with TiO_2 exhibits similarity with natural oxide film on titanium, and this advantage can also minimum tissue reactions, such as inflammation. The natural formed but dense TiO_2 film provides protection on titanium to avoid metal ion release into adjacent tissues. However, NT display an increased specific surface area, which can effectively improve cell attachment. Furthermore, the nanotube structure can mimic the natural bone mineral nanostructure [36]. Implant with

nanostructured biomimetic surfaces have gained attention because they can provide a highly suitable topography for protein and cell interactions [37-40]. In addition, the 3-D nanoporous structure can aid antibiotic loading at the site of implantation for local drug delivery when tubes are filled with gentamicin [41].

Another remarkable usage of nanopatterned compounds is to provide potential tools to understand biochemical signalling, and possible direct mechanotransducive signalling in cells, revealing cell adhesion mechanisms due to the interactions of nanotopography and filopodia [42]. Researchers have demonstrated that the behaviour of MSCs is strongly affected by the dimension of NT [43]. On small diameter nanotubes, MSCs are featured with increased cell adhesion, and growth with minimal differentiation seems to be prevalent, potentially due to protein aggregate adhesion and distribution configurations induced by the small nanotubes. In contrast, on larger diameter nanotubes, MSC cells are forced to elongate and stretch to search for protein aggregates, and as a result, are forced/guided to differentiate specifically into osteoblast cells.

1.3.2 NT fabrication mechanism and *in vitro and in vivo* for orthopaedic implant application

NT fabrication mechanism

NT can be fabricated by various methods, including sol-gel, template-assisted, hydro/solvo thermal methods and anodization (electrochemistry method) [44]. Electrochemical anodization in particular has attracted considerable interest over the

last 15 years. This interest has been ascribed to the controllable morphology of NT. Since 1999, Gong et al. have been generating NT using electrochemistry in hydrofluoric acid first. The mechanism, structural design and relationship between each parameter in the anodising process have been well researched [45-47]. The fabrication process is carried out in an electrolytic cell with two electrodes. The electrochemical anodization has been used to build highly ordered, self-oriented NT with titanium foil and platinum foil, containing an F^- ion electrolyte. Aqueous hydrofluoric acid electrolyte was used by Gong and co-workers for the first time. Parameters such as anodization voltage waved area successfully generated tubes from 10 to 40 V; HF concentrations were from 0.5 to 3.5 wt %. Under these parameters, the diameter of tubes was 25 nm to 60 nm, and the limited length of NT was 500 nm because of the dissolution of the growing top of NT due to the strong acidity of the HF electrolyte. Apart from inorganic electrolyte, NT are also formed in containing F^- ions and viscous organic electrolytes such as ethylene glycol and glycerol [48]. Longer NT can be obtained by using organic electrolytes; for example, the length was observed to increase to 7 µm by controlling pH to avoid top tube dissolution in the electrolyte [49, 50]. Highly ordered nanotube arrays—220 µm length tubes, were fabricated by Shankar et al. with an ethylene glycol (EG)-based electrolyte, HF, KF or NaF providing F^- ions [51].

Compared with aqueous electrolyte, using organic electrolytes can obtain mildly reducing conditions due to the increased difficulty of the oxygen donation process. The generation of NT is caused by Ti oxide fabrication and TiO_2 dissolution in the

electrolyte due to two reactions:

$$Ti+2H_2O \rightarrow TiO_2+4H^+ \quad (1)$$

$$TiO_2+6F^-+4H^+ \rightarrow TiF_6^{2-}+2H_2O \quad (2)$$

Viscous organic solution can provide a pH gradient that has a tendency to decrease from tube mouth to bottom, leading to chemical etching at the bottom while avoiding mouth part dissolution in the electrolyte [50]. The growth of the oxide layer is determined by the ions' transportation process. The $[TiF_6]^{2-}$ ion is formed by complexation of Ti^{4+} ions, which is ejected at the oxide–electrolyte interface (dissolution layer in Figure 1. 1) from the oxide film (oxidation layer in Figure 1. 1), whereas F^- ions migrate through the oxide, forming TiO_2 by chemical attack [52].

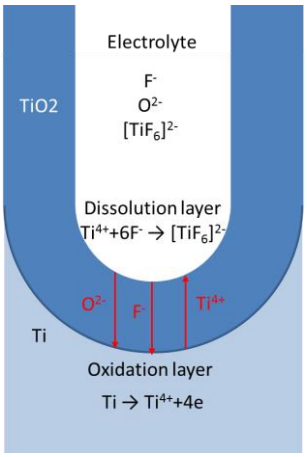

Figure 1. 1 Ion transfer during anodization. Oxygen ions diffuse to the interface between the nanotube bottom and titanium substrate from the electrolyte; fluorine ions have the same transfer route to oxygen ions and release electrons. Titanium is transferred from substrate side to nanotubes' inner bottom surface and electrons are obtained, forming titanium ion, which is then combined with oxygen ions to generate TiO_2

During the initial anodization stage, these two reactions occur at a high rate. However, the fabrication reaction (anodic oxidation) plays a dominate role compared to the

dissolution reaction (chemical etching). Smaller and irregular pore sizes are fabricated. As the NT layer increases, the rate of anodization decreases and the chemical etching process dominates—this process then leads to increased pore size. At the final stage, the concentration of F^- is decreased, the chemical etching rate is lower than the anodic oxidation rate and the pore size becomes small again [53].

Dong explained a different and highly detailed mechanism in their wettability study of NT. While anodization reacts in an EG solution, the ammonium fluoride participates in the reaction and is ionized into the ammonium ion (NH^{4+}) and fluoride (F^-)—the product can be $Ti(OH)_4$ rather than TiF_4 [54].

$$Ti + 4H_2O + 4NH_4F \xrightarrow{HO(CH2)2OH} Ti(OH)_4 + 4NH_4^+ + 2F_2\uparrow + 2H_2\uparrow \quad (3)$$

Due to vapours being obtained on both cathode and anode sides, the anodic mechanism reaction is modified, and $Ti(OH)_4$, H_2, NH^{4+} and F_2 are obtained. F_2 vapours is obtained on the anode side and H_2 vapours is generated on the cathode side—based on this process, NH^{4+} remains in the electrolyte. It is observed that the initial products are not TiO_2, but $Ti(OH)_4$, due to the hydroxide compounds of the NT surface after anodization. Another phenomenon is the increase in hydrophilicity after heat treatment of NT, which is conversed with general annealed metal oxide (more hydrophobic). Water droplets were found to decrease by 40 to 56% after being annealed in Dong study, with the author examining the effect of aging tubes in 3 months. The results demonstrate that the NT surface hydrophobicity was increased for as-anodised tubes, annealed tubes and bare Ti surfaces. This observation may be due to $Ti(OH)_4$ being less stable than TiO_2—the reaction substitutes $Ti(OH)_4$ to TiO_2,

and H_2O vapour is released into the environment. The speed of reaction would be accelerated by hydroxyl and oxygen. FTIR results confirmed this hypothesis—the hydroxyl group was embedded in the as-anodized NT and decreased in aged NT.

$$Ti(OH)_4 \rightarrow TiO_2 + 2H_2O \uparrow \quad (4)$$

There are many methods available for NT modifications to match its applications. The usage of NT in biomedical implant applications has also been studied both in vitro and in vivo. A significant increase in bone implant contact (BIC) and gene expression levels was found in bone attached to implant with NT, particularly with 70 nm in diameter nanotubes compared with 30 nm and 100 nm in diameter.

NT in vitro performance

Cells' response to NT has also been investigated by researchers. The interactions between NT and mesenchymal stem cells were also studied by Sungho Jin [55]. Different diameters of NT have been investigated in terms of adhesion, proliferation and differentiation in cultured human mesenchymal stem cells (hMSCs). MSCs are multi-potent stem cells that can differentiate into stromal lineages such as adipocytes, chondrocytes, fibroblasts and osteoblast cell types by generating the appropriate intermediate progenitors for each. NT with decreased diameter (30 nm) promoted adhesion without noticeable differentiation, whereas larger (70 to 100 nm diameter) nanotubes elicited a dramatic stem cell elongation (10-fold increase), which induced cytoskeletal stress and selective differentiation into osteoblast-like cells, offering a promising nanotechnology-based route for unique orthopaedics-related hMSC treatment. The speculated mechanism led to, on small diameter nanotubes with 30

nm in diameter, increased cell adhesion and growth with minimal differentiation, partly due to the protein aggregate adhesion configurations induced by the small nanotubes. On larger-diameter nanotubes, hMSC cells are forced to elongate and stretch to search for protein aggregates, and as a result, are forced/guided to differentiate specifically into osteoblast cells.

However, the phenomenon of precedence of MSCs attaching to small tubes and differentiation on large nanotubes has been questioned by Prof. Schmuki [56,57]. He also studied MSC adhesion, spreading, growth and differentiation on different diameter nanotubes, from 15 nm to 100 nm. The results of his study are in slight contrast with the work of Sungho, who found that larger nanotubes (around 100 nm) have the most improved differentiation ability for MSC stem cells [55]. Conversely, MSC cell adhesion and spreading were severely impaired with respect to nanotube diameters larger than 50 nm, resulting in dramatically reduced cellular activity and a high extent of programmed cell fate. Although the preference diameter of nanotubes with the improvement of stem cell activity is controversial, the critical impact of NT diameter in terms of influencing cell behaviour has reached a consensus. Further, that nanotubes positively affect adhesion and propagation of osteoblasts has been well documented. It is well known that osteoblasts are a crucial prerequisite to subsequent cell functions such as synthesis of extracellular matrix proteins, formation of mineral deposits and osseointegration on the substrate surface. Seunghan et al. have experimentally investigated and demonstrated that with nanotube structure inducement, a significant acceleration in the growth rate of osteoblast cells by as much as 300 to 400% occurs,

compared with pristine titanium surface samples [8]. Regarding the phenomenon of 70 nm in diameter nanotubes having better performance than 100 nm in diameter nanotubes, the authors concluded that this observation was most likely due to the natural bone collagen type 1 forming fibrils with an interfibrillar spacing of 68 nm and 35 nm depth, and hydroxyapatite crystals being embedded in fibrils, with an average size of $50 \times 25 \times 4$ nm^3—70 nm nanotubes are more efficient in terms of mimicking natural bone. Peng et al. determined that significant cell adhesion increased on nano-textured surfaces in vitro—C3H10T1/2 mouse cells were seeded on different diameters of nanotubes, 30 nm and 80 nm, and both size nanotubes were significantly enhanced cell adhesion compared to a polished titanium surface and acid-etched titanium [58]. A filopodia of growing cells spreading across the pores of nanotubes' surface produces an interlocked cell structure. Gongadze et al. suggested that the attraction between a negatively charged Ti surface and a negatively charged osteoblast is mediated by charged proteins with a distinctive distribution of quadrupolar internal charge [59]. When discussing the osteoblast surface interaction, it ultimately concerns an interaction between the cell and its surface-surrounding proteins or other biomolecules. Because osteoblasts are negatively charged, they are electrostatically repelled by the negatively charged titanium surface as long as some other attractive forces are not present in the system. Nanorough regions, due to the distribution of many highly curved nanoscale protrusions, have increased surface charge density and electric field strength, leading to promote divalent cation-mediated adsorption of fibronectin to a negatively charged titanium surface and quadrupolar

protein-mediated adhesion of osteoblasts (Figure 1. 2).

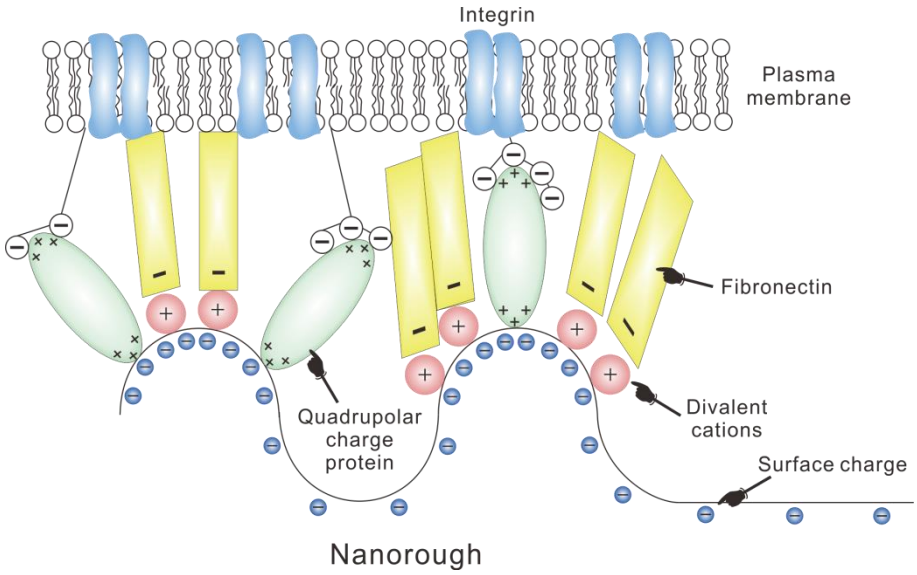

Figure 1. 2 Protein-mediated adhesion of an osteoblast to the nanorough region of a titanium surface is facilitated by the increased surface charge density and electric field strength at highly curved convex edges and spicules

NT in vivo evaluation for orthopaedic application

Apart from the in vitro performance of NT on titanium, the application potential of NT has also evaluated by researchers, particularly for in vivo animal models. One in vivo experiment was setup by Na et al. to compare the osteointegration performance with different sizes of nanotubes generated on a titanium cylinder implanted at 3, 5 and 8 weeks in mini pigs [60]. Higher osteogenesis-related expression was observed on implant surfaces with vertically arranged NT than a bare-machined surface, and 70 nm diameter NT demonstrated significantly higher expression of Osterix (Osx), alkaline phosphatase (ALP), Type 1 collagen (COL 1) and tartrate-resistant acid phosphatase (TRAP) than the remaining nanotubes. Due to the more active expression of ALP, COL 1 and TRAP in 70 nm nanotubes, a higher bone remodelling

rate at the bone implant interface was indicated. Not only with respect to mini pigs, but NT have also been employed in animal tests such as a rabbit model [61]. However, the applied nanotubes were generated in one small size of 37 ± 11 nm in diameter, and only around 160 nm length on cylinder implant inserted in subchondral bone. Histology and pull-out testing demonstrated well that 37 ± 11nm diameter nanotubes have enhanced osteointegration compared to a machined surface, and tissue bonding slightly higher than classic grit-blasted, acid-etched micro-featured surfaces.

1.3.3 NT biofunctional modification for anti-bacterial effects and cell differentiation

In recent years, various synthesis routes for nanotube geometries have emerged for titanium oxide. In the biomaterials field, particularly from the orthopaedic implant perspective, the manner in which to synthesise tubes with a simple and optimized method has stimulated significant research activity.

A novel approach for fabricating top-porous perfectly aligned tubes using 2-step anodization has been published by Wang and co-workers [53]. Due to the liquid-meniscus-induced forces, with the increase of aspect ratios, bundling structure tubes are generated on the top of NT [62]. This bundling structure not only limits the NT properties in solar cells but also impacts modification approaches due to affects upon infiltration materials. In their work, after the first step of anodization, a peeled-off etching process was developed by soaking the films in a saturated $HgCl_2$ solution for 2 h, leaving bowl-like footprint—a bundling structure was induced by adding 1% HF in

the electrolyte by over-etching the top part (which is thin and fragile) in the second step of anodization. A top-pore morphology structure is obtained owning to the instantaneous hydrolysis reaction on the orifices of TiO_2 and the dissolution of TiO_2 in a highly acidic environment involving hydrogen fluoride consumption; the changing pore size reflects the balance between Ti^{4+} ejection and the deposition on the surface in the form of TiO_2 [63]. Initially, anodic oxidation plays a dominate role (large current density, $Ti^{4+} \rightarrow TiO_2$) although oxidation rate and HF etching rate were both found to be fast; then, the ejection rate of Ti^{4+} slowed down, a larger porous structure was obtained due to the etching process dominating during this period and the concentration of HF was decreased, leading to decreased pore size.

Sergiu P. Albu [64] published in 2008 work detailing fabricated double-walled nanotubes, demonstrating that the tubes can be converted to an ordered TiO_2 nanoporous structure due to a rapid optimized thermal annealing process. The outer and inner shell structure were confirmed in a TEM image, and the outer shell structure had a near constant thickness; the inner shell increases from a few nm at the top to 50 nm at the bottom after 120 V anodization in EG electrolyte. The anodic tubes were annealed at 500ºC for 10 s with the rates of 1 $ºCs^{-1}$, 25 $ºCs^{-1}$and 50 $ºCs^{-1}$. With the annealing rate of 1$ºCs^{-1}$ at 500ºC, a structure of separation of inner shell with an outer shell can be fabricated (double-walled structure); when the heating rate was accelerated to 25 $ºCs^{-1}$, a loss of double-walled morphology was noted. It is remarkable that a highly ordered porous membrane can be fabricated when the rate is up to 50 $ºCs^{-1}$, and some inner shell was found to collapse into a porous nature during the heating

process. The size of nanocrystallites that built the annealed wall of nanotubes increased from several nanometres to 200 nm, with the author claiming that one possible approach is the non-equilibrated kinetics leading to the abnormal speed of crystal growth. After Sergiu's work, a further detailed double-walled mechanism with several synthesis methods have been studied by Jiaguo published in 2010 [65] and Daoai published in 2011 [66]. Apart from morphology modification, the phase and chemical composition were also analyzed; to improve the mechanical properties of NT, researchers attempted approaches such as converting nanotube layers to semi-metallic TiOxCy using a thermal heating method in an acetylene atmosphere [67]—the semimetallic nanotubes demonstrated significant enhancement of hardness, tensile strength and friction behaviour [68]. Other biomedical modifications have been discovered; for example, bone morphogenetic protein 2 (BMP2) was functionalized on the surface of nanotubes, and it was found that the BMP2-coated surfaces were beneficial for cell proliferation and differentiation, with significantly higher differentiation levels than uncoated nanotubes [69].

Apart from the improvement of cell activity, NT can also be biofunctionally modified, for example by loading drugs for antibacterial capability due to their unique geometry. It is hypothesised that the hydrophilic TiO_2 nanotube structure with a negative charge attaches to positively charged osteoblast cells and repels the same negatively charged microbes, reducing build-up such as biofilm formation and resisting infection. Further, biofunctional modification for drug delivery of NT has been well studied—one of the common methods is to embed Ag oxide/Ag nanoparticles in nanotubes. One

study employed magnetron sputtering and anodization to generate NT-Ag_2O arrays containing Ag in a wide range (from 0 to 15%). Different diameters ranging from 5 nm to 20 nm of crystallized Ag_2O nanoparticles were embedded in amorphous TiO_2 nanotubes, leading to controlled release of Ag^+ that generates adequate antibacterial activity without any cytotoxicity (osteoblasts) [70]. The NT-Ag_2O arrays could still effectively kill *Escherichia coli* and *Staphylococcus aureus* even after immersion for 28 days, demonstrating long-lasting antibacterial capability.

One strategy of immobilizing antimicrobial peptides in NT has been reported, with a film of novel structure with dual diameter from 35 nm cap to 140 nm bottom NT being fabricated and loaded with ponericin G1 peptide. The new structure of NT has increased prolonged-release AMP kinetics, up to 60 days, compared to normal NT released in 42 days in phosphate-buffered solution [71]. AMPs are widely distributed in living organisms and function as part of their first line of defence. AMPs have drawn significant attention because of their rapid bactericidal activity against a broad spectrum of bacteria and other microbes, low toxicity and immunogenicity, as well as complex killing mechanisms [72-74]. The nanotubes' structure provides the capability to simply fill drugs using relatively easy methods such as immersion and doping; however, one of the challenges involves the robust release of drugs [75-77]. The kinetics adsorption and release are mainly governed by physical interactions between charged terminal groups of the adsorbed molecules and the hydroxide layer forming on nanotube surfaces [78]. Peng et al. reported elution kinetics of two kinds of drug model and demonstrated that NT can control small molecule delivery in the period of

weeks, and larger molecules in the order of months for the elution [79].

Another remarkable strategy involves altering charging of NT to achieve antibacterial properties. An external electrical current was applied to capacitive NT doped with carbon, and the carbon-doped nanotubes exhibited bacterial killing without impairing the growth of osteoblasts [80].

1.3.4 Limitations of NT in orthopaedic application

NT with respect to their use in biomedical applications are still at a relatively early stage. Implant surface morphology and chemistry on both micro and nano size have been widely demonstrated to affect the associated biointeractions [81]. Cell growth, proliferation and differentiation on NT have been investigated; one important finding in this regard is that cell behaviors are strongly dependent on NT diameter [82]. Mesenchymal stem cells, hematopoietic stem cells, endothelial cells, osteoblasts and osteoclasts were cultured on different diameters of NT [8, 55, 57, 83-85].

From clinical retrieval reports, the two leading causes of implant failure are aseptic loosening and infection. Aseptic loosening is the leading cause of long-term failure of 20% [86]. Furthermore, aseptic loosening can be caused by various sources; one key factor is the micromotion at the bone implant interface, leading to progressive worsening of micromotion. Wear can damage the implant surface, generating wear particles that are then released and trapped at adjacent bone tissues, activating macrophages and initiating a series of cytokines. These cytokines, such as tumour necrosis factor α (TNF-α), result in osteoclast activation, osteoclastogenesis and bone

resorption [87, 88] (see Figure 1. 3). Therefore, reduction of micromotion and limiting particle wear generation are pursued targets for implant material/implant surface coating materials.

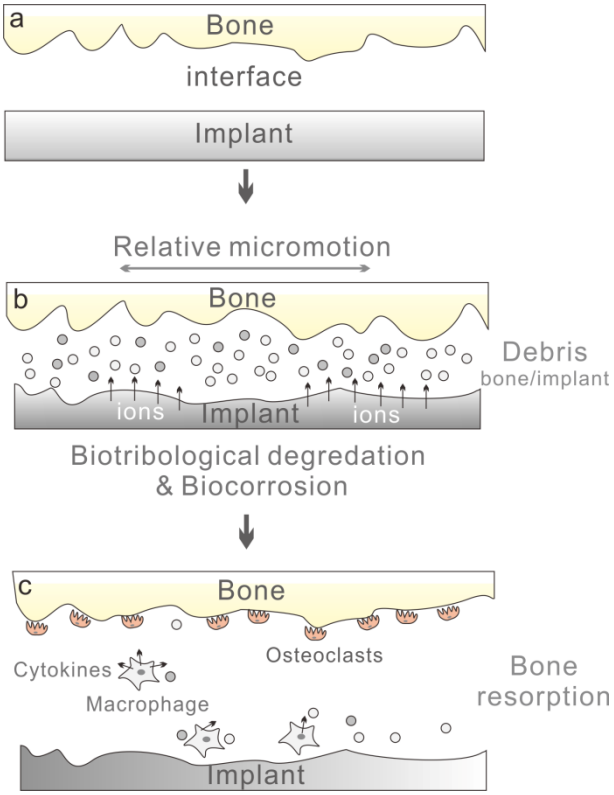

Figure 1. 3 Aseptic loosening pathways associated with gaps at the bone implant interface. Debris is generated by wear between bone and implant surface and is trapped in the bone tissue. This trapped foreign debris causes a tissue response; in brief, activating macrophages that then release cytokines and resulting in osteoclast activation. The active osteoclasts can absorb bone tissue, causing loosening of the implant

Hence, the biotribological properties of implant materials affects implant performance, even at the bone tissue bonding interface. The tribology can be defined as 'the science and technology of interacting surfaces in relative motion and the practices related thereto', and the biotribology is all aspects of tribology related to biological systems [89]. Wear particles due to biotribological damage are a concern with respect to

activating inflammatory reactions at surrounding organs, leading to loosening of implant or subsequent failures. Another main degradation is delamination, which can promote the wear loss of coating. Because NT have been widely demonstrated in animal models such as those involving rabbits, mini pigs and rats for their positive association with osteointegration, the biotribological and wear performance of NT were mostly ignored due to the limitation of serve duration in animal models. At the same time, NT have particular advantages—the NT layer has poor interfacial adhesion between tube layers and Ti substrate, and the TiO_2 nanostructure is prone to peel off [68, 90, 91]. The shear strength can be a decisive factor in terms of implant coating applications—wear debris released around tissues under mechanical stress results in inflammatory reactions that may cause implant failures [92, 93]. However, the crucial importance of the poor adhesion problem of NT has yet be solved. In clinical reports, osteointegration has been found to be strongly affected by the wear behaviour of the implant surface.

Apart from mechanical properties, corrosive behaviour is also one of the key characteristics for implant applications. Corrosion and surface dissolution are two mechanisms that can release ions into the body, potentially causing adverse biological reactions and mechanical failure of implant [94]. NT have a larger surface area, and their different morphology may influence corrosion resistance compared with a conventional titanium surface [95]. Only a few reports have focused on the corrosion resistance of NT; Saji and co-workers found that the nanotubular structure of a Ti–35Nb–5Ta–7Zr alloy could form an immediate and effective passivation in

Ringer's solution at 37°C [96]. Yu studied the corrosion behaviour of TiO_2 nanotube layers and titanium in naturally aerated Hank's solution, finding that TiO_2 nanotube layers showed better corrosion resistance than smooth titanium, and that annealed NT which feature anatase have enhanced corrosion resistance in its outer tube layer, with only slight effects being noted for the inter-barrier layer [95]. Thus, the significantly enhanced corrosion resistance of TiO_2 cannot be achieved using an annealing method due to the tube structure not changing. Whereas significant amount of research have focused on biofunctional NT to enhance their antibacterial nature or interactions with cells, biotribological and biocorrosion performance of NT have been neglected despite these areas playing a key role in the long-term success of implantation.

1.4 Research aim and objectives

NT have been demonstrated to be able to improve protein adsorption and cell attachment. These compounds have significant potential for orthopaedic implant surfaces to enhance the *in vivo* performance of implant. Retrieval analysis has revealed that wear and corrosion are the main factors that contributed to the implant failures. Whereas biotribological and biocorrosion aspects are the main concerns, limited research in this regard with respect to titanium nanotubes has been reported in the literature. The hypothesis are the biotribology and biocorrosion resistance, as well as cellular performance of titanium implant surfaces could be enhanced through engineering the formation of titanium dioxide nanotube layers.

The aim of this study is to engineer titanium dioxide nanotube formation to create a structurally modified titanium dioxide nanotube layer with enhanced biotribological performance and biocorrosion resistance, systematically characterize and evaluate its biotribology and biocorrosion characteristics, as well as its cellular performance. The objectives are:

1. To understand the failure mechanisms of orthopaedic fixation screws by retrieval analysis of failed orthopaedic fixation screws.

2. To engineer the titanium dioxide nanotube formation to create a structurally modified titanium dioxide nanotube layer on a titanium substrate.

3. To study the effect of NT layers on the biotribology and biocorrosion of titanium.

4. To evaluate the cellular performance of the modified titanium with respect to cellular attachment and growth.

Chapter 2

2. Materials and Methodology

The materials fabrication and characterisation methodology are illustrated in this chapter. Conventional TiO_2 nanotubes (NT) and structure-optimised TiO_2 nanotubes (SO-NT) were fabricated using an electrochemical method, described in the following section. The physicochemical properties of materials were characterised by scanning electron microscopy (SEM), energy-dispersive X-ray spectroscopy (EDX), X-ray diffraction (XRD) and X-ray photoelectron spectroscopy (XPS). Further, the mechanical features were measured by Nanoindentation, Vicker's hardness test, and other methods. In particular, the biotribological and biocorrosion behaviour of materials were comparatively tested using a pin-on-disk tribometer.

2.1 Creation of TiO_2 nanotubes (NT) layers on Titanium substrate

2.1.1 Conventional NT fabrication

Sample pretreatment

NT was fabricated using an anodisation method. Titanium foil samples (99.5% thickness of 0.15 mm) were cut into 4×4 cm^2, washed in deionised (DI) water and alcohol for 20 min and then air-dried. Titanium sheet samples (Goodfellow, 99.6% thickness of 1.5 mm) were cut into 2.2×2.2 cm^2. Grinding and polishing were undertaken using 200, 400, 600, 800 and 1200 grit papers. After the polish process, the titanium sheet samples were flat and smooth, without any optically observable scratches. After polishing, the samples were ultrasonically cleaned in ethanol and DI water for 20 min.

Anodization

The anodisation process followed after the pretreatment of titanium. The samples were anodised using a conventional two-electrode setup with a graphite sheet counter electrode. The specimens were completely immersed in the electrolyte. Furthermore, two different anodisation electrolytes were attempted in this thesis, one was an aqueous electrolyte (10 vol%, one-step anodisation), and the other was pure ethylene glycol (two-step anodisation). The concentration of electrolyte for one-step anodisation was 1.2 wt.% NH_4F (96+%, Fisher chemical) in ethylene glycol (99%+, extra pure, ACROS Organics) content 10 vol% DI water. Two-step anodisation was in

pure ethylene glycol (99%+, extra pure, ACROS Organics) with 0.5wt.% NH_4F (96+%, Fisher chemical) under a constant temperature of 15 °C linked with an external cyclic water thriller, see Figure 2.1. The parameters of anodisations are illustrated in Table 2. 1.

Table 2. 1 Parameters of one step and two steps anodization

Route	Voltage	Electrolyte	Temperature	Duration
One step	20–40V	1.2 wt% NH_4F ethylene glycol (10 % water)	Room temperature (18–22°C)	60min
Two steps	20–60V	0.5% NH_4F ethylene glycol	15°C	60min+60min

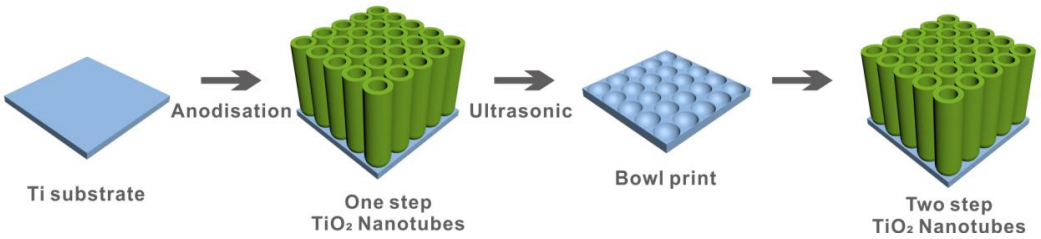

Figure 2. 1 Scheme for one– and two–step NT fabrication

The one-step nanotubes are obtained after 60 min of anodization (Figure 2.1 left procedure). For two-step nanotubes (Figure 2.2 full procedure), similar anodisation is carried out for 60 min; following ultrasonic vibration washing in DI water, the surficial TiO_2 nanotubes layer is lifted off. Afterwards, additional anodisation in electrolyte for 60 min is performed under the same parameters. After anodisation has been completed, NTs were rinsed with DI water and dried with an N_2 stream.

Annealing NT

Annealing NT is a facile method for transferring titanium dioxide from amorphous to anatase form. NT specimens were annealed in a Muffle furnace. The annealing

process included heating to 500 °C at a rate of 4 °C/min. Specimens were maintained at 500 °C for 30 min, then cooled to room temperature within the furnace.

2.1.2 Interfacial engineering TiO_2 nanotubes, bonding layer fabrication

As aforementioned in Chapter one, the conventional NT has poor adhesive strength to the titanium substrate because the bottom of the nanotube was a typical sphere structure. To improve conventional NT mechanical stability, including biotribology and biocorrosion performance, further experimental investigations were carried out to engineer the nanotubes-substrate interface. For this purpose, the specimens were further anodised in H_3PO_4 acid containing electrolyte to generate a TiO_2 compact bonding layer at the interface between the nanotubes' bottom with the titanium substrate (Figure 2. 2). It is generally known that titanium oxide growth involves field-assisted migration of ions through the oxide films, and the thickness of the anodic oxide follows Faraday's laws. Due to these laws, parameters affecting the mechanical stability of the bonding layer are thickness, bonding layer structure and grain size.

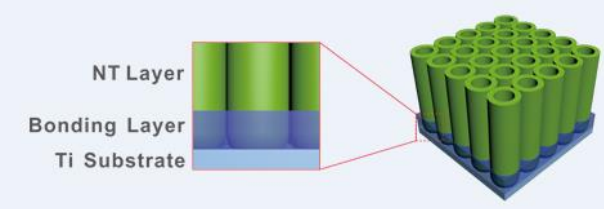

Figure 2. 2 Schematic illustration of bonding layer at TiO_2 nanotubes-titanium substrate interface that wrap the bottom of titanium

The ideal thickness of bonding layer could be similar to the TiO_2 nanotubes' layer

thickness because it can integrate with the nanotubes' structure. A feasible method to increase the thickness of the bonding layer is applying high voltage; however, it is impossible to generate a well-organised nano-sized thick (> 500 nm) bonding layer. Instead, irregular micro-sized titanium oxide grains are obtained as the potential applied increases to where electric sparkling is observed [97, 98]. The irregular oxide grains strongly affect the arrangement and structure of TiO_2 nanotubes. The strategy for optimising a bonding layer involves fabricating as thick a bonding layer as possible with ordered nanosized grains, maintaining the nanotubes' structure at the same time.

Table 2. 2 experimental arrangment to investigate the effect of processing parameters on bonding layer formation (H_3PO_4 contained electrolyte)

	Voltage(V)	**Duration(min)**
a	200	30
b	150	60
c	150	10
d	130	10
e	120	10
f	110	10
g	105	60
h	100	15
i	100	1
j	95	15
k	90	5
l	85	5
m	80	15
n	80	5

2.1.3 Structure optimised TiO_2 nanotubes (SO-NT)

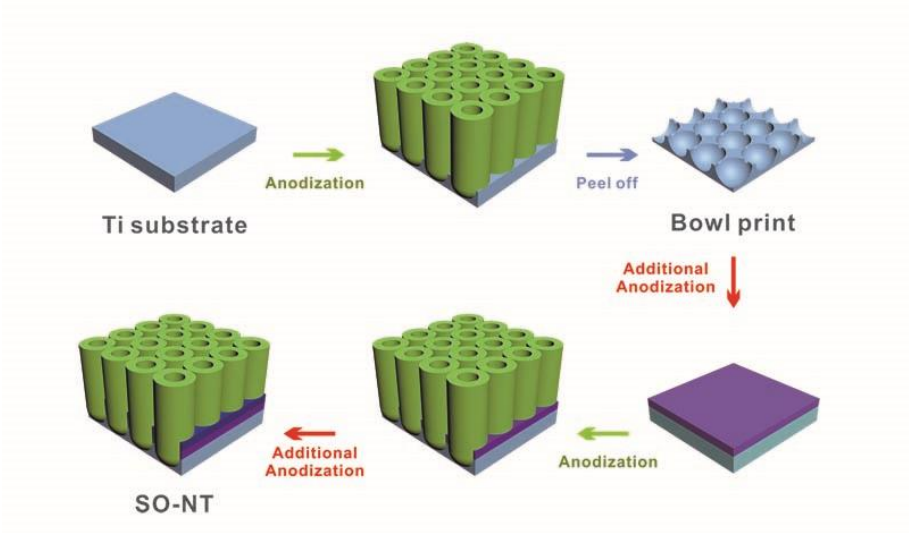

Figure 2. 3 Scheme for structure optimised TiO_2 nanotubes fabrication, the SO-NT fabrication was based on two-steps anodization with additional anodization in H_3PO_4 electrolyte

Based on interfacial engineering, a structure-optimised TiO_2 nanotube was formed. Such nanotubes are based on the typical process of two-step anodisation but with additional anodisation after each step, displayed in Figure 2.3. The first step of anodisation was performed for 30 min in ethylene glycol with 0.5 wt.% NH_4F, peeled-off by ultrasonic washing in DI water and then dried. Subsequently, additional anodisation was carried out in pure EG with 3–5 wt.% H_3PO_4 for 3 min at 60 V. The second step was performed in the same condition, 0.5wt.% NH_4F for 60 min, dry out, then anodised in 3–5 wt.% H_3PO_4 for 3 min. After anodisations were complete, structure-optimised TiO_2 nanotubes samples were rinsed with DI water and dried with a N_2 stream.

2.1.4 Formation of TiO_2 nanotubes on medical Ti_6Al_4V alloy and on orthopaedic screws

In addition to fabrication of TiO_2 nanotubes and structure-optimised TiO_2 nanotubes on pure titanium, fabrication of nanotubes on medical-grade Ti_6Al_4V was also investigated and will be discussed in detail. Because the rich Al phase was prone to being eroded in fluorine electrolyte, the long procedure would generate defects on the rich Al phase. Compared with the parameters applied on pure titanium, the anodisation duration of Ti_6Al_4V alloy was shorter—anodisation in 0.5 wt.% NH_4F for 40 min. Moreover, the TiO_2 nanotubes and structure-optimised TiO_2 nanotubes were also fabricated on medical devices using internal fixation screws. The nanotubes were fabricated on Ti_6Al_4V medical-grade (TC4) veterinary fixation screws (3.5 mm in diameter and with 26 mm length, self-tapping screws, manufactured by Shanghai Huifu company). Screw samples were sequentially cleaned in acetone, ethanol and DI water, then air-dried. The first anodisation step was performed for 30 min in ethylene glycol with 0.5 wt.% NH_4F, then additional anodisation was carried out in pure ethylene glycol with 3 wt.% H_3PO_4 for 1 min. After both anodisation steps, structure-optimised TiO_2 nanotubes were rinsed with DI water and dried with a N_2 stream.

2.2 Characterizations

2.2.1 Morphological observation

After TiO_2 nanotubes were generated on the titanium substrate (both foil and plate), the first characterisation was observed by scanning electron microscope (SEM). SEM is a common characterisation method in materials science used to produce images of a sample by scanning the surface with a focused beam of electrons. The electrons interact with atoms on the sample surface, producing various signals that contain information about the surface topography. Because of the nano-featured structure, a field emission HR-SEM JSM-6701F (Japan) with 3 nm maximum resolution was applied to analyse TiO_2 nanotube structural details, such as tube diameter, length (TiO_2 nanotubes array thickness) and level of homogeneity. Furthermore, an SEM (JSM-5600LV) with 20 nm resolution was also used to analyse the micro-sized samples, such as biotribological wear track, due to the entire spectrum of array behaviour being more important than individual nanotubes.

Before SEM observation, the samples were pretreated with an ultrasonic washer in DI water and alcohol, and dried with a N_2 stream. For SEM sample preparation, gold nanoparticle sprays were used to enhance the electro conductivity of the sample's surface. The SEM parameters were adjusted according to the sample's substrate thickness—the working distance was set in a range from 7.8 to 9.0 mm and at a constant voltage of 5 kV–10 kV.

The top view of TiO_2 nanotubes was observed to determine the characteristics of the

sample surface, and nanotube profiles were analysed to assay whether fragments had detached from the substrate and subsequently scratched the sample's surface.

2.2.2 Chemical composition

Chemical composition affects to a significant degree a biomaterial's performance. The chemical composition was mainly analysed using X-ray photoelectron spectroscopy (XPS) and SEM energy dispersive X-ray analysis (SEM-EDX). XPS is one of the most powerful tools available for the quantitative analysis of chemical surface composition of materials. It is also a surface-sensitive quantitative spectroscopic technique that measures the elemental information of a material's surface. XPS is obtained by irradiating a material with a beam of X rays while simultaneously measuring the energy and number of electrons that escape from the top 0 to 10 nm of the material being analysed (see Figure 2.4). Usually, the entire XPS spectrum scan was carried out to analyse the elemental content, and a specific high-resolution scan was applied to analyse and compare individual element peaks.

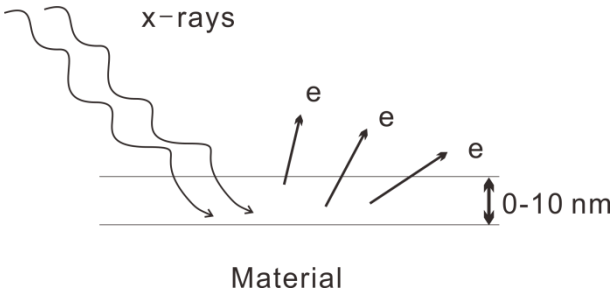

Figure 2. 4 Schematic illustration of XPS surface detection and reflection

SEM-EDX was also employed to investigate the element's transfer after a biotribological test in the retrieval chapter (Chapter three) and analyse the elemental distribution of interfacially engineered TiO_2 nanotubes. Compared with XPS,

SEM-EDX can combine both morphology and chemical analysis areas, providing more detail.

XRD was also applied to compare the oxidation phase content of TiO_2 nanotubes. XRD is a rapid analytical technique primarily used for phase identification of a crystalline material and can provide information on unit cell dimensions. In this study, due to the TiO_2 nanotube samples being uniformed in terms of growth on the titanium substrate, three different areas on samples were randomly selected and scanned by both XPS and XRD to confirm that the scanning results were representative of the entire sample.

2.2.3 Mechanical property

The measurement of mechanical properties of Ti, NT and SO-NT includes macro hardness (Ti and NT), E modulus (nanoindentation, NT and SO-NT), surface roughness (Ti and NT), bending and twisting (NT and SO-NT), ultrasonic vibration (NT and SO-NT), shock (NT and SO-NT), industrial impact (NT and SO-NT) and industrial pull-out test (NT and SO-NT).

The macro hardness of NT and Ti were measured by a Vickers hardness tester, calculating the average of 12 testing points randomly selected in the 12 different areas. The hardness was calculated using equation 2. 1:

$$\mathrm{HV} = \frac{1.8544\mathrm{F}}{\mathrm{d}^2} \qquad \text{Equation 2. 1}$$

where,

HV, Hardness Vickers,

F=0.1 kg, Force was applied for 10 s,

d=mean between d_1 and d_2,

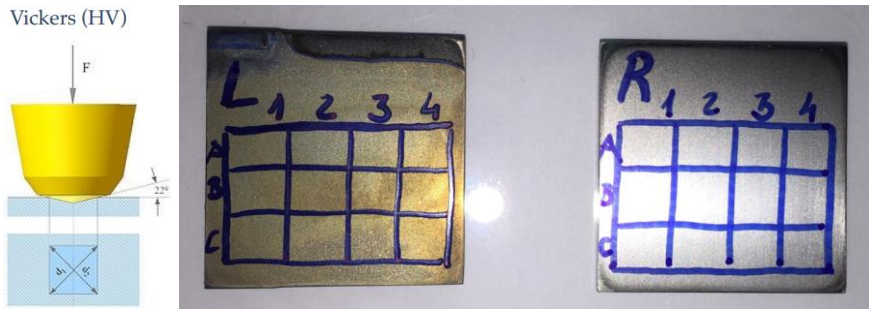

Figure 2. 5 Vickers hardness and 12 testing points in 12 different areas, TiO_2 nanotubes (L) and titanium sheet (R)

Apart from macro hardness, the substrate independence E modulus of several nanotubes was also measured by nanoindentation to analyse the micro compress behaviour of nanotubes. The measurement was performed by employing a Berkovich indenter at less than 300 nm indentation (less 10% of nanotubes layer thickness) so that substrate effects could be ignored. Elastic modulus of NT was calculated as follows:

$$\frac{1}{E_r} = \frac{1-{\nu_N}^2}{E_N} + \frac{1-{\nu_d}^2}{E_d} \qquad \text{Equation 2. 2}$$

where

E_d (elastic modulus of diamond tip)=1194 GPa,

ν_d (passion ratio)=0.07,

ν_N (passion ratio of titanium)=0.37,

E_r (relative elastic modulus) was measured by indentation.

Three different areas were selected for testing the modulus to calculate statistical results.

Surface roughness of samples was determined using Bruker contour GT-I by randomly selecting three different testing areas.

Bending and twisting is a simple but effective method to test the coating adhesive strength with a substrate. Considering each twist may lead to a different bending force, it was necessary to bend one piece of titanium substrate. Titanium foil was bent 150° to compare the strength of the attached nanotube's layer. As the nanotube's layer was fabricated on both sides of Ti foil, one surface was under tension and the other surface under compression, whereby adhesion strength could be evaluated easily. Next, the mechanical strength was evaluated under more harsh conditions. Specifically, a metal hammer was employed to continuously hit the sample (titanium foil) repeatedly times.

An ultrasonic test was performed in an ultrasonic cleaner with DI water under vibration (50 kHz) for different durations to compare nanotube peeling-off rates when subjected to friction with water. Subsequently, an industrial impact, falling ball experiment was employed to investigate the impact resistance of the samples. In a typical case, a standard 1 kg steel holder with a ball tip (10 mm in diameter) was fixed at a 500 mm height, and the free-falling body's motion was then allowed to impact the samples.

Additionally, a comparison pull-out test was carried out to test the adhesive strength of each surface nanostructure under standards ASTM D4541/D7234 and ISO 4624/16276-1. After nanotube fabrication on the titanium sheet surface, Super Glue was applied on the testing surface and then covered with a metal plate; all samples were stored in a vacuum for 24 h. Then, the pull-out tester was employed to

test coating adhesion.

To analyse the mechanical behaviour and stability of NT and SO-NT in further detail, microscopic finite-element (FE) models were established using ANSYS software. Unit bending and twisting loads were applied to the FE models of both NT and SO-NT, respectively. The deformations and stresses, which represent the material stiffness and strength, were obtained by conducting a statistical analysis.

2.3 Biotribology evaluations

2.3.1 Wear test

In this thesis, the biotribological test was mainly performed on the pin-on-disk. Two parts of the pin-on-disk experiments were employed to evaluate the biotribology performance of titanium surface, TiO_2 nanotubes (NT) and structure-optimised TiO_2 nanotubes (SO-NT). It is known that the motion of the pin-on-disk can determine the wear factor, which is based on the cross shear and aspect ratio of wear tracks [99].

A six-station pin-on-disk procedure was constructed to quantify volume loss and evaluate the wear resistance of samples. In this research, the motion of the pin-on-disk simulator combines a cyclic linear sliding 5 mm each from the central line and a 5-degree rotation of each side of the central line (Figure 2.6). The pin was fixed with a block holder, which has a bearing inside; the sliding and rotating part was a disk, and the frequency was 1 Hz. Six disks were randomly distributed in these six stations (Figure 2.6).

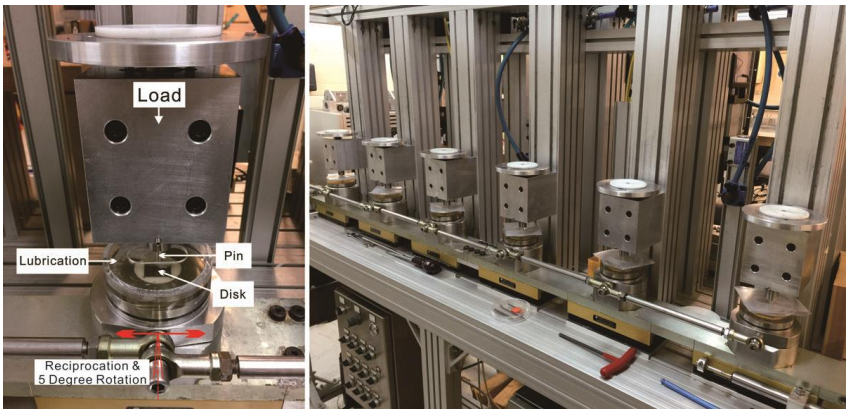

Figure 2. 6 The six-station Pin-on-Disk wear test rig, Setup of each station with load, pin, disk, and lubrication chamber, left image. Testing disks are randomly arrangement in six stations, two comparison groups (materials) are evaluated, each three of specimens are setup in stages, right image

The pin-on-disk involves two-part materials, disks and the countering part pin with relative motion, the material composition see Table 2. 3 below.

Table 2. 3 Material content of pin and disk

Pin stainless steel 316#									
Element	C	Mn	Si	Ni	Cr	Mo	Co	Fe	N2
%	0.082	0.52	0.62	0.22	27.24	5.64	Cpt	0.73	0.121
Disk Ti purity: 99.6+%									
Element	Al	Co	Cr	Cu	Fe	Mg	Mn	Ni	Si
ppm	500	2	500	200	300	20	500	500	200
Element	Sn	Ta	V						
ppm	200	10	500						

According to ASTM-G99 [100], the testing materials were tested in pairs under non-abrasive conditions, and pins in wear testing were manufactured with a radius tip. The relative wear motion was located at the testing disk specimen centre. Because the objective is to evaluate the biotribological performance of the NT or/and SO-NT layer during wear, the thickness of these layers is 2~3 μm, indicating that heavy wear (titanium substrate abrasive loss) needs to be avoided. Hence, the wear test cycles were set to 1.2×10000. This slight wear can investigate the NT layer wear resistance.

In addition, the wear conditions strongly depend on the stress at the articulating surface, which relates to the pin and disk material's properties. For example, the curvature of the pin tip can influence the stress applied on the disk under a constant loading condition. To quantify the stress at the wear interface, Hertz's classical theory of contact was used in this simulation process. The theory is focused primarily on non-adhesive contact, where no tension force is allowed to occur within the contact area and has four conditions;

1. The strains are small and within the elastic limit.

2. Each wear material can be considered an elastic half-space (i.e., the contact area is much smaller than the characteristic radius (pin radius)).

3. The articulating surfaces are continuous and non-conforming.

4. The wear materials are in frictionless contact, and all wear tests of the pin-on-disk are performed using diluted bovine serum (which has low viscosity) as lubrication during the period of sliding.

Because a slight elastic deformation occurs while the pin is contacting the surface of the disk, this area is called a contact patch and has a sphere-dome shape, as illustrated in Figure 2.7

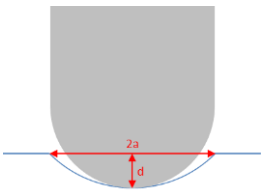

Figure 2. 7 Slight elastic deformation occurs at contacting area, as the countering pin has spherical tip, the deformation area was 2a in diameter, and the deformed depth was d

The contact area of Pin-on-disk can be calculated by equations as below,

$$s=\sqrt{Rd}=\sqrt[3]{\frac{3RF}{2E*}} \quad \text{Equation 2. 3}$$

$$\frac{1}{E*}=\frac{1}{2}\left(\frac{1-v1^2}{E1}+\frac{1-v2^2}{E2}\right) \quad \text{Equation 2. 4}$$

Where;

s-the contact area,

R-radius of sphere,

E*: Elastic modulus,

V: Poisson's ratio

The elastic modulus and Poisson's ratio of 316# stainless steel pin and titanium disk are illustrated in Table 2. 4.

Table 2. 4 Elastic modulus and Poisson's ratio of Pin and Disk

	E*/GPa	**v**
316# stainless steel	193	0.27
Ti	105	0.37

The pin was manufactured with a domed tip with a diameter of a 120 mm circle. The Hertzian stress model during the wear test was calculated for a sphere in the flat model using the theory of non-adhesive elastic contact. The initial contact stress of the pin-on-disk was 122.8 MPa and the load was $\approx$ 585 g.

The first comparative wear test compared the wear resistance of the NT surface and pure titanium surface (for the NT and Ti comparison test parameters see Table 2. 5 below).

Table 2. 5 Parameters of pin-on-disk comparison wear test for NT surface and Ti

Pin (R=60mm)	Lubricant	Contact stress (MPa)	Load (N)	Cycles (x1000)
316 stainless steel	25% diluted bovine calf serum	122.8	5.85	12

Frequency (Hz)=1, Sliding distance (mm)= 10

Apart from the wear performance of Ti and NT, a further pin-on-disk wear test was set up to compare the wear resistance of NT and SO-NT; the NT and SO-NT parameters were similar to those outlined in Table 2.5.

After the pin-on-disk wear test, each sample surface was found to have worn. The most frequently used method to evaluate wear damage is test volume loss (VL). In this study, volume loss was used to quantitatively analyse the wear resistance of Ti, NT and SO-NT. Conventionally, weight loss is one of the main measurements to quantify wear degradation of samples. However, damage to the nanotube's layer on NT and SO-NT specimens was mild, leading to difficulty in measuring weight loss. The nanotube's layer was only with 3–4 μm thick, with the coating layer also being completely detached from the substrate—the weight loss was so small that it was beyond the capability of the balance being used. Moreover, tribology behaviour of TiO_2 nanotubes is rare; this novel 'nano coating' material is inappropriate for use in traditional wear quantity methodology. Hence, a novel quantification model was applied for this study— using a TESA 90G under ISO4287 to measure the wear track then calculated by the model.

The wear track (volume loss) of the pin-on-disk can be calculated by the model below:

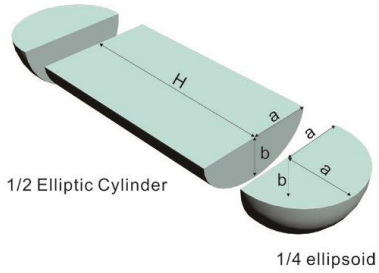

Figure 2. 8 Volume loss Model of DISKs

To calculate the degraded nanotube's layer (volume loss) at the articulating surface of the disk and pin, the wear track morphological model of the disk is described, shown in Figure 2.8. The reciprocating motion generated the wear track shaped with an elliptic cylinder (VE) with two 1/4 ellipsoids (Ve); here, these two 1/4 ellipsoids are analogously evaluated with the half-width of the wear track as two semi-long axes, and the depth of wear track was evaluated as the remaining semi-short axis. Hence, the volume of wear track can be calculated with the following formula:

$$\text{Volume loss}\,(\text{DISK}, \text{mm}^3\ ) = \frac{1}{2}\text{V}_\text{E} + 2 \times \frac{1}{4}\text{V}_\text{e} \qquad \text{Equation 2. 5}$$

where V_E is the volume of elliptic cylinder, V_e is the analogously evaluated ellipsoid. As the formula of elliptic cylinder and sphere are calculated by:

$$\text{V}_\text{E} = \pi\text{abH} \qquad \text{Equation 2. 6}$$

$$\text{V}_\text{e} = \frac{4}{3}\pi\text{ba}^2 \qquad \text{Equation 2. 7}$$

According to formula 2 and 3, the formula 1 is given by:

$$\text{Volume loss}\,(\text{DISK}, \text{mm}^3\ ) = \frac{1}{2}\pi\text{abH} + \frac{2}{3}\pi\text{ba}^2 \qquad \text{Equation 2. 8}$$

where a is the semi-long axis of the elliptic cylinder (here, it is the profile of semi wear

track width), b is the semi-short axis of the elliptic cylinder which is the depth of the wear track, and H is the length of the elliptic cylinder as the length of the wear track (sliding distance).

According to the wear testing pin wear trace, the volume loss of the pin was approximated as a half ellipsoid geometry—the equation for determining the volume of the ellipsoid on the spherical end pin is as follows:

$$\text{Volume loss (PIN, mm}^3\text{)} = \frac{2}{3}\pi abc \qquad \text{Equation 2. 9}$$

where a is the radius of the ellipsoid long x axis, is the half-long of the wear trace value,

b is the short axis, is the half-short wear trace value,

c is the height of ellipsoid, is the depth of wear trace value (Figure 2.9).

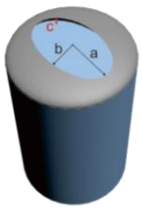

Figure 2.9 schematic Volume loss model of pin

By the volume loss model above, the Ti, NT and SO-NT worn tracks were measured and estimated. To further analyse the wear degradation, the wear track was observed and compared by SEM and a MicroXAM 3D noncontact surface mapping profiler.

2.3.2 Friction testing

A pin-on-disk wear test can characterise the wear resistance of materials. However, the biotribology behaviours of materials include wear and friction. The friction test is

also a key evaluation approach to study material tribological performance systematically. The friction test was also carried out in this study; in particular, the friction coefficient value was also tested using a ball-on-disk reciprocating tribometer (CSM). A PTFE ball (ϕ=10 mm) as a counterpart in 0.1 g/ml bovine serum albumin lubrication was placed under a 2 N load at 1 Hz constant frequency for 120 min. Compared with the pin-on-disk, the ball-on-disk was carried out to measure the coefficient of friction (COF); during the sliding test, the COF was recorded using a tribometer, which is a common tool for tribological analyses. After the 120 min friction test, the wear track was analysed and compared. For parameters applied to the ball-on-disk test, see Table 2. 6.

Table 2. 6 Parameters of ball-on-disk friction test

Ball (ϕ=10 mm)	Lubricant	Contact stress (MPa)	Load (N)	Cycles (x1000)
PTFE	0.1 g/ml bovine serum albumin	20.1	2	7.2

Frequency (Hz)=1, Sliding distance(mm)= 10

2.3.3 Fretting screw model

Based on the basic biotribology test, the titanium surface, NT and SO-NT were evaluated by pin- and ball-on-disk methods for wear resistance and friction. However, clinical orthopaedic and dental devices are designed with diverse curved surfaces, such as screw threads, and present more complicated stress distribution and tribology behaviours on the implant surface. Particularly under massive loading, and due to the transmitted mastication loads, dental screw implants are subjected to cyclic

micro-movements at the bone-implant interface, inducing wear [101, 102]. Fretting corrosion is one of the main degradation forms and affects the failure of the bone-implant interface; the inserted implants have relatively low micromotion with the healing bone and generate wear debris during the process. Furthermore, biocorrosion is another dominant factor that co-relatively acts with the mechanical fretting process. Clinically inserted titanium implants are surrounded by blood-rich tissue, and the serum protein in blood can affect implants' corrosion behaviour. Regarding biotribology of titanium implants, tribocorrosion is an irreversible process that occurs at the bone implant's interface, leading to its failure [103, 104]. Hence, to evaluate screw fretting and corrosion behaviour for NT and SO-NT, both surfaces were generated on the Ti_6Al_4V medical-grade screw surface, and the wear and corrosion degradation processes were studied comparatively with pristine machined screw surfaces.

NT and SO-NT were grown on Ti_6Al_4V medical-grade (TC4) veterinary fixation screws (3.5 mm major diameter and 26 mm length, self-tapping screw, Shanghai Huifu manufacturing Co., Ltd). The screws were sequentially cleaned in an ultrasonic cleaner for 15 min with acetone (99.5%, Fisher Scientific), ethanol (99.8%, Fisher Scientific) and DI water, then air-dried. The first anodisation was performed in ethylene glycol (EG, 99.5%, ACROS Organics) with 0.5wt.% NH_4F (98%+, ACROS Organics) for 30 min, followed by sequential, additional anodisation in EG with 3wt.% H_3PO_4 (85%+, Fisher Chemical) for 1 min. After both anodizations, SO-NT was rinsed with DI water and dried with a N_2 stream. NT fabrication applied the same procedure without additional anodisation. Parameters are shown in Table 2. 7.

Table 2. 7 Parameters of fretting model

Bone	Lubricant	Temperature (°C)	Load (N)	Cycles (x1000)
Fresh sheep formal	none	37	100	36

Frequency (Hz)=10, Sliding distance(um)= 300

We chose fresh sheep femoral bone as our ex-vivo fretting counter for screws because the micromechanical properties are altered in dehydrated bone [105]. The middle part of the femoral bone was collected from a local abattoir within 2 hours of sacrifice. Each screw sample was inserted in each new fresh bone to confirm tight contact between the bone and screw interface. Before insertion, a hole of 3 mm in diameter was drilled in the centre of the bone, and each self-tapping screw was inserted into each femoral bone. The mechanical setup is used to simulate the shear applied from bone to screw in vivo, and shear is vertically applied to the screw (please see Figure 2. 10). Fretting was achieved using an SRV-IV oscillating reciprocating friction and wear tester. A 100 N load was applied on the screw head vertically, with 300 μm fretting distance at 37 °C. A frequency of 10 Hz was applied for 60 min fretting testing, with 36×1000 cycles.

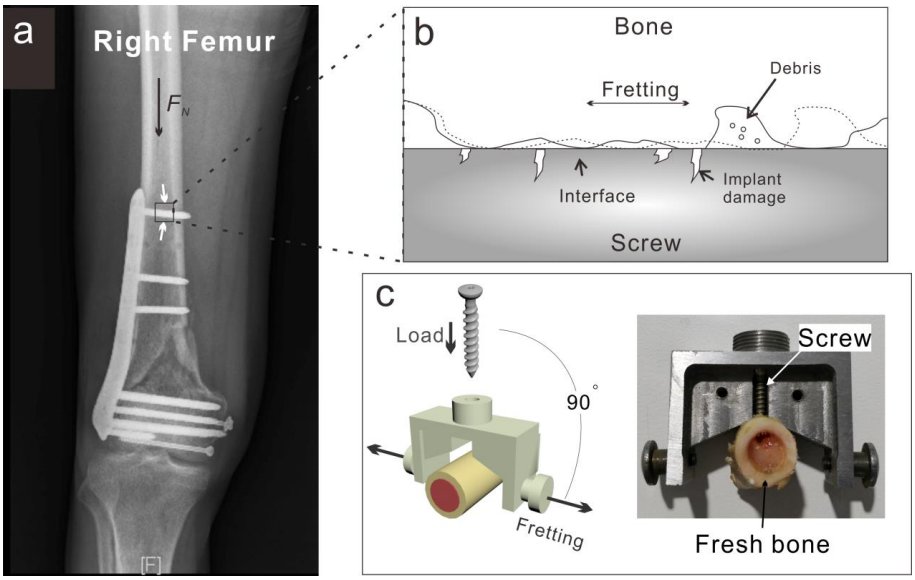

Figure 2. 10 Schematic of fretting at bone-implant interface: Fretting behavior of inserted injury fixation screws (a), load vertically applied on screws, fretting behavior at bone-implant interface, the fretting leads to implant surface damage and wear debris generation (b) and mechanical setup (c)

FESEM (JEOL-7601) was carried out for topography observation of screws before and after the fretting test. Bare Ti_6Al_4V, NT and SO-NT topographies were all measured under the same magnification for comparison purposes. Orthopaedic screws' wear damage included short-term wear during insertion and long-term fretting in vivo. The self-tapping screw thread faces mass stress and heavy rubbing while drilling in installation, and the cortical bone can mechanically remove the material on the thread. After insertion, due to the tight contact, the bone thread interface may lead a more severe fretting damage than other areas. Thus, the wear tracks on the thread were compared by SEM measurements. As aforementioned, the NT layer is featured with micrometres thick film; because of the low level of damage, conventional quantitative wear methods, such as weight loss, are unsuitable for determining nanotube damage.

2.4 Biocorrosion measurement

Biocorrosion plays a vital role in the degradation of orthopaedic implants [9]. As a thin layer of metal oxide film forms on the metal surface under an oxygen atmosphere, the metal substrate is protected by this natural film. However, while the metallic implants make contact with bodily fluids, the aqueous environment with mass ions, protein and cells would 'degrade' this passive film—the exposed biomaterial leads to corrosion damage and ion release into surrounding tissue[104]. Therefore, to characterise the titanium (alloy), NT and SO-NT systematically, the biocorrosion test was performed to test open circus potential (OCP) achieved in E versus time in simulated body fluid solution (SBF). Electrochemistry measurements were carried out by CHI660D (CHI Co., Shanghai, China) to evaluate corrosion resistance. The OCP measurement is an important source of information on the chemical reactivity of materials immersed in liquids, and it denotes whether or not there is a pre-disposition to corrosion. Different OCP values indicate the different electrochemical states of a material, reflecting its active or passive state. An increase in the OCP (anodic shift) displays a more passive state and on the contrary, a decrease (cathodic shift) indicates a more active state. After a period of OCP stabilisation, a dense and passive oxide film of a few nanometres is expected to be present on Ti smooth surfaces, and the OCP stabled value is also related to the sample’s physiochemical properties, such as microstructure. A higher OCP value of a material indicates its reduced activation in the eroding environment.

The apparatus for electrochemical measurements consisted of a three-electrode electrotank, corresponding to an OCP of ± 250 mV with a scan rate of 0.3 mV s^{-1} at room temperature, a saturated calomel electrode as a reference and platinum foil (Goodfellow) as a counter electrode. The polarisation was recorded after soaking in SBF until stabilisation, and scan data were selected for 1500 s. The screw samples were also tested for OCP. Before the fretting test, the OCP curve of three screws was recorded for 1200 s, with a comparison with the OCP being performed after the fretting test. All screws were washed with DI water and alcohol for 15 min in an ultrasonic bath before the biocorrosion test.

To summarise, the NT and SO-NT were fabricated on pure titanium, alloy and medical devices by anodisation methods under specific parameters illustrated in this chapter. With the generated materials, the physiochemical properties were systematically characterised. In particular, the biotribology performance was determined in terms of friction and wear, and biocorrosion behaviours were also evaluated.

Chapter 3

3.Retrieval analysis of orthopaedic bone screws

Retrieval analysis of failed implants plays a key role in assessing the *in vivo* performance, identify issues that influence the implants *in vivo* performance. In this chapter, two typical clinical failure cases were analyzed, one case was the aseptic loosening of fixation screws retrieval from femoral neck fracture fixation. Screws were subjected to fretting corrosion which led to discoloration, pitting attack, and cracking. Fretting corrosion may as a dominated factor to screws failure. Second case failure was mainly caused by fatigue corrosive fracture of screw, stress, biocorrosive atmosphere and the cyclic load applied on screw can increase the fracture risk of fixation screw, especially at screw plate contacting region. The retrieval analysis was mainly focused on the implants performance, especially the degradation mechanism at the bone implant interface. Both failure cases were caused by various factors, and the poor osteointegration was one of the most important precondition leads to a limited biomechanics performance of implants.

3.1 Introduction

3.1.1 Screw fretting corrosion retrieval case

Hip fracture is a major public health issue and is likely to be continued as one due to the ageing population resulting in a significant amount of morbidity and mortality, and fragility fracture is the commonest type of fracture in older patients with osteoporosis or osteopenia. Fractures of femoral neck generally necessitate surgical intervention with either internal fixation or arthroplasty.

Displaced fractures of the femoral neck are typically treated with arthroplasty, whereas internal fixation is a better-suited treatment for undisplaced fractures [106]. Treatment of choice varies according to degree of displacement, patients' age, bone quality, level of activity, and premorbid mobility [107, 108]. Internal fixation remains the treatment of choice for patients without degenerative changes in the hip joint and also in displaced fractures in the younger patients, where preservation of the femoral head is the priority [109]. The rationale behind using multiple screws for internal fixation include less invasive surgery, enhanced rotational stability and preservation of more cancellous bone compared to large screws [110-114]. Anatomical reduction can be achieved using cancellous screw fixation or dynamic hip screw (DHS). The DHS prevents varus displacement or rotational instability due to the locking plate feature, whereas the cancellous screws offer less invasive surgery, shorter operation time, less blood loss when compared to DHS [110-117]. Despite screw fixations advantages, a failure rate of 20-36 % have been reported for cancellous screws [118, 119]. In terms of

failure causes, osteolysis or loosening, dislocation, migration, infection, and malpositioning wear and mass loading, can lead to implants failure [120, 121]. Both biological and mechanical factors can affect the longevity of implant [122, 123]. However, retrieval reports are mostly focused on joint replacement cases with severe wear and the fretting corrosion of screws are hardly been reported [124]. Although internal screws are with mild wear compared with the wear of knee and hip replacement, the orthopaedic screws are inserted in bone tissue surrounded blood-rich tissue and adjacent the nerve in spinal fixation. The lifted off wear debris can cause around tissue reactions. Fretting corrosion at one implant interface can also cause mild such as discoloration or severe tissue reactions that affects implants life span. Fretting is common in orthopaedic refers to friction process involving micro moved amplitude displacements, more precisely displacements with a total amplitude smaller than the contact width. Moreover, the aqueous environment in-vivo with corrosive medium also contributes to generate and accelerate wear process [125]. For example, fretting corrosion behaviour of one cemented (PMMA, polymethylmethacrylate) hip joint prosthesis (316L steel) was deeply investigated by Jean and co-workers with using model system [126]. Compared with the 316L steel/PMMA wear volume loss while was fretting in air, the volume loss of PMMA slightly lower in Ringer's solution. Obviously, the 316L steel degradation was faster than that in air and it is due to the corrosion process. Degradation of the passive layers on the metal implants surface by the fretting causes an anodic dissolution that is strongly enhanced by the confined character of the contact zone (crevice effect) [126]. Fretting corrosion not only occurs at

bone-implant interface on hip stem, but also observed in modular components of spinal implants, screws and rods [127]. Although titanium alloy has improved corrosion resistance than steel, the titanium implantation also can be damaged by fretting corrosion. Studies have shown that titanium based implants degradation lead to as peripheral neuropathy, osteomalacia and Alzheimer disease due to the release of aluminum and vanadium ions in tissue. Vanadium and its oxide (V_2O_5) have been widely proved to be toxic to cells [128]. The corrosion process of Ti_6Al_4V is because of the dissolved of vanadium oxide in passive film, vacancies generated and diffused on the oxide layer of the implants [129].

The first retrieval case is, by investigating a typical degradation of three failed screws at bone implant interface, to reveal the degradation such as fretting corrosion mechanism on locations of screw. Long term fretting-corrosion of the implants has been discussed in details. Moreover, the formed stress corrosion was detected and analyzed. This research could give the further understanding of screw wear degradation procedure. Meanwhile, the retrieval analysis has stated a further biomechanical demand for the surface modifications with potential to be applied to the screws.

3.1.2 Fatigue fracture bone screw retrieval case

The main goal for surgical treatment of bone fracture is to restore the function of the injured limp, stable internal fixation gives the primary strength to bone, allowing early functional mobilization [130]. One of common orthopaedic fractures is the femoral shaft

fracture – an high energy injury frequently associate with life-threatening conditions. The Locking Compression Plate (LCP) fixator is the mostly used device to immobilize the femoral fracture. However, bone screws implant failure cases were also commonly reported by revision and retrieval analysis [131]. Two factors could affect service life span of inserted implants, i.e. mechanical and environmental factors [132]. Mechanical factors include implants fatigue, tribological degradation and fretting, environmental factors are commonly focus on biological corrosion process. Especially, fatigue failure, a process of defect accumulation, from crack initial generation and propagation with cyclic loading, can cause the breakage of bone screw. Furthermore, screws fatigue is also combined with corrosion attack, the corrosion fatigue can cause the fracture of screws [133]. Screws fracture can cause the failure of internal fixation and lead to twice injury of patient. Thus, orthopaedic engineers put great effort to optimise the biomechanical stability of bone screw from both clinical performance and implants designing [134-136]. Stress concentration is commonly suspected to be the main cause of screw breakage, and screw fracture is usually at the joint area of screw shank and head [137]. In fractured femur fixation cases, various types of forces act on the plate, screws and the femur, especially while the cyclic load applying on fixation system during walking, the complex forces transmission increase the risk of implant failure. Herein, a broke cortical bone screw has retrieval analyzed, fracture surface was observed and stress distribution has been simulated by finite elements analysis (FE analysis), and the mechanism of screw fracture was discussed in details.

3.2 Fretting failure of fixation bone screw

3.2.1 Case report

In this case, a 61-year-old male (170 cm height, 66 kg weight) patient's right hip was internally fixed due to displaced femoral neck fracture (injury) with multiple 7.3 mm cannulated screws (self-drilling Ti-6Al-7Nb screws, DePuy Synthes). At the time of the surgery, patient had no significant medical comorbidities. Two short thread and one long thread screw were inserted, and one of the screws were stabilized with a washer (screw 1). One year after implantation, pain was firstly felt in right hip, and the pain led to patient limp and limited activation. After five years insertion, screw loosening and avascular necrosis of femoral head was diagnosed. Before retrieve screws, the routine inspection of blood tests were carried out, erythrocyte sedimentation rate (ESR) exhibited a normal value = 16 mm/h, C-reactive protein (CRP) = 0.83 mg/L. Both ESR and CRP were at normal range and based on values, the diagnose of avascular necrosis of the femoral head was priority to be considered. The clinical CT taken at the time of revision surgery showed necrosis of the femoral head and severe bone resorption adjacent to the screws, indicating aseptic loosening failure of the fixation screws. The failed screws were retrieved after five years and the patient underwent total hip replacement procedure. In general, potential reasons for revision surgeries can be classified into inadequate surgical techniques, patient-related factors, and implant-related factors. Inappropriate implant position and inadequate preloading results in implant loosening. The CT image showed that the screws were unparalelled

(three screws were paralelled while insertion) and thus the next step was to investigate surgery process and implant related factors (Figure 3. 1).

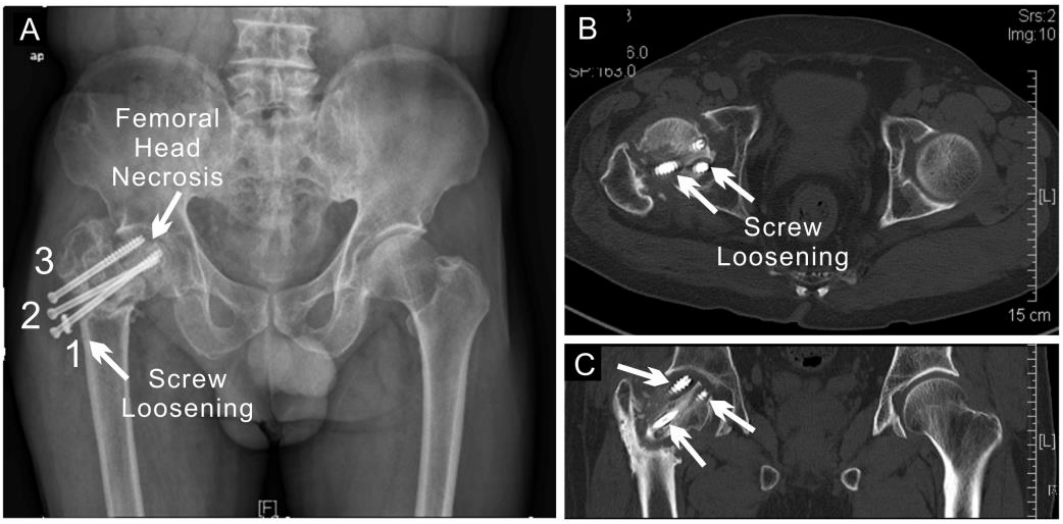

Figure 3. 1 CT scan of screws loosening and avascular necrosis after five year implantation: the front view of 1,2 and 3 screws location (A), the top view of CT scan, gap at bone implant interface can be detected clearly (B), obvious femur head resorption are observed adjacent screws (C)

3.2.2 Fretting induced failure analysis

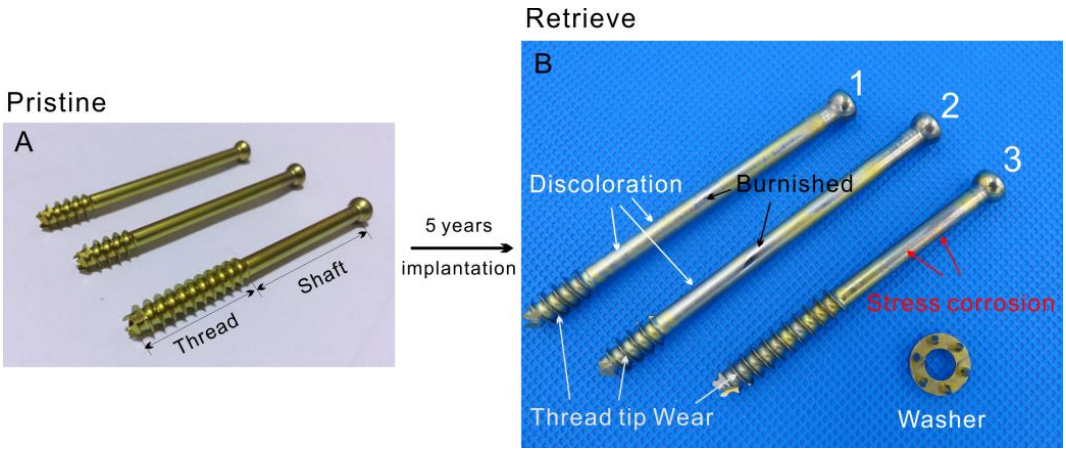

Figure 3. 2 Comparison optical image of pristine screws and degradation of screws, pristine screws (A) and retrieval screws discoloration located on both shaft and thread areas (B)

The screws were originally with gold colour as can be seen from the pristine screws

(Figure 3.2A). However, after five years three screws were worn severely with an evident colour change as a result of long-term fretting. Corrosion and fretting damaged was identified according to Goldberg et al [138]. A region was described corroded when altered optical properties including discoloration and loss of reflectivity was observed. Fretting was defined as mechanical damage to surfaces, resulting in plastic deformation and material removal, or burnishing resulting in regions of increased reflectivity. Among the three screws, screw 3 was less worn compared to screws 1 and 2.

Thread wear during insertion

The threads of all screws 1, 2 and 3 was facing a more heavy worn in insertion. Tip area on thread was analyzed by SEM-EDX (Figure 3. 3D). Wear on thread ridge was examined by SEM. It was observed that micro sized pits were consistently distributed on one side of the blade (Figure 3. 3D2, A side), on the other side (Figure 3. 3D2, B side), the articulating surface was more smooth and without obvious pits. This phenomenon indicates two different wear mechanism of each side on tip surface. Wear on side A (operative installing direction) was dominated by adhesive wear. As the initial of installation, cortical bone was first contacted with side A, as the screw was drilling forward and squeezing the bone, the mass stress was concentrated on side A. Due to the heavy wear damage, bone tissue was removed and debris was generated on the articulating surface. The debris was trapped and rolled on contacting interface, damaged the surface of thread tip, and left the pits topography. The EDX results proved the bone material has been transferred to side a, carbon,

calcium and phosphorus. In contrast, side B maintained an integrate surface and without traces of bone tissue. The difference in the wear pattern between side A and side B is clearly shown in Figure 3. 3D2.

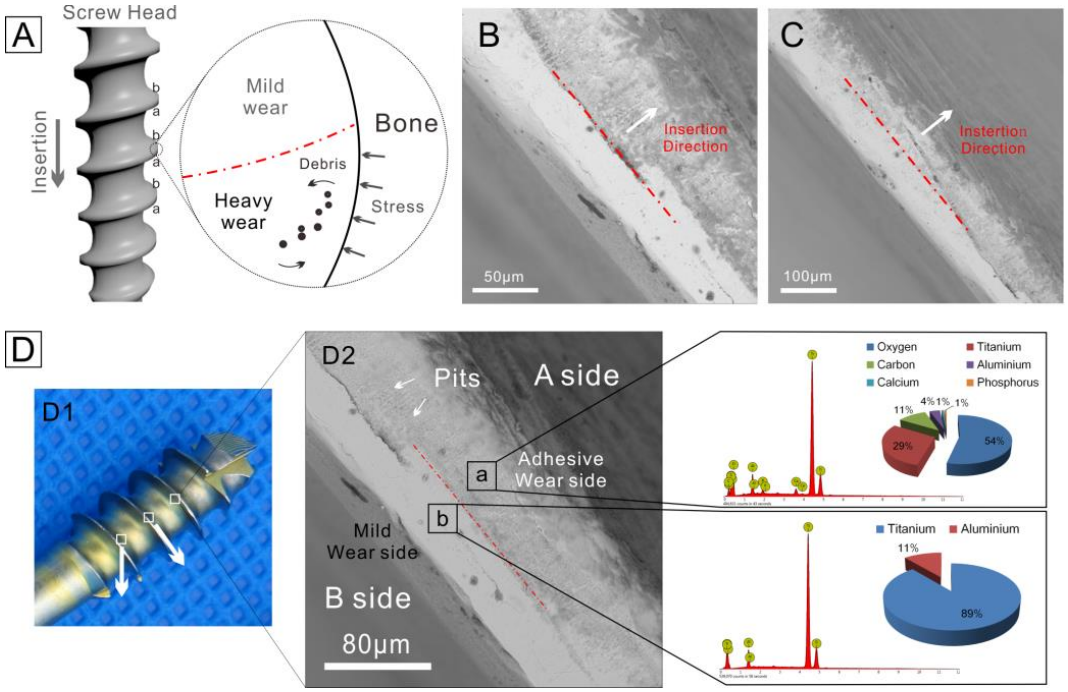

Figure 3. 3 Schematic images of insertion wear, schematic illustration of insertion wear mechanism at thread tip (A), SEM images of wear scar on the threads tip (B) and (C), optical image and EDX analysis of thread tip on area a and b, (D, D1 and D2) Different position were examined for more representive. It is revealed that the adhesive wear marks were distributed along the thread, as shown in Figure 3. 3A, B and C. Therefore, the operative installing direction side on thread tip were under more intense friction conditions, and more damage were observed.

Fretting corrosion

Apart from wear caused by insertion, fretting assisted biocorrosion is the main damage mechanism during the implantation life time. Fretting assisted biocorrosion occurs while two surfaces in contact with micro relative motion. The existence of

crevice at bone implant interface is one of the prerequisite of fretting assistants biocorrosion. Fretting on all three screws were obviously as observed from the colour exchange. The colour from initial gold colour changed to titanium.

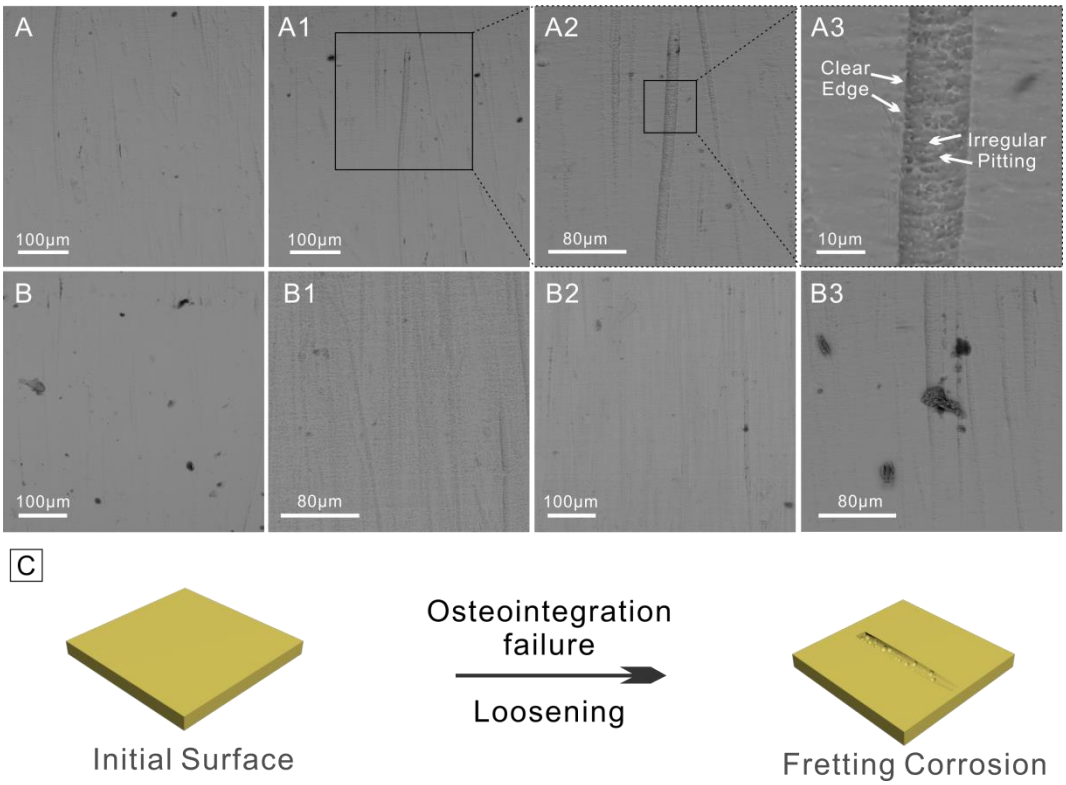

Figure 3. 4 Fretting corrosion wear scars, a, a1, a2 and b, track formation, c

Fretting corrosion is the one of main damage mechanism during the implant service life time It occurs while two surfaces in contact are in relative micromotions [126]. When screw 1 and 2 was viewed under SEM (Figure 3.4), the shaft was covered with randomly ordered scratches featured with above 100 μm in length. Higher magnification SEM images of the scratches revealed irregular pitting which may have formed by erosion over time. As shown in Figure 3. 2 , the areas with fretting corrosion pits featured a shiny/burnish surface on screw 1 and 2. However, as long term fretting corrosion condition in the bone tissue, the wear track was having more

tendency to be eroded, prone to be further damaged by corrosive body fluid.

Regions without fretting scar were also examined (Figure 3. 5). The surface was subjected to fretting corrosion and uniform distribution of pits were found on the surface of screw. The size of irregular pitting were 10–20 micrometers, meanwhile, pits were extensive and uniform distributed on the screws surface. As revealed from the optical microscope examination (Figure 3. 2), the areas with pits were exhibited a shiny/burnished surface. Moreover, the extensive distributed pits generated by fretting corrosion are one of main evidence of screws mechanical loosening.

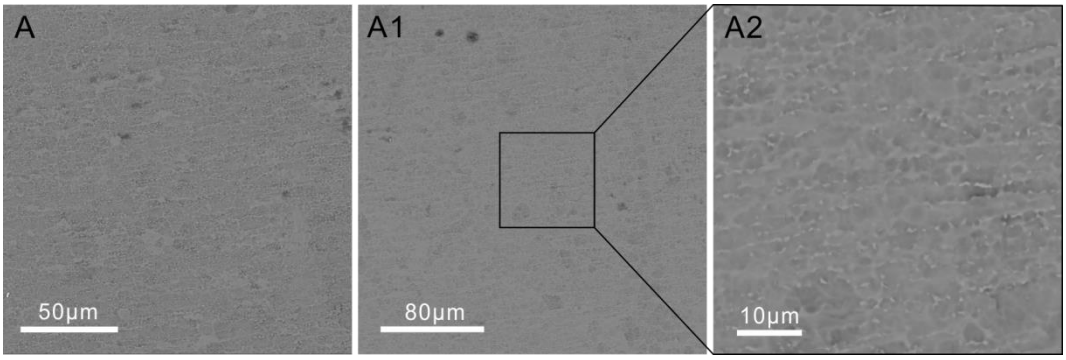

Figure 3. 5 Fretting corrosion morphology features on screw 1 and 2 shinny (burnished) areas, screw 1 widely distribution (A) and specific features on screw 2, (A1) and (A2)

Stress corrosion

From optical image, screw 3 on shaft part exhibits a mass distribution with colorful small dots, as shown in Figure 3. 6 optical image. Form the magnified SEM image, the grey area displayed a 'cracked land' topography, featured with sharp angle. The micro-cracks linked with each other before broke. This is characteristic of stress corrosion cracking. EDX analysis were carried out to compare the scanned shrunk film (area a) and substrate surface (area b). EDX analysis of both regions

demonstrated presence of Oxygen (O), Aluminium (Al) ,Titanium (Ti), and Carbon (C) elements. The high percentage of oxygen (region A:62% and region B:51%) indicated exposure of oxygen diffused layer. The considerable percentage of Aluminium element (region A :3% and region B:5%) suggested decreased thickness of the oxide layer and exposure of bare titanium alloy. Furthermore, high content oxygen and carbon on screw 3 indicated presence of biological elements from proteins.

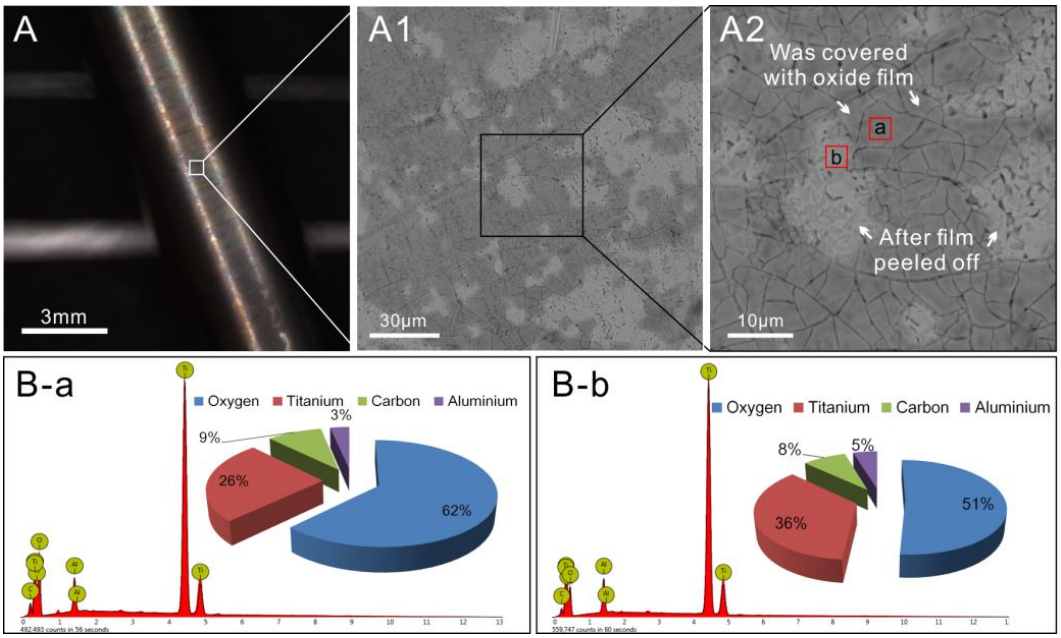

Figure 3. 6 Stress corrosion on screw 3, Optical image (A), SEM images of stress corrosion areas (A1 and A2), and chemical composition of area a and b (B-a and B-b)

Figure 3.7 illustrates the difference topography features between stress corrosion and fretting corrosion surfaces. As the stress corrosion strongly depends on the stress distribution on screw, that generates with angle cracks, however, topography of fretting corrosion shown with open type damage (pits), indicates the material was removed by mechanical shear.

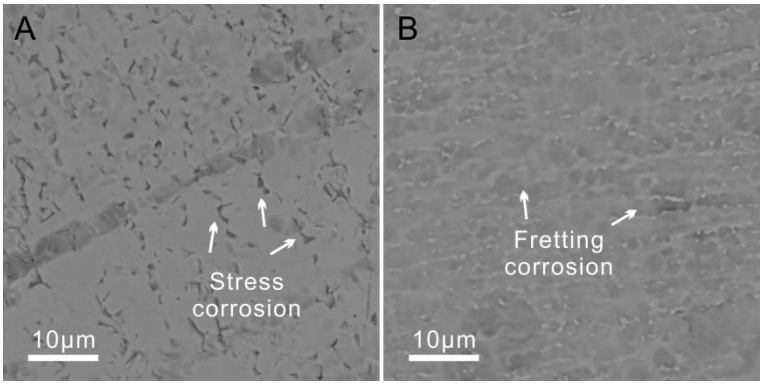

Figure 3. 7 Comparative SEM images, stress corrosion topography featured with angel edge cracks (A) and fretting corrosion topography (B)

Table 3. 1 The main degradation of Screw A, B and C

	A	**B**	**C**
Shaft (burnished areas)	Fretting corrosion (pits < 20 μm)	Fretting corrosion (pits < 20 μm)	Stress corrosion (cracks)
Shaft (discoloration)	Fretting corrosion (scratches > 100 μm)	Fretting corrosion (scratches > 100 μm)	
Threads	Insertion wear	Insertion wear	Insertion wear

Discussion

This case study documents the reasons for failure of three internal fixation screws retrieved from a patient after 5 years in vivo. Here, we have visually and microscopically investigated for signs of degradations. Typical features observed among the screws include pitting attack, scratches and cracking. Corrosion is a process of degradation of material into its constituent atom due to occurrence of chemical reactions between material and its surroundings, it is also the process of unstable metal changes in the material's thermodynamic state and electrochamical oxidation of metals in reaction with oxygen [139]. The presence of corrosive elements in human body such as hydrogen ion (H^+), dissolved oxygen, free radicals (O_2, O^-), sulfide compounds (S_2^-) and chloride ion (Cl^-) affects the corrosion behavior of

implantable materials [140]. The most common types of corrosion in titanium orthopaedic prostheses can be classified as pitting, fretting, galvanic, and crevice corrosion. When the passive TiO_2 layer on a flat surface is disrupted by acid, pitting corrosion occurs. Moreover, repeated micromotion or friction between the TiO_2 layer and another material cause mechanical wear and breaks up of the passive layer and it is known as fretting corrosion. The three screws in here were all moderately affected by fretting corrosion. Discoluration, dullness and burnishing was observed in all screws. Micromotions causing the fretting corrosion can be result of inadequate mechanical fixation at the time of surgery or reduced bone healing capacity due to avasuclar nercrosis. Furthermore, a cracking pattern was also observed in screw C shaft which indicates the presence of stress corrosion cracking. However, the mechanism for crack initiation and propagation is not clear. It has been suggested that cracks could initiate by fretting and propagte by stress corrosion craking [141]. K.J.Bundy showed that crack like phenomena can occur in vivo at a stress level of σ_y (yield stresss) after short period of time [142]. Corrosion of the metal implants may jeopardize the integrity of the surrounding tissue and mechanical stability of the implant. When the metal ions are released from the implant surface or particulate metallic wear, they either remain in the intercullular spaces near the site where they were released or migrate systemically. The release of these ions activate the immune system and subsequent release of proinflammatory factors and chemical mediators which have shown to result in cascade of events leading to periprothetic osteolysis. In the present investigation, fretting promoted the removal of the TiO_2 layer and release

of oxide and metal debris which may have contributed to osteolysis and loosening as observed in the CT scan (Figure 3. 1).

It is advocated that fracture reduction and stable fixation should be performed as a surgical emergency in an attempt to restore blood supply to the femoral head and prevent further complications including avascular necrosis (AVN) and non-union. The incidence of the named complications have been reported to be 10-30% and 20% respectively [143-146]. AVN and non-union of femoral head leads to segmental collapse of the head which predispose to secondary hip joint degenerative changes, necessitating revision surgery. Lakkol et al evaluated the failure rate among fixation devices for undisplaced fracture neck of femur in 52 patients and found 36% of patients had reoperation [147]. The reason for revision was failure of fixation in 88% and avascular necrosis in 11% of the patients. Manohara et al aslo reviewed the outcomes of cancellous screw fixation for undisplaced femoral neck fracture in 96 patients [148]. The patients were followed up for a mean of 39 months, 8 underwent revision for avascular necrosis (AVN) of the femoral head (n=5) , and for non-union/ implant failure (n=3). The case reviewed here also suffered from AVN. The fracture was treated 4 hours after the incidence. Khoo et al reported no cases of AVN when the fracture was reduced and fixed within six hours but the incidence increased with increasing time interval. The vascularity of the head can be affected by intial trauma and also inadequate fracture reduction [109]. However, no signs of AVN was observed at the time of the surgery in this case.

In another clinical study nonunion, osteonecrosis, stress fracture of the subtrochanter,

excessive pull-out of a screw , and deep infection were major complications reported for undisplaced femoral neck fractures [107]. Bacteria present on the surface of the implant or biofilm formation can cause pitting and discolouration of implants. To determine if periprosthetic infection was a contributing factor to the failure of the screws, we analysed the serum biomarkes prior to implant removal. For any patient undergoing revision total joint arthroplasty ESR and CPR are standard screening tests regardless of the cause of faiure. Ghanem et al. showed that CRP of 10 mg/L and ESR of 30 mm/hr have a sensitivity of 97.6% if combined [149]. We found CPR of 0.83 mg/L and ESR of 16 mm/h which were not indicative of infection.

For the surgical technique, the fixation screws of femur head are widely accepted should be parallel to each other, and the insertion triangle configuration is usually favoured due to it increased mechanical stability [150, 151]. However, three parallel cannulated screws has been documented with its possibility of inappropriate fixation strength especially when osteoporosis presents, and the initial interfragmentary compression of these construction is insufficient frequently. Due to the close insertion of three screws, the entry points localised in thin section, leads to the lacking appropriate lateral cortical support [152].

In the case, the patient was no osteoporosis diagnosed as the fracture fixation, however ,the three screws were lacking of sufficient loading and compression at the initial insertion which may cause the failure of osteointegration in early stage. Another concern is insertion angle, higher insertion angle is proved with better fixation strength [153]. The insertion angle of this case was 107-120 degree lower than 135-150 degree,

the lower insertion angle also effected the torque and stress distributed at bone screw interface.

Above all the factors including surgery technique and implant performance, led to three screws loosening failure. This case is meaningful to develop osteointegration improved surface coating, with enhanced anti fretting corrosion properties, and also valuable to the surgery operation optimization.

3.3 Retrieval case report: fatigue failure

3.3.1 Case report

One LC-DCP plate and eleven medical grade Ti_6Al_4V screws were fixed into a 58-year-old male patient diagnosed with right femur fracture by accident. During bone healing process, the patient was without obvious pain, with no movement limitation and inflammation, and no weight loss was observed. After 19 months bone healing, the femur was healed, internal fixation implants have been removed. In clinical removal, a fractured screw were observed inside the femur (cancellous bone area), however, the CT scan displayed no obvious screw broke, deformation or displacement, see Figure 3. 8. The screw marked with red arrow were broken in bone tissue. After retrieval other screws and plate, the broken screw has been removal hardly.

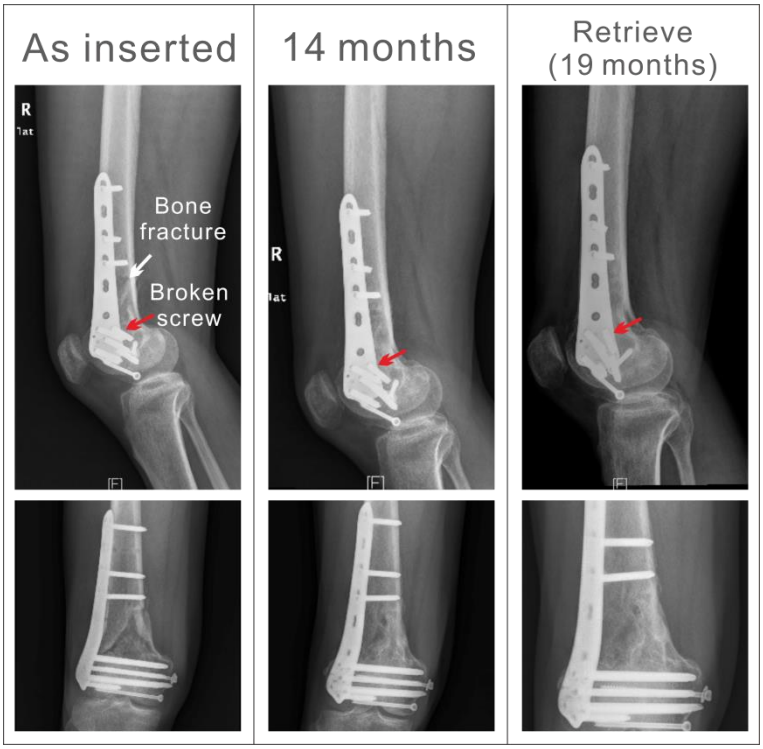

Figure 3. 8 CT scan images of internal plate and screws fixator inserted in right femur in patient, by as inserted, after healing 14 months and before 19 months retrieval. Femur fracture area is marked with white arrow, and the fractured screw is marked with red arrow

3.3.2 Fatigue failure analysis

The as retrieved broken screw was ultrasonic cleaned 30 min in alcohol and distilled water separately, then brush cleaned the fracture surface, and blow dried with N_2 stream subsequently. The fracture surface of screw was detected by Scanning Electron Microscope (SEM, JSM-5600LV, JEOL company, Japan), retrieval screws plate fixation system and broke screw optical image, see Figure 3. 9. The surface of broken screw was smooth and no obvious defect could be detected.

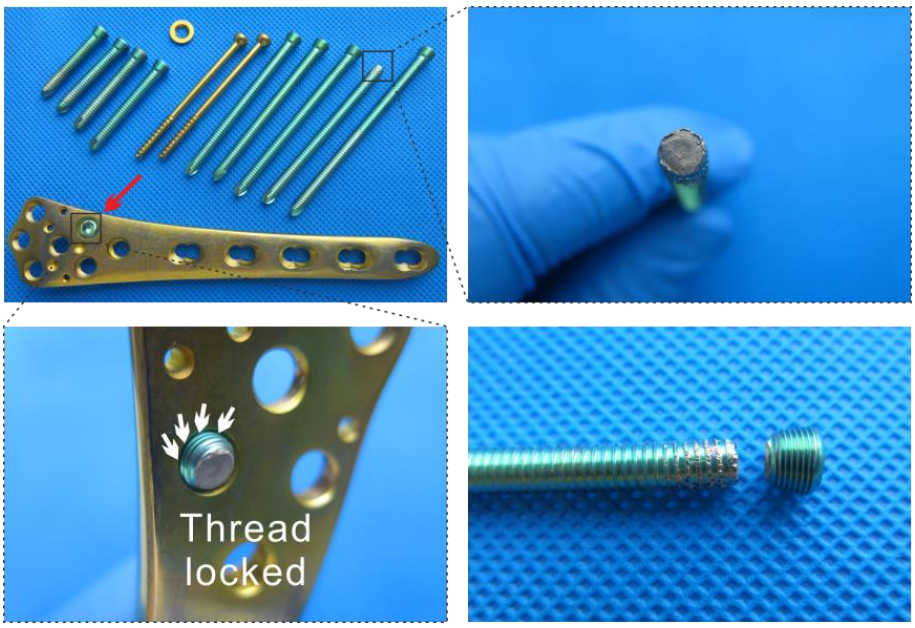

Figure 3. 9 Optical image of as-retrieved screws and plate fixation system, fracture screw (red arrow), breakage screw part thread was locked with plate thread (white arrows)

Meanwhile, the stress distribution was analyzed by finite element (FE), especially the stress distribution at the fracture interface area. Considering the patient weight and femur stress condition, 800 N equivalent load was applied for the simulation.

Figure 3. 10 shows the morphology of fracture surface. The fracture morphology exhibits a typical fatigue fracture failure, from Figure 3. 10 c and e, indicates the cyclic crack propagation though the fine grain structure, black arrows. The shear loading transmit from femur to knee (Figure 3. 10 b to d), the fatigue fracture initial area might start from area of femur side (Figure 3.10b.).

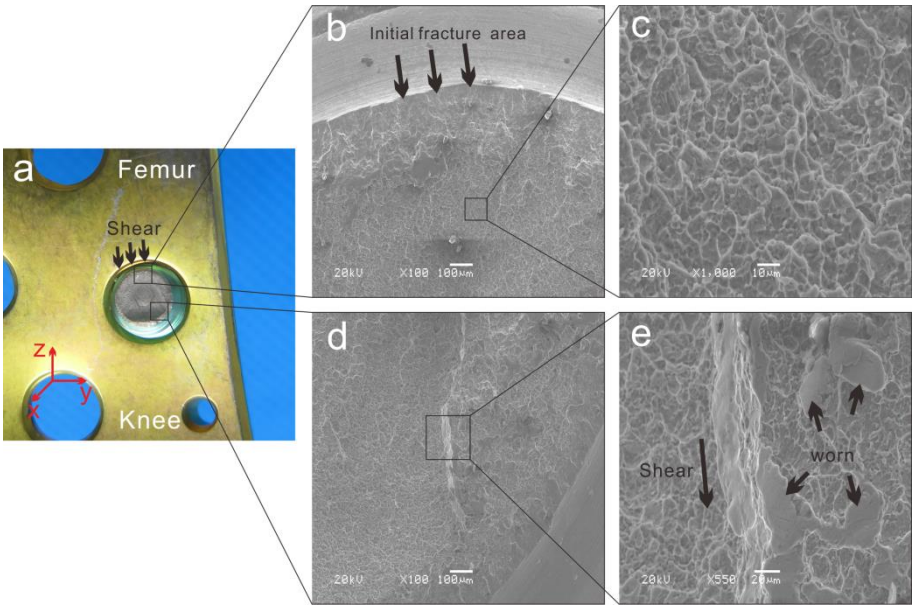

Figure 3. 10 The SEM images of fracture topography. Shear applied from femur to knee, the opposite direction z axis, shown in a. The initial fracture area (b), magnified fracture topography shown typical fatigue breakage (c). Breakage end topography with step topography, magnified step and worn areas, marked with black arrows (d)

Furthermore, several worn areas was analyzed on fracture surface, featured with wear tracks located on flat surface, the flat surface has compressed and worn (Figure 3. 11). The worn tracks has demonstrated that the fretting at fracture interface was presented even after the screw broken. Meanwhile, the CT scans images were also displayed no obvious dislocated of fractured screw. The possibly mechanism was due to concentrated cyclic shear stress at screw plate connect area, the fatigue leads to screw broke, however, each part were still contact and with relative micromotion. However, the wear tracks were different. Tracks in Figure 3. 11b were distributed without orientation, indicates irregular fretting. On the contrary, ordered wear track were observed in Figure 3. 11d, displays the heavy worn with counter-part. Considering the fixation screws were implanted in patient with 19 months, and the

exact broken time was unclear, as Figure 3. 11b shown, the screw possibly broke at early stage, and fretting at fracture surface in long term generates many different arranged tracks. However, Figure 3. 11d has shown a different fretting behavior, the ordered tracks indicates a heavy but possibly only one sliding was performed, that means the area was worn at initial fracture stage. As screw fracture happened, this area was performed relative motion under shear with counter-part, after motion the worn areas were no contact anymore.

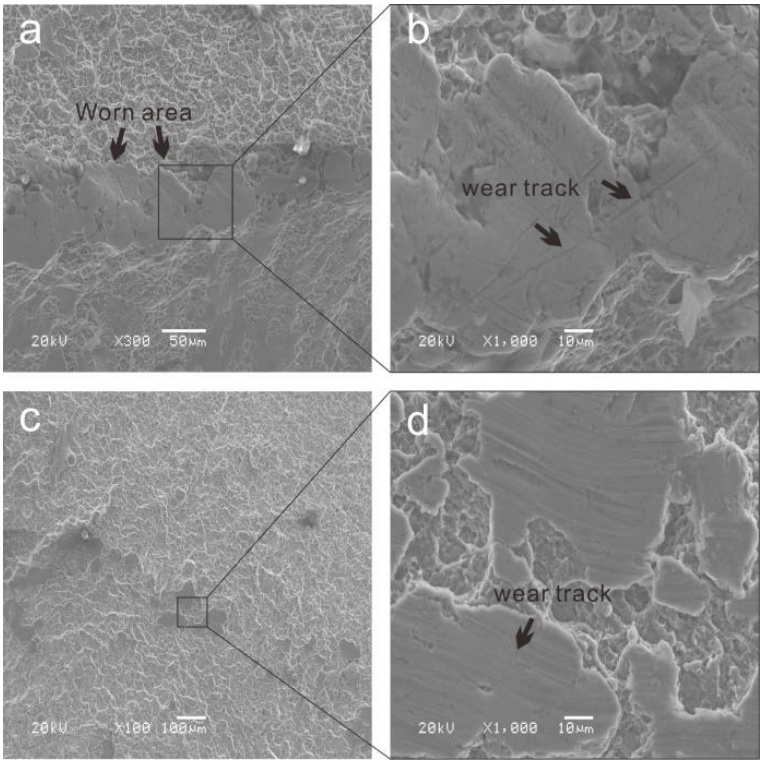

Figure 3. 11 SEM images of worn areas. Worn areas are widely distributed at fracture surface (a), the magnified image of disorder arranged wear tracks, and the longest track (black arrows), approx 100 μm (b). Worn areas in other locations (c), order arranged wear track (d)

Apart from the fracture surface, analysis investigation from fracture profile and adjacent area was also important to reveal the fracture process. An obvious

microcrack was detected along the thread root near fracture, prove a fatigue condition from the outer circumference of the screw as shown in Figure 3. 12 a and b. Root of thread are barely contact with bone, indicates the wear was not the factor formed crack. Meanwhile, near the fracture surface, tiny fatigue cracks were detected by SEM with higher magnification (see Figure 3. 12 c and d). The cracks were paralleled arranged, leads to the microcrack generation. A possibly mechanism is illustrated as follows, when the fatigue cracks generated and paralleled aligned, accumulated at thread root surface and formed microcrack, then the microcrack extended to screw substrate, leads to fatigue fracture.

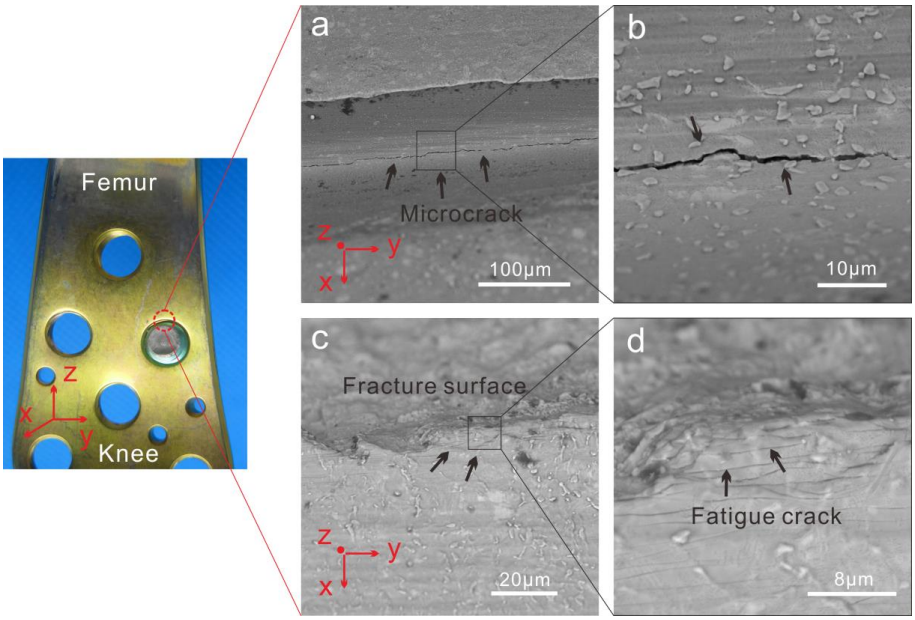

Figure 3. 12 Cracks were observed on the femur side of broken screw head. The crack generated and extent along with thread root (a), detailed image of crack (b), tiny fatigue cracks were arranged adjacent the fracture surface (c) and magnified image of fatigue crack (d)

Meanwhile, the FE analysis was applied to investigate the stress concentration, especially the stress distribution at the fracture interface area. Considering the patient

weight and femur stress condition, 800 N equivalent load was applied for the simulation. The entire model was meshed with a 20-node hexahedral element Solid186, while the mesh size was smaller at thread root than other parts. The Young's modulus applied was 113.8 GPa, Tensile Strength was 950 MPa and the Poisson's ratio was 0.342 for Ti_6Al_4V alloy.

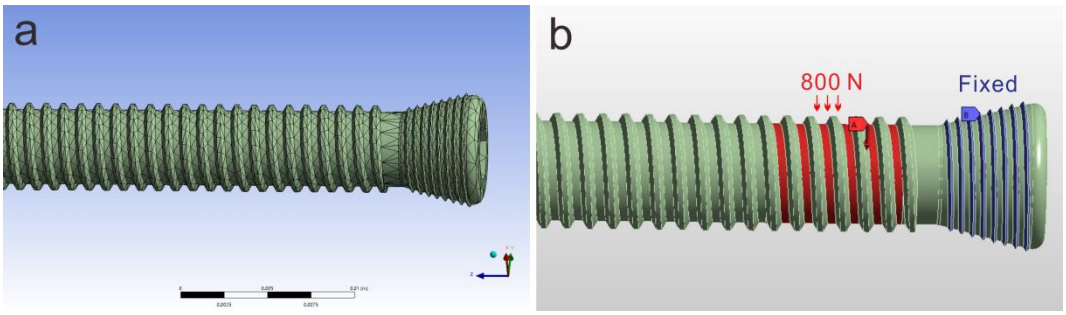

Figure 3. 13 Finite element analysis (FEA) model shows the mesh of screw (a), and conditions of FEA, 800 N equivalent force applied on the area close to plate and inside the bone. Fixed support was imposed on the surface of the screw head

Under preload, the stress distribution on the thread part was investigated. Through stress distribution, the stress was concentrated at the joint area of shaft and head. Simulation presence the maximum stress was 1141.5 MPa, at the both side areas of stress applied from top to bottom direction, see Figure 3. 14.

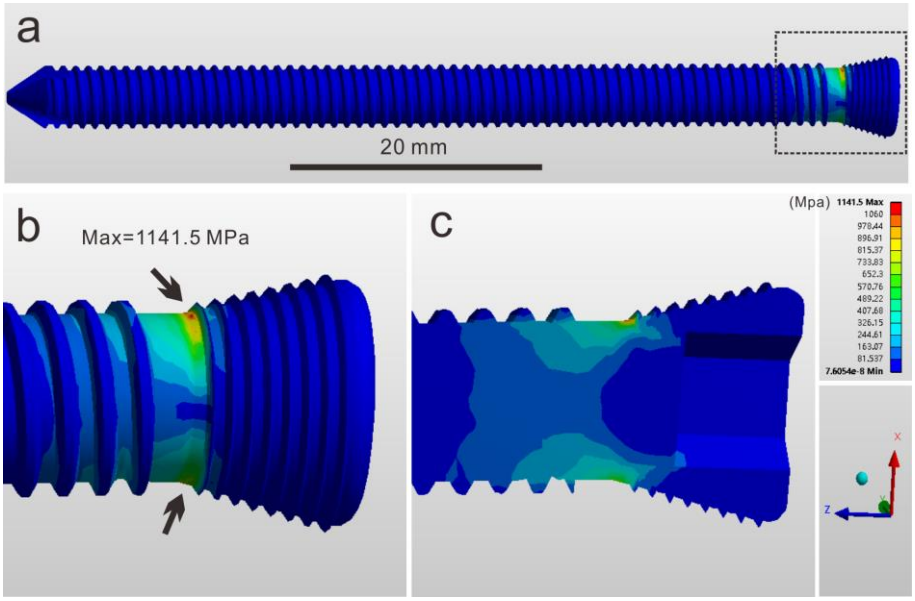

Figure 3. 14 FEA shows the stress distribution on the screw (a), the maximum value of stress exhibits 1141.5 MPa at thread root on bond area of head and screw (b) and section view of stress concentration (c)

Meanwhile, the simulated maximum deformation was about 0.01 mm. Apart from the simulation, the wear track was examined by SEM. Here, the longest wear track was measured, with 110 to 120 μm in length, the wear track featured with abrasive scar. The scale of wear track well proved the relative deformed at the joint area of shaft and head caused by fatigue, and the fatigue could be as the main cause for screw breakage. Besides this fatigue, corrosion also plays another important role during the failure procedure. Figure 3. 14 shows the cracks generated and arranged at the thread root, however, the distribution of tiny fragments lifted off from screw surface proved the contribution of corrosion to failure. Because of the stress concentrated at shaft head joint area, the cracks were extended faster. The initiation of corrosion can be due to the various conditions existing along the implant surface. However, as the fatigue crack exposed the screw substrate into the fluid environment which could

promote the fracture progress.

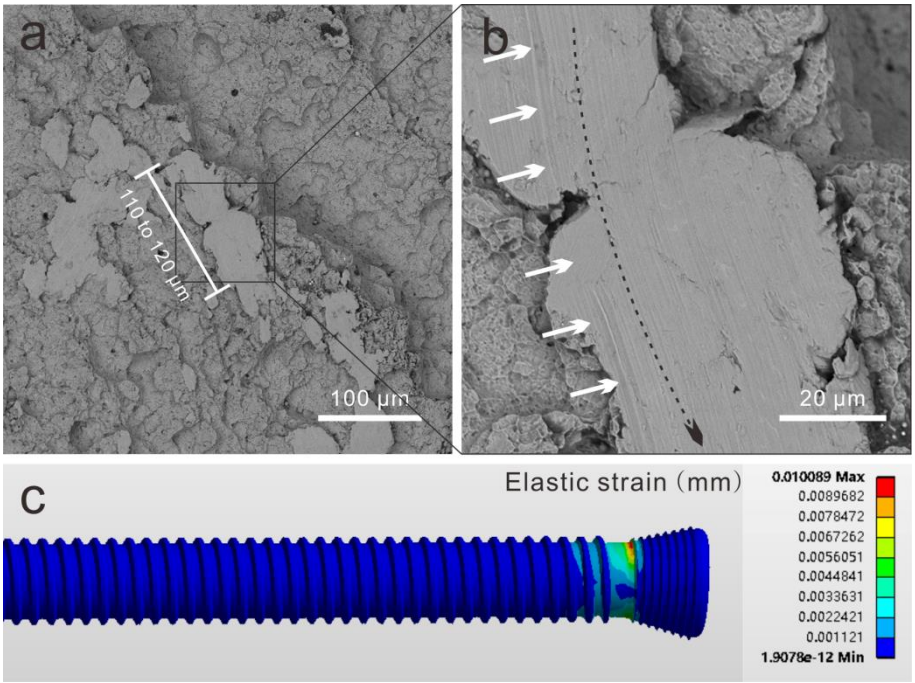

Figure 3. 15 Image of longest consecutive wear scar on the fracture surface with 110-120 µm in length (a), the magnified image of the wear scar (b) and FEA elastic strain with 0.01mm in maximum value of fracture surface

Corrosion also plays one dominate role in orthopaedic implants failure. Combined with other degradable failure, such as fretting corrosion and fatigue corrosion. Corrosion is the formation of electrochemical cells accompanied by active metal dissolution at favored localized spots at the implant body fluid interface. Thus, in this case, the body fluid can also react inside of implant though the cracks on screw surface.

3.4 Discussion

Titanium and its alloys are vastly used in orthopapedic applications due to a

combination of attractive properties such as high corrosion resistance, biocompatbility and mechanical properties. The corrosion resistance of Ti is result of spontaneous formation of a 3 to 10 nm passive titanium oxide (TiO_2) film on its surface when in contact with oxygen [154]. Under normal physiolocal conditions TiO_2 has the ability to reform. Abnormal cylcic loading, acidic enviroment, implant micromotion and their conjoin effects lead to permanent breakdown of oxide layer and active corrosion of the bare metal. Corrosion of the metal implants may jeopardize the integrity of the surrounding tissue and mechanical stability of the implant. When the metal ions are released from the implant surface or particulate metallic wear, they either remain in the intercellular spaces near the site where they were released or migrate systemically. The release of these ions activates the immune system and subsequent release of proinflammatory factors and chemical mediators which have shown to result in a cascade of events leading to periprosthetic osteolysis.

From these two retrieval cases, it is postulated that the failures were attributed to multiple factors such as fretting corrosion and fatigue corrosion, which correlated with the implants material biomechanical behaviors and biocorrosion resistance. For the titanium based implants, mostly Ti_6Al_4V with much higher Young's modulus (104—113 GPa) than that of natural bone (14.8—20.7 GPa) [155]. The unmatched modulus resulted in stress shielding leading to bone resorption, as well as poor mechanical instability due to micro-motion at the bone-implant interface. Furthermore, the biomechanics performance of implant is strongly depended on proper contacting between bone and implant, this requires sufficient tissue integrate to implant surface

that can fully presence the biomechanics performance of implant. This also pose an important requirement of implant surface–osteointegration. The poor osteointegration causes the failure of implant bone combination, this also could be the main reason for fretting and the formation of biofim at interface. Osteointegrated implantation also has decreased wear due to the limited relatively micro motion with bone tissue at interface. Secondly, it is a premise to be used for implant surface has to be with enhanced wear resistance and corrosion resistance. Inserted implants are facing a more strict environment with fretting combined with corrosion, these conditions require implants surface with more 'stable' mechanical and chemical performance. During operative progress can slight damage the implants surface, e.g. the plough damage and stress concerted on thread. This requires osteointegration capability of implants should be long lasting during and after the bone healing process, which is usually to be three months in proceeding. Even after bone healing, the surface is not expected to be lifted off from implant substrate, which can cause debris generation and release in tissue. Obviously, one main weakness of hydroxyapatite with plasma spraying is its weak adhesive strength with implant substrate that compromise its coating success in long term service. Another inevitable factor for engineering also needs to be considered, is the accessibility for manufacturing. Orthopaedic devices have many designing to fit its applications like stem, screw, cage, even skull, jaw and mesh. All of them have the osetointegration demand. Most of them are with curve or spheral surface, such as cages with three dimensional porous structure, this claims a flexible fabrication method can generate uniform and with same thickness on different locations of

implant. Due to the spraying technology is based on inducing external elements that spraying and coating on the implants surface, the topography of implants are quite limited, such as hip stem and bowl are fit well with its manufacturing. However, it is hardly to generate coating on the spine cages uniformly with the technology. Otherwise, the sprayed elements is not able to distribute inside the porous implants. Other issue for spraying technology is the adhesive strength with substrate, the bonding mechanism of coating and implants are based on simple mechanical bond, and because of the difference of elasticity modulus of coating and implants, the coating is prone to lift off while applying external stress.

3.5 Conclusion

In conclusion, case one reported failure of a femoral neck fixation using parallel cannulated screws. Inadequate fixation and micromotion appeared to cause fretting corrosion in these constructs and subsequently leading to the failure of the screws. Given the advantages of screw fixation for femoral neck fracture, studies are needed to develop titanium surfaces with enhanced fretting corrosion resistance and bio-functionality in order to establish the longevity of these screws. Case two highlighted a case of fatigue corrosion failure, as the insufficient bone integration to screw allowed the relative micromotion between screw and bone, combined with the repetitive stress applied by plate and corrosion atmosphere, resulted in the screw fracture.

All the retrieval failure cases highlighted the importance of bone-screw integration,

and the potential of implants surface modification to enhance osteointegratation, and wear and corrosion-resistance. However, apart from osteointegration, the wear and biocorrosion of the bone fixation device are not well studied and reported. These two performance are basis and strongly affects the success of implants.

Chapter 4

4. Fabrication of TiO_2 nanotubes and interfacial engineered TiO_2 nanotubes

This chapter will discuss the TiO_2 nanotubes fabrication on both titanium and medical grade titanium alloy (Ti_6Al_4V) substrates. NT and SO-NT were successfully grown on both titanium sheet and titanium foil, as well as on bone screws. The surface topography, chemical composition, crystallinity and mechanical properties of resultant surfaces were investigated and the results were discussed in this Chapter. The interfacial bonding of the TiO_2 nanotube bottom to the Titanium substrate was engineered to obtain the structure optimised TiO_2 nanotubes (SO-NT, the combination of conversional TiO_2 nanotubes and bonding layer). The examinations have demonstrated that the SO-NT has an interfacial bonding layer of approximately 120–150 nm that strongly joined the TiO_2 nanotube layer with the underlying Titanium substrate. The impacting, bending, and biotribological tests have demonstrated the SO-NT exhibited improved mechanical stability compared to that of conversional TiO_2 nanotubes (NT). The uniform hyper—fine interfacial bonding layer with nano-sized grains exhibited a strong bonding to nanotubes layer and Ti substrate. It concluded that the SO-NT has great potential to be exploited in the field of orthopaedic medical devices.

4.1 Introduction

The highly demand of improved osteointegration and enhanced biotribological and biocorrosion performance of implant surface, NT attracted much attention due to its potential application in orthopaedic. As the methodology illustrated in Chapter two, the NT and SO-NT were fabricated and systematically characterized in this Chapter.

4.2 Materials and Methods

Conversional NT and SO-NT on both pure Ti sheet and Ti_6Al_4V substrates, as the methods illustrated in Chapter two. SEM-EDX, XRD, XPS were carried out to measure the topographies and chemical composition of specimens. The mechanical performance of Ti, NT and SO-NT were systematically evaluated by Vicker's hardness tester, Nano indentation, ultrasonic vibration, surface roughness tester, bending test and industrial coating adhesive tester. Meanwhile, the finite elements (FE) analysis was applied to simulate the mechanical behaviours of NT and SO-NT under stress. As methods described in Chapter two, the interfacial bonding layer at nanotubes bottom was optimized under different anodization parameters, the bonding layer structure was compared by optical and SEM.

4.3 Results

4.3.1 Structure observation

Conversional TiO_2 nanotubes (NT)

The structure of TiO_2 nanotubes (NT) was mainly characterized by SEM. The top view of NT exhibits a porous topography, as the diameter of the porous strongly depends on the voltage applied and water content in electrolyte during anodization. Figure 4. 1 shows SEM examination of nanotubes anodized under 60 V for 60 minutes. It was observed the obtained array of nanotubes have a diameter about 100 nm, with 25—35 nm wall thickness. Furthermore, the topography of NT displays highly ordering arrangement.

As Figure 4. 2 shown, the profile of NT on titanium substrate, the nanotubes are vertically arranged with open—top and half spherical closed bottom attached with titanium substrate (half spherical bottom see Figure 4. 3). The length of NT (also the thickness of NT layer) is related with the duration of anodization procedure, in Figure 4. 2 the duration process was 1 h, the length of nanotube has reached 4 μm. The bottom structure of NT exhibits a typical hexagon shaped hemisphere as shown in Figure 4. 3.

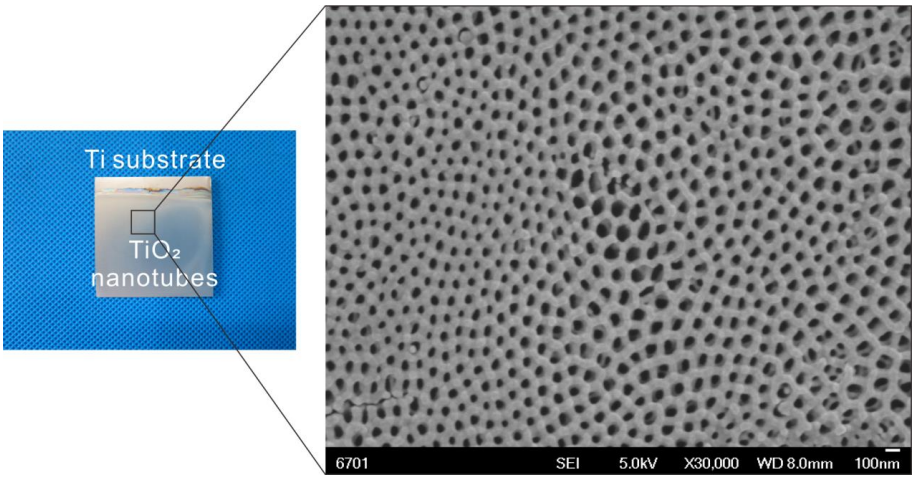

Figure 4. 1 The optical image of TiO_2 nanotubes (NT and SO-NT at 60V 60 min) and nanotubes structure top view

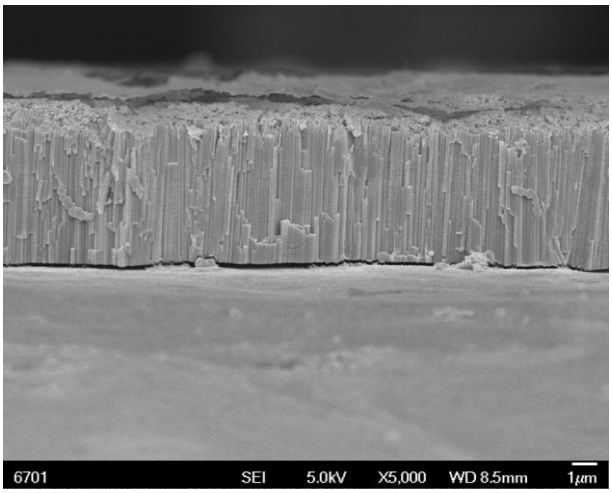

Figure 4. 2 TiO_2 nanotubes (NT) cross section view

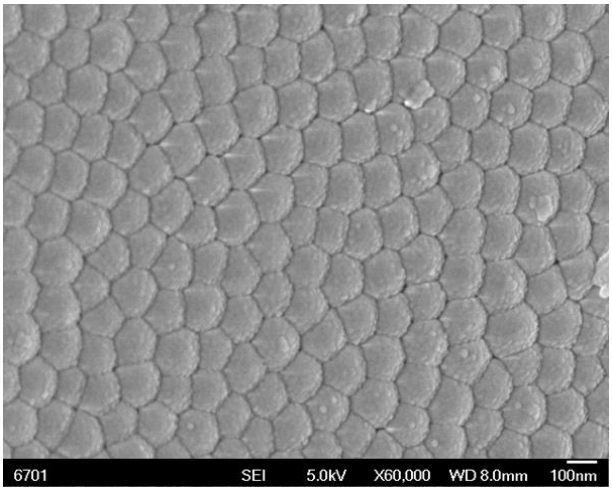

Figure 4. 3 TiO_2 nanotubes (NT) bottom view

Interfacial bonding layer

The interfacial bonding layer generated by anodization in this research is aim to improve the conversional NT bonding to the Ti substrate. Unlike the optical colour of NT which displays dark green, the bonding layer exhibits light blue or purple colour by naked eye. The different colour may indicates a different micro topography with nanotubes, see Figure 4. 4. Light reflection is a feasible method to detect nano structure change, the refection angle is influenced by the micro structure of material surface.

Figure 4. 4 Optical view of interfacial bonding layer

Figure 4. 5 has shown the micro topography of interfacial bonding layer which consisted with nano sized TiO_2 grains. And the arrangement of subunit grains could be disordered or ordered, the grain size can also change by shifting voltage applied. The parameter optimise of interfacial bonding layer will be discussed in detail at end of chapter.

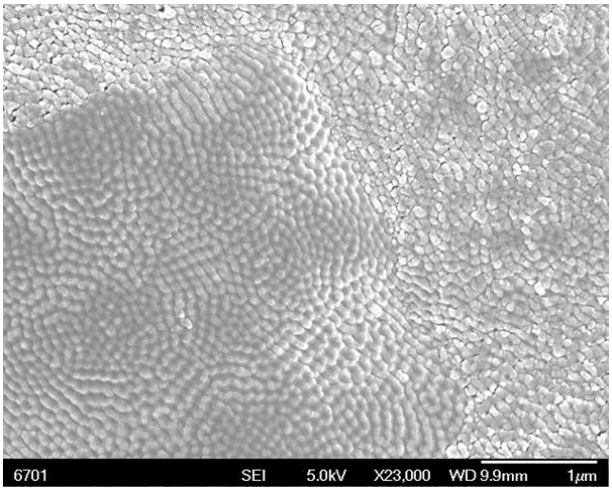

Figure 4. 5 Micro topography of interfacial bonding layer

Structure optimised TiO_2 nanotubes (SO-NT)

A structure optimised TiO_2 nanotubes (SO-NT) was fabricated by the inducement an interfacial bonding layer between nanotubes bottom and titanium substrate, see

Figure 4. 6 a and c. Compared with NT, the top of NT and SO-NT both display a porous structures with inner diameters of 100 nm were similar. A 120–150 nm thickness interfacial TiO_2 bonding layer was formed at the NT–Ti interface, Figure 4. 6 a. The interfacial layer was wrapped around the NT bottoms with no clear boundary between the interface of tube bottom and layer. Owing to the increased contact area of the tube bottoms, the interfacial layer distract shear forces and bore loadings. At the bottom of the NT and SO-NT, it can be noted that the SO-NT bottom was flat with tiny bulges, which were dissipated at the bottom outer-shells of the half-spherical NT. Regarding the NT, a typical tube bottom structure with hexagonal half - spheres and clear edges can be observed in each NT contact area.

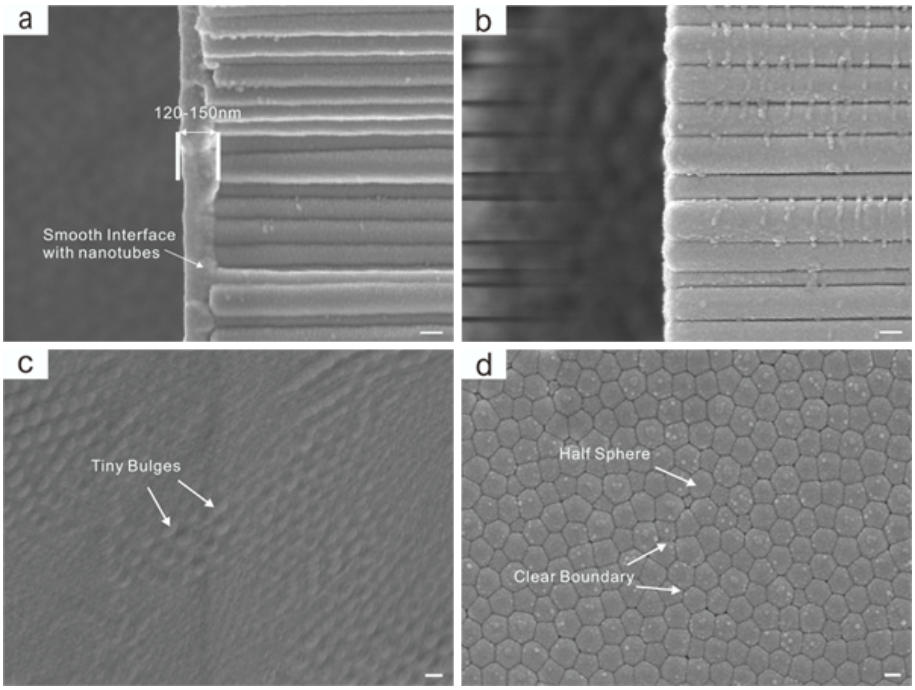

Figure 4. 6 TiO_2 nanotubes (NT) cross section view (a), structure optimised TiO_2 nanotubes (SO-NT) cross section view (b), NT bottom view (c) and SO-NT bottom view (d)

NT and SO-NT on Ti_6Al_4V medical grade alloy

As NT and SO-NT have been successful generated on pure titanium substrate (purity>99.6%), fabrication NT and SO-NT on medical grade Ti_6Al_4V was also investigated due to the widely usage in orthopaedic implants. Compared with the NT and SO-NT on pure titanium, micro pits were distributed on the nanotubes layer due to the rich vanadium and aluminum oxide film eroding during anodization, as reported by Patrick [82]. The micro pits affects the uniformity arrangement of both kinds of nanotubes. As the anodisation process in acid electrolyte, the dynamic in aluminum rich phase shows an eroding behavior while titanium rich phase growing nanotubes. The structural comparison between NT and SO-NT on titanium alloy are shown in Figure 4. 7 (NT: a1, a2 and a3, SO-NT: b1, b2 and b3). As can be observed, apart from micro pits, the shape of nanotubes has less similarity than nanotubes on pure Ti. Furthermore, the tube diameter of both NT and SO-NT were 100 nm in average, and the length (nanotubes thickness) were 2.5 ± 1 μm. The mainly difference is at the bottom of nanotubes layer, SO-NT bottom was with a 120–150 nm bond layer, instead, NT was exhibited a typical nanotubes bottom with half sphere globe. Indicates the interfacial bonding layer was also successful generated on Ti_6Al_4V.

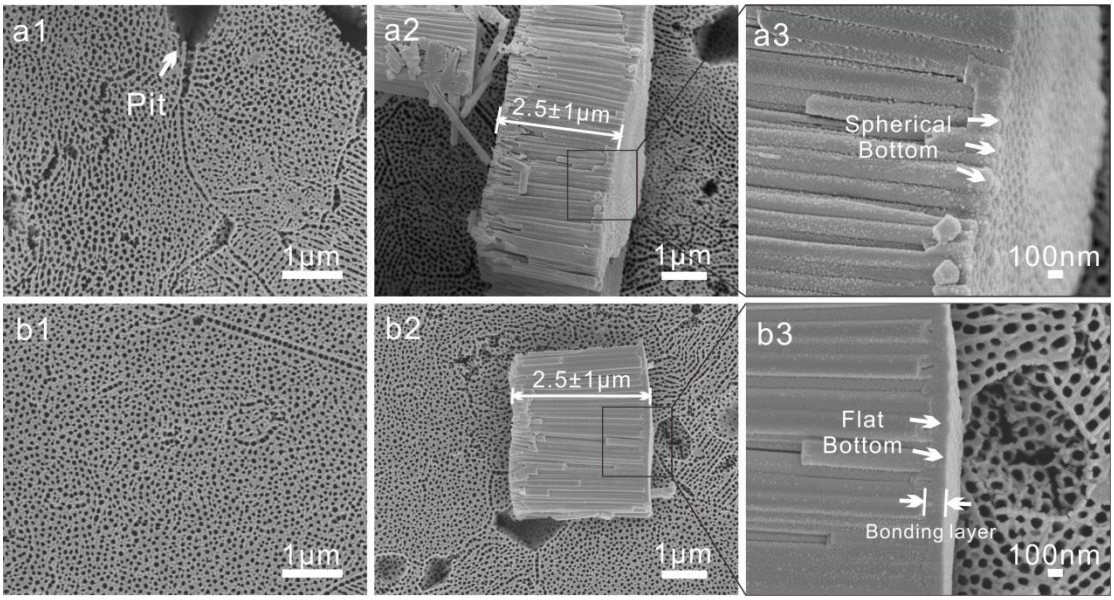

Figure 4. 7 FESEM images of top view of nanotubes, NT a1 and SO-NT b1, cross section view of NT a2 and SO-NT b2 and the profile bottom view NT a3 and SO-NT b3, Pristine machined surface, NT and SO-NT on Ti_6Al_4V orthopaedic screws

NT and SO-NT were fabricated on three medical grade screws (TC4). Figure 4. 8 reported the optical examination of the screws. It is observed from optical examination (Figure 4. 8), the NT and SO-NT exhibit dark green color. However, the SO-NT shows a slightly light green color than NT. Both NT and SO-NT surface screws are shown a homogeneous color without obvious (optical) pit defect.

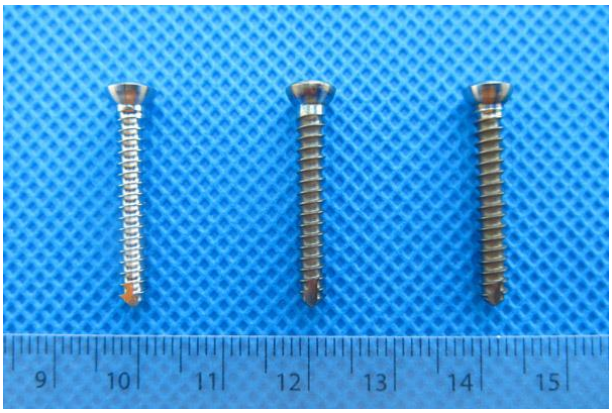

Figure 4. 8 Optical images of Pristine machined surface screw (left), NT surface screw (middle) and SO-NT surface (right) screw

Pristine machinery groove track was easily detected by FESEM, the surface of machined screw has a rough topography under the ten thousands magnification. Instead, NT and SO-NT were observed top porous vertically arranged with nanotubes structure, as shown in Figure 4. 9 and 4. 10. The successful growth NT and SO-NT on medical grade screws indicates that anodization method could be applied on complex shape and geometry of titanium based alloy, and the topography of nanotubes is similar to that of nanotubes on flat substrate.

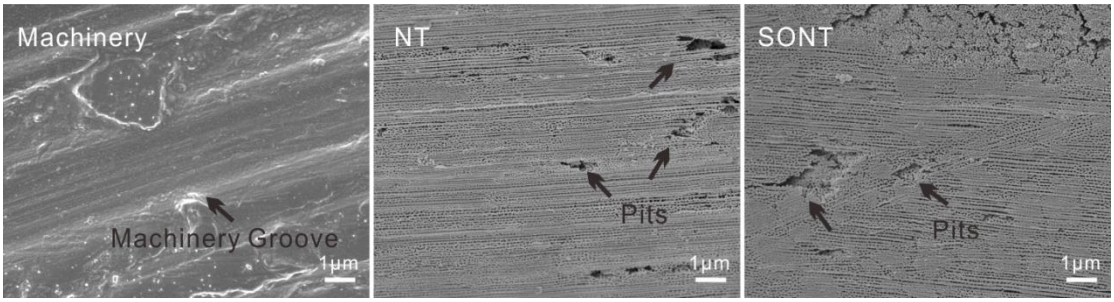

Figure 4. 9 FESEM images for machined surface screw, NT surface screw and SO-NT surface screw

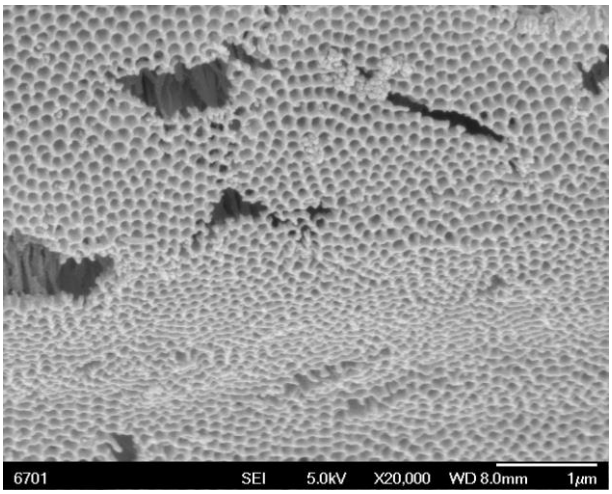

Figure 4. 10 The vertical arrangement of nanotubes (NT) on TC4 screws

4.3.2 Ti-O phase analysis (XRD)

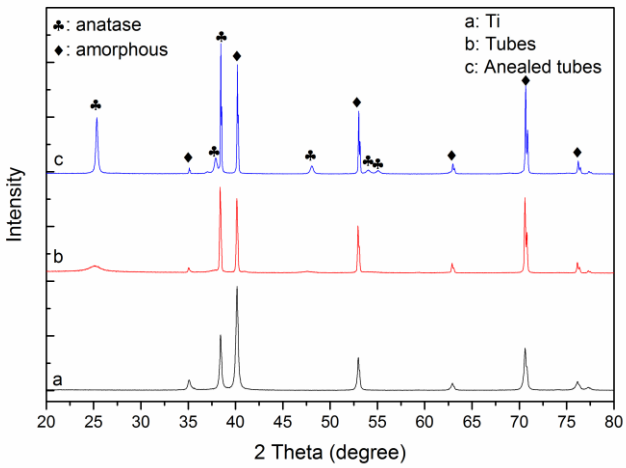

Figure 4. 11 XRD analysis of bare Titanium (a), TiO_2 nanotubes (NT and SO-NT) (b) and annealed TiO_2 nanotubes (NT and SO-NT) (c)

The titanium, NT and SO-NT specimens were examined by XRD. Although three specimens are titanium based, and covered by titanium dioxide layer, however, the Ti-O phase may different. Firstly, the Ti-O phase contains amorphous, anatase and rutile, among of them, rutile is widely existed in natural, however, generate rutile TiO_2 requires high temperature. The amorphous TiO_2 can shift to anatase by heat treatment. Figure 4. 11 illustrates the titanium presence a composite of amorphous and anatase TiO_2, only one anatase peak was presence indicates the composite of specimen was dominated by amorphous.

As the generated TiO_2 nanotubes (both NT and SO-NT) consisted with amorphous TiO_2 phase, the heat treatment process could transfer the phase from amorphous to anatase. Figure 4. 11 shows the XRD phase characters, as the heat treatment improves the signal for anatase peak of nanotubes (37–40 theta degree). Meanwhile,

the peak of amorphous has deceased after heat treatment. Anatase is always found as small, isolated and sharply developed crystals, and like rutile, a more commonly occurring modification of titanium dioxide, it crystallizes in the tetragonal system. However, the topography of annealed TiO_2 nanotubes was cracked, see Figure 4. 12. The stress may concentrate between nanotubes caused by the heat, and led to cracks. Although anatase phase is more stable than amorphous, the crack areas are prone to stress concentrated while shear loading applied on nanotubes surface.

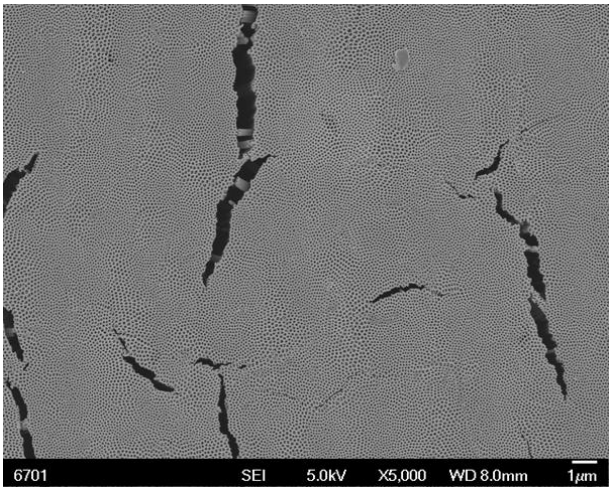

Figure 4. 12 SEM image of annealed TiO_2 nanotubes indicated micro cracks formation as a results of heat treatment with 4 °C/min to 500 °C

4.3.3 Chemical composition

Although the NT and SO-NT both exhibit similar nanotubes topography, the chemical composition of elements are different. The chemical compositions of the NT and SO-NT on bare titanium samples were measured via XPS with a survey scan and high-resolution element spectra for phosphorus and fluorine (Figure 4. 13). The existence of hydroxyl chemical group has been confirmed by high resolution scan of

O1s combined with two peaks, Ti-O (530.2eV, 70.58%Area) complex oxide and O-H hydrate (the hydroxyl 531.6eV, 29.42%Area) which plays key role for the hydrophilic performance and to bond chemical group with covalent bond. The XPS full-spectrum and high-resolution scan of SO-NT indicates a phosphorous 134eV peak (P2p). Table 4. 1 displays the semi-quantitative elements composition of NT and SO-NT, regards the quantity of titanium (NT=15.1, SO-NT=14.68) the fluorine and phosphorus containing of NT and SO-NT exhibit significantly difference. F1s/Ti2p (NT)=0.158, F1s/Ti2p (SO-NT)=0.062, P2p/Ti2p (NT)=0.073, P2p/Ti2p (SO-NT)=0.316 . Compared with NT, SO-NT presence a lower composite if fluoride, a higher composition of oxygen and a high phosphorous.

Table 4. 1 Elements composition of NT and SO-NT (Atomic, %)

	C1s	**F1s**	**O1s**	**P2p**	**Ti2p**
NT	42.76	2.38	38.66	1.11	15.1
SO-NT	33.45	0.91	46.32	4.64	14.68

Studies on phosphorous-incorporated Ti surfaces have demonstrated an enhanced osteoblast attachment, osteoblast gene expression, and removal torque forces. According to studies, the intensity of fluorine (F1s) was significantly lower after an additional anodization. Further, it is also established that a fluorosis can increase the bone fracture risk. The here presented SO-NT sample exhibited an extreme rare fluoride concentration and displayed existence of phosphorous: an evident existence of phosphorous in an elemental composition similar to the mineral phase of natural bone tissue was observed.

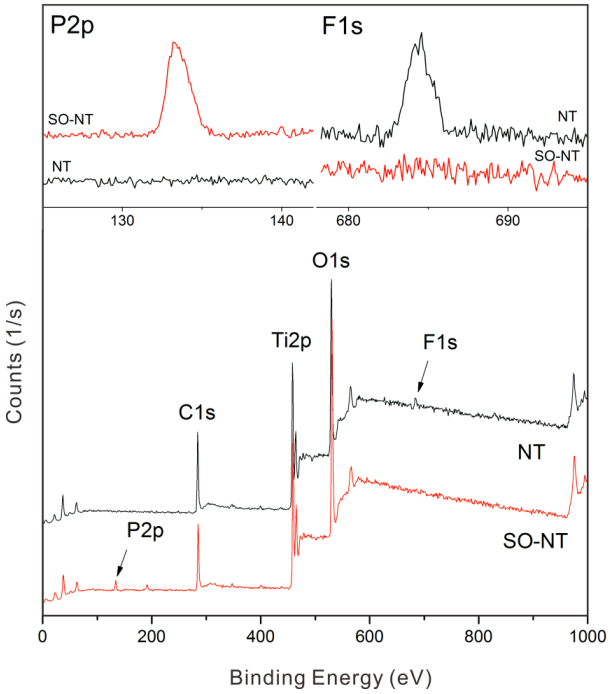

Figure 4. 13 XPS spectra of NT and SO-NT samples and corresponding high-resolution scan peaks of F1s and P2p

Apart from the whole spectrum of XPS, the high resolution scan of oxygen was also carried out to evaluate the Ti-O and O-H, as illustrated in Figure 4. 14, the oxygen peak was combined by Ti-O and O-H peaks, indicates the presence of hydroxyl on nanotubes.

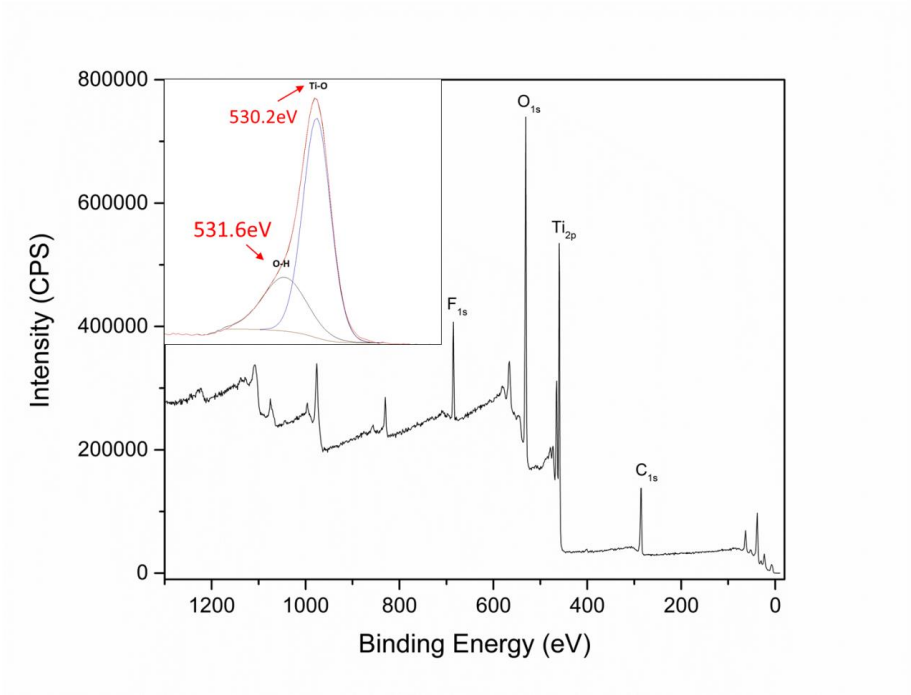

Figure 4. 14 XPS spectra of NT sample high-resolution scan peaks of Ti-O and O-H

Figure 4. 15 and Figure 4. 16 shows the EDX results by atomic percentage of nanotubes area and pits area on NT and SO-NT. On nanotubes areas, both NT and SO-NT consist above 55% of oxygen, 23-25% of titanium, 10% fluorine, 7-8% carbon and less than 3% vanadium. However, the chemical composition in pits area shows a significant difference. NT pits contains 54% titanium, 21% fluorine, 17% carbon, 5% aluminum and 3% vanadium. The chemical composition of SO-NT pits areas contains same value of oxygen, titanium, fluorine compares with nanotubes areas. In summary, the chemical composition of SO-NT displays constant regardless the topography change, however, NT shows the difference composition depends on surface topography.

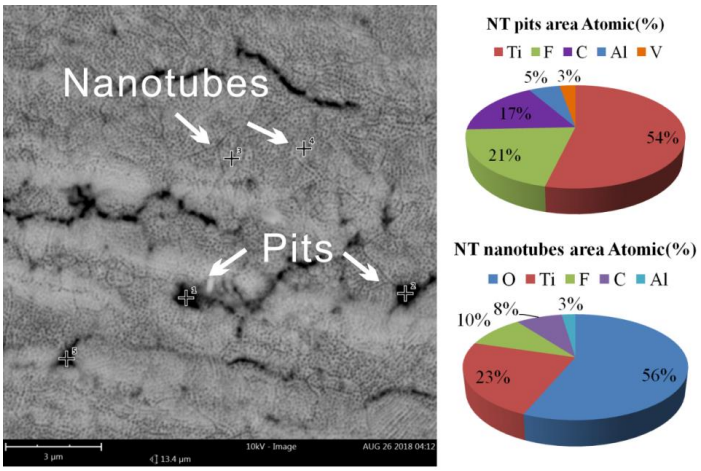

Figure 4. 15 The arrangement of NT on TC4 screw and the micro pits distribution, and the chemical composition on nanotubes areas and pits areas

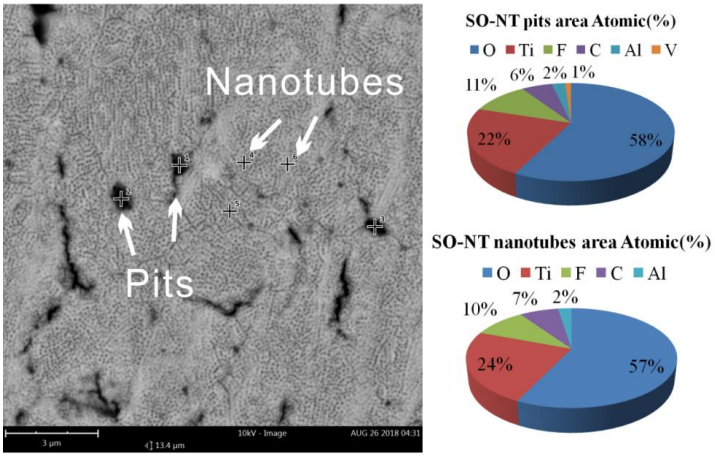

Figure 4. 16 The arrangement of SO-NT on TC4 screw and the micro pits distribution, and the chemical composition on nanotubes areas and pits areas

4.3.4 Mechanical properties

Vicker's hardness

The calculation method of Vicker's hardness has described in Chapter two, the Vicker's hardness of titanium and TiO_2 nanotubes are shown in Figure 4. 17. According the results, TiO_2 nanotubes surface is more 'soft' than pristine titanium

surface due to the micro topography.

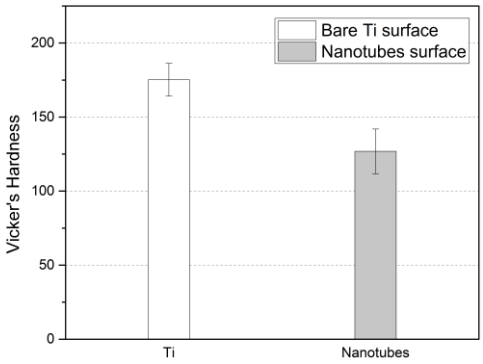

Figure 4. 17 Vicker's hardness of titanium and nanotubes

Nanoidentation

Apart from the macro Vicker's hardness comparison between titanium substrate and bare titanium surface. In nano materials science, the nano modulus properties are important affects the mechanical behaviors in nanoscale. Thus, the elastic modulus of NT and SO-NT were further investigated by nanoidentation. With the method described in Chapter two, the nanoidentation test of elastic modulus also proved that the nanotubes on NT samples is with no significantly difference with nanotubes on SO-NT. Figure 4. 18 shows both NT and SO-NT exhibits around 3 GPa of *E* modulus. Indicates the inducement of bonding layer has not change the micro mechanical properties of nanotubes.

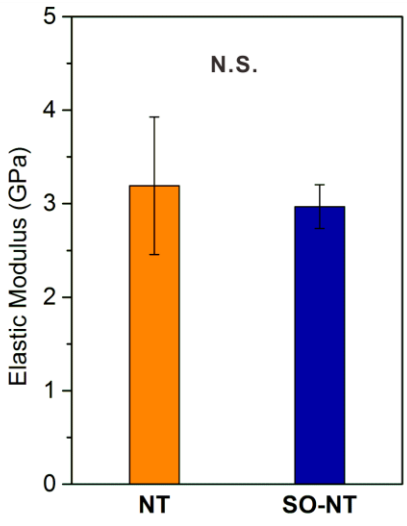

Figure 4. 18 Elastic modulus of NT and SO-NT were measured by nanoindentation with Berkovich indenter at less than 300 nm indentation (less 10% of nanotubes layer thickness)

Surface roughness

In general, friction is strongly relevant with surface topography, engineering surfaces never have an ideal geometrical shape, instead include different deviations. Roughness is the micro geometrical deviations. As two counterpart surface contacted, a region of plastic deformation with high contact pressure generate shear force lead to the deformation and wear debris peels off from the interface, asperity surface is easier deformed than smooth one. As the Figure 4. 19 shown the roughness of nanotubes is three folds (around 900 nm) than titanium surface roughness (around 300 nm).

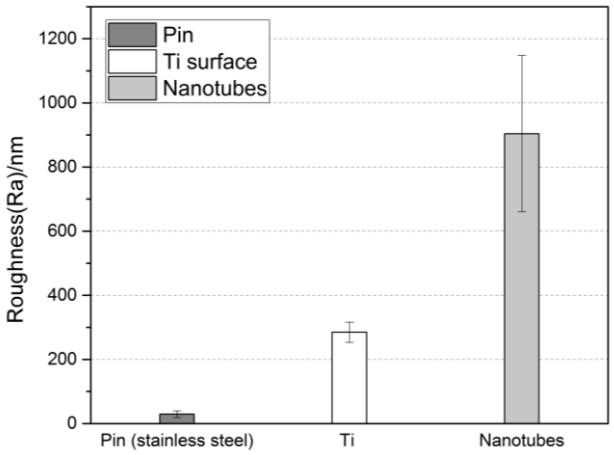

Figure 4. 19 Roughness of Pin (counter-part in biotribological test), titanium surface and nanotubes surface

The profile meter displays nanotubes surface is with more peaks and more pores than bare titanium surface, see Figure 4. 20.

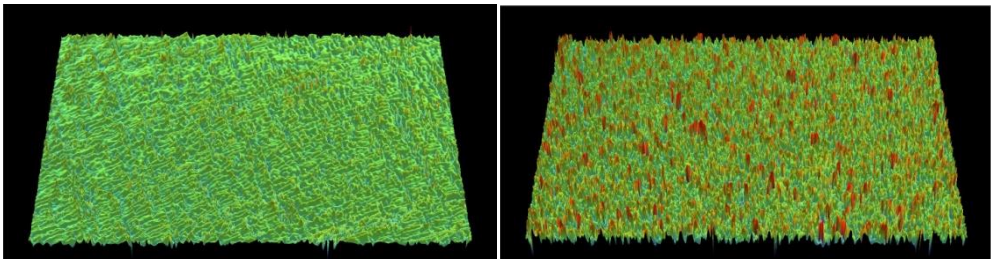

Figure 4. 20 3D topography comparison of bare titanium surface and nanotubes surface

Bending, Twisting test and Industry shock test

The systematically mechanical such as shocking, twisting and bending comparison of NT and SO-NT see Figure 4. 21. For comparison purposes, one half of the titanium plate was treated with common NT, whereas the rest was treated with a multi-step oxidation to obtain SO-NT. The differently coloured regions can be clearly distinguished in Figure 4. 21 a1. Owing to mechanical bending, one side of the Ti foil experienced strong tension (Figure 4. 21 a2), whereas the other side experienced

strong compression (Figure 4. 21 a4). Regarding the side under tension, the NT layer was completely peeled off of the Ti substrate, whereas no obvious damages in the SO-NT part could be observed (Figure 4. 21 a1). Regarding the side under compression, the NT part exhibited a peeled debris, whereas no damages were found in the SO-NT part (Figure 4. 21 a3). Furthermore, a twisting test was performed to evaluate the adhesion strength of the NT layer on the Ti substrate. After several twists (Figure 4. 21 b2), the NT layer of the NT part completely peeled off, whereas the SO-NT layer remained intact (Figure 4. 21 b3). Next, a shocking test was conducted to prove the improved mechanical stability of SO-NT (Figure 4. 21 c2): The NT layer of the NT part completely peeled off of the substrate, whereas the NT layer of the SO-NT part remained adhered to the substrate (Figure 4. 21 c3). Further, HR-SEM was employed to investigate the surface morphology after hitting. As shown in Figures 4. 21 c3-1–c3-3, no NT layer was left in the NT–Ti part, whereas it remained intact in the SO-NT part but was covered by many fragments, and the NT topography could still be detected in SO-NT areas. Subsequently, the falling-ball shocking experiment was performed on the NT and SO-NT samples, respectively. Heavy damages on the NT sample due to stripped NT could be observed (Figure 4. 21 d2). By contrast, approximately no damages were observed on the SO-NT surface, indicating a strong bonding between NT layer and Ti substrate (Figure 4. 21 d3).

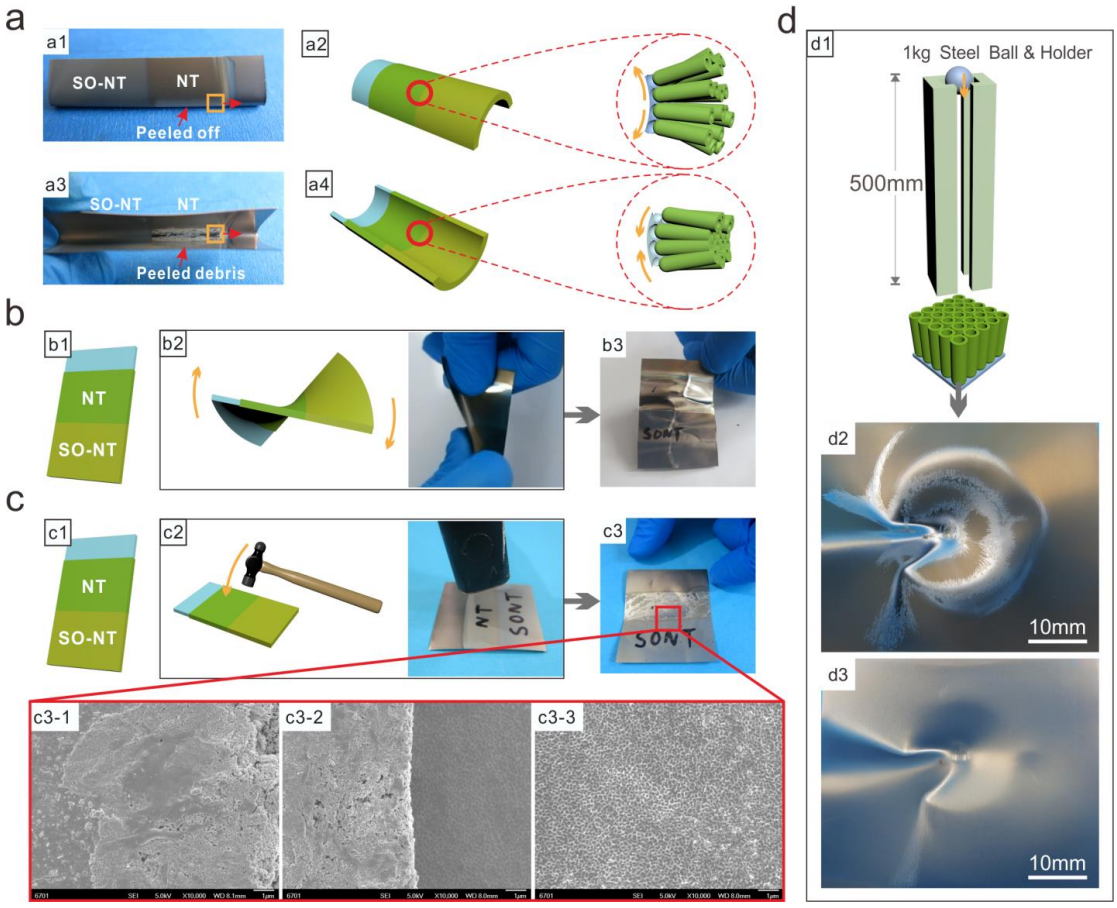

Figure 4. 21 Evaluation of mechanical stability of NT and SO-NT on one Ti foil: (a) Bending, (b) twisting, and (c) shocking tests on SO-NT and NT regions of one Ti sample. (d) free falling ball impact test: 1 kg steel ball free fall on to the specimen from a height of 50 cm. Part of nanotubes were debonded from the NT Ti substrate as a result of impact, nanotubes on SO-NT were remained on Ti substrate

Ultrasonic vibration

A mechanical ultrasonic vibration test was carried out to evaluate the mechanical stability of both specimens. The physical examinations of the specimens after the test are shown in Figure 4. 22. It was observed that the NT layer tended to deboned from the Ti substrate with the ultrasonic treatment. The longer the treatment, the more NT be deboned from the substrate. The NT layer was almost completely be removed after 180s ultrasonic treatment. By contrast, almost no damages was observed on the

SO-NT modified specimen. The SO-NT layer has no obvious damage even subjected to 300 second ultrasonic treatment. This result indicated that the as-prepared SO-NT sample are mechanically more stable than that of traditional NT samples.

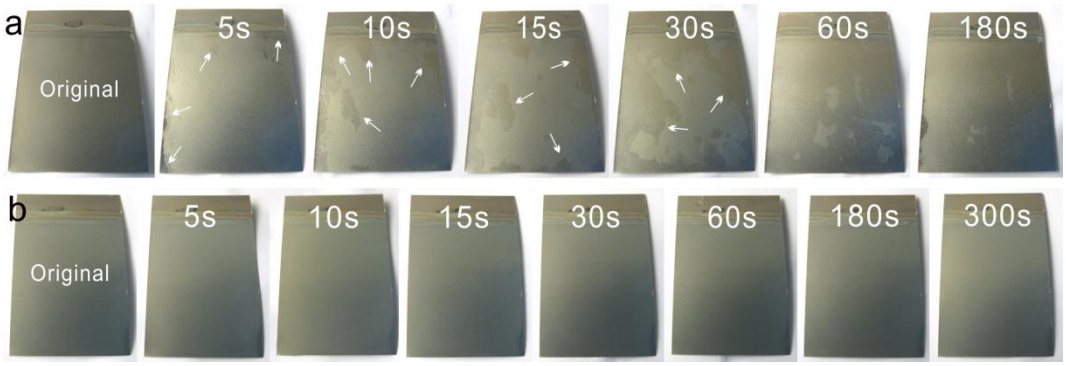

Figure 4. 22 Optical photos of NT (a) and SO-NT (b) in ultrasonic test. The ultrasonic test was performed in an ultrasonic cleaner in DI water under frequency=50 kHz vibration

Nanotubes layer pull-off test

An industrial coating adhesive test was carried out to measure the NT and SO-NT adhesive strength to the substrate. The pull off strength are shown in Figure 4. 23 and Figure 4. 24.

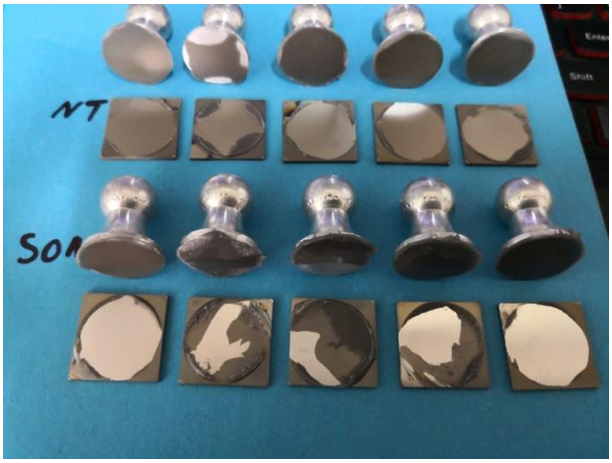

Figure 4. 23 Optical image of pull-off test for NT and SO-NT modified Titanium

It was observed that the pull off strength of SO-NT (2.6 MPa) is higher than that of NT which has a strength of 1.4 MPa. It was also observed from the optical image that the

peel off areas on SO-NT samples are smaller than that of NT lift areas, as shown in Figure 4. 23 (three samples in middle). Indicated the adhesive value of SO-NT might be higher than 2.6 MPa.

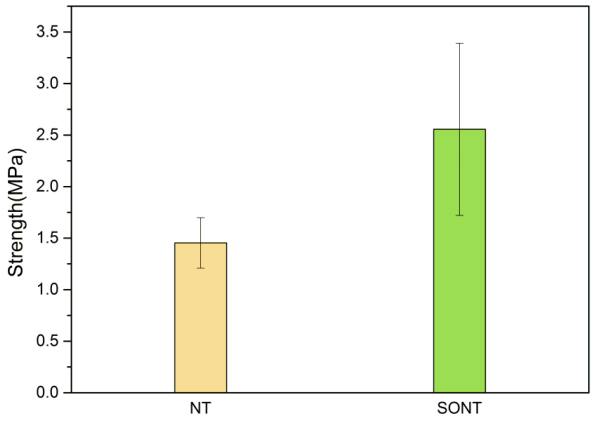

Figure 4. 24 Pull-off strength of NT and SO-NT modified titanium

The strong adhesion of nanotubes of SO-NT on Ti substrate is featured with an improved biomechanical stability which is important to orthopaedic implants success at bone implant interface.

Microscopic finite-element analysis (FE)

From the mechanical stability tests, the SO-NT displayed improved performance than NT layer. However, the mechanical properties of nanotubes on SO-NT were similar to that on NT modified specimens. It is postulated that the mechanical stability enhancement was contributed to the inducement of bonding layer. To further understand the function of bonding layer, the FE simulation was carried out to analysis the mechanism. As shown in Figure 4. 25, the maximal deformations of NT and SO-NT were 0.029 μm and 0.009 μm under unit bending loads, respectively; These equivalent to the maximal stresses of 108 MPa and 63 MPa, respectively.

Compared with NT, the maximal deformation of SO-NT was 69% less and the maximal equivalent stress was 42% less.

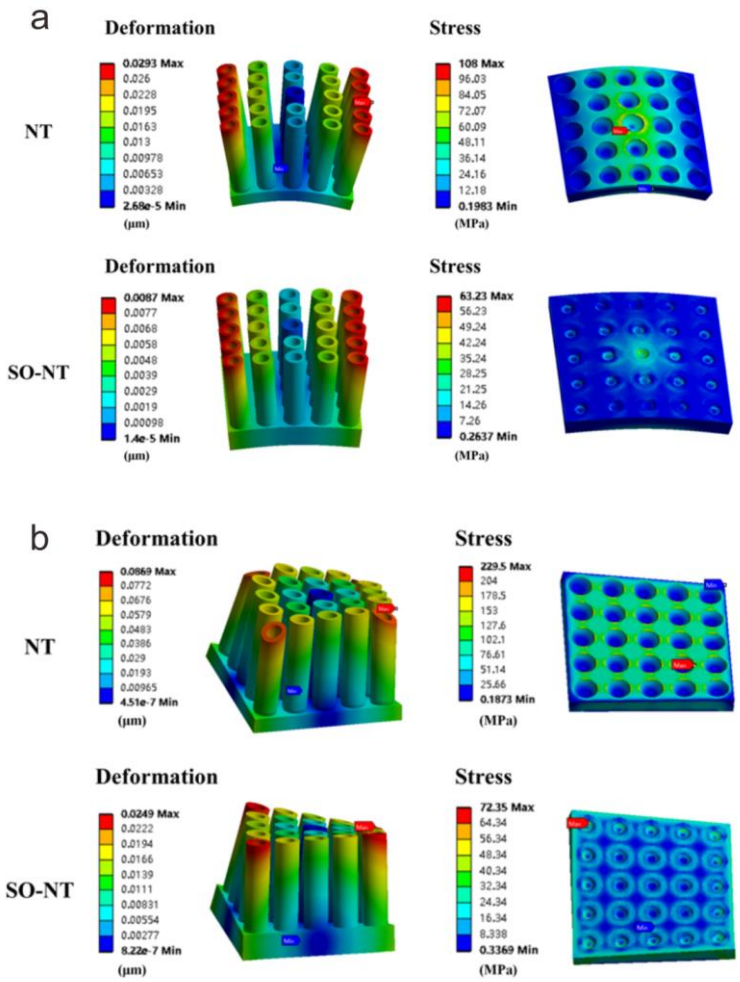

Figure 4. 25 Deformation and stress results of FE simulations for (a) unit bending and (b) twisting load

The maximal deformations of NT and SO-NT under unit twisting loads were 0.087 μm and 0.025 μm, respectively; The maximal equivalent stresses were 230 MPa and 72 MPa, respectively (Figure 4. 25b). Compared with NT, the maximal deformation of SO-NT was decreased by 71.26 % and the maximal equivalent stress was decreased by 68.70 %. The results also shown that the stress concentration of SO-NT was evidently reduced. Because of the nanotubes on NT and SO-NT have the similar for

mechanical properties, it is reasonably presumed the enhancement of stiffness and strength were attributed to the presence of the interfacial bonding layer.

4.3.5 Bonding layer optimization

The bonding layer plays important role in mechanical performance of SO-NT, the optimizing the processing parameter of bonding layer is necessary. As reported in Chapter two, the bonding layer structure was affected by parameters such as voltage, duration. Thus, the table 4. 2 summarized the observation during experiments. It was reported that the anodisation parameters influence the bonding layer from the optical color. Optical is a facile and priority method to detect the surface layer uniformity.

Table 4. 2 Parameters and erodes of bonding layer (H_3PO_4)

	Voltage(V)	Duration(min)	Colour	Erodes
a	200	30	green(irregular)	large & massive pits
b	150	60	dark brown	obvious pits
c	150	10	gold(irregular)	obvious pits
d	130	10	light gold	obvious pits
e	120	10	light gold & blue	obvious pits
f	110	10	light gold & blue	non-obvious pits
g	105	60	dark green	few obvious pits
h	100	15	light gold & blue	few obvious pits
i	100	1	gold & purple	non-obvious pits
j	95	15	light gold & blue	non-obvious pits
k	90	5	blue	few obvious pits
l	85	5	blue	few obvious pits
m	80	15	light gold & light blue	few obvious pits
n	80	5	light blue	few obvious pits

The interfacial binding layer with parameters generated on titanium substrate are shown in Figure 4. 26. From the optical image Figure 4. 26, the interfacial bonding layer fabricated by high volts (up to 100 V) and long duration (up to 10 min) are featured with defects, marked with red arrow.

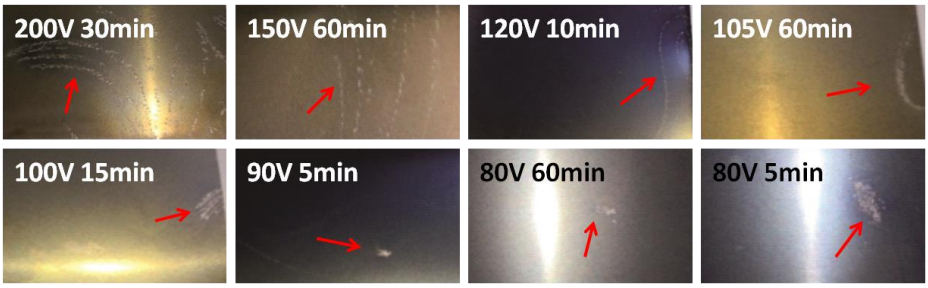

Figure 4. 26 Optical defects (pits) on specimens of interfacial bonding layers

The obvious defects strongly affect the material performance while implanted into body. Eliminate other parameters with observe optical defects, to compare the morphology of samples with 150 V–60 min, 105 V–60 min, 100 V–15 min, 100 V–1 min, 95 V–15 min, 80 V–15 min, 80 V–5 min by SEM, as shown in Figure 4. 27.

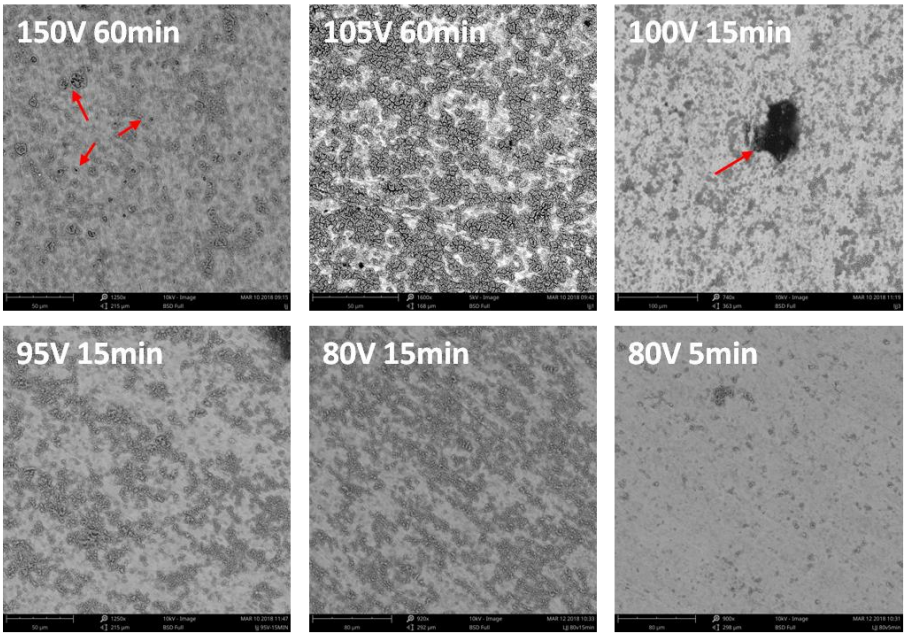

Figure 4. 27 SEM images for bonding layer specimens with different parameters shown in each figures

Bonding layer fabricated under 100 V for 1 min and 60 V for 3 min, both samples are not able to detected obvious defects by SEM. And the sample made by 100 V–1 min showing gold and purple color. From SEM image, the 100 V–1 min sample also observe smooth surface without any micro sized pits, as shown in Figure 4. 28.

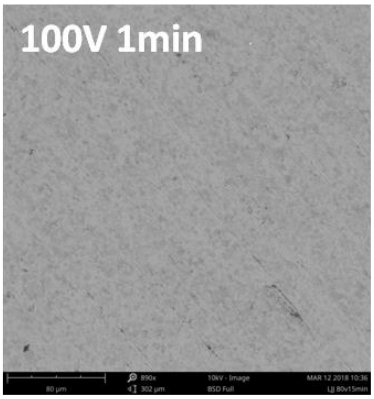

Figure 4. 28 SEM image for sample processed under parameter, 100 V for 1 min, this specimen was featured with smooth surface without obvious or micro sized pits under SEM

While applied voltage higher than the dielectric breakdown limit of the oxide, the oxide will no longer be resistive to prevent further current flow and oxide growth, which will lead to more sparking, known as Anodic spark deposition (ASD) or Micro arc oxidation (MAO). The applied voltage for interfacial bonding layer generation was below the break down volt in H_3PO_4 electrolyte.

The high resolution SEM shows the difference between these two strategy anodization, bonding layer generated by 60 V for 3 min shows a highly ordered structure with 100 nm in diameter for grain size, instead, bonding layer fabricated by 100 V for 1 min shows more irregularity with the array of grain, the distribution of massive grain are in different layers, higher voltage leads to many grain are assembling with adjacent grain, generating 300–500 nm sized grain-group. These irregular arranged grain can affects mechanical stability of wear interface while applying shear stress. Compared with 300–500 nm sized grain-group, the grain was around 100 nm in diameter for the bonding layer generated by 60 V with 5 min, and

more importantly, the arrangement of 100 nm grains were ordered.

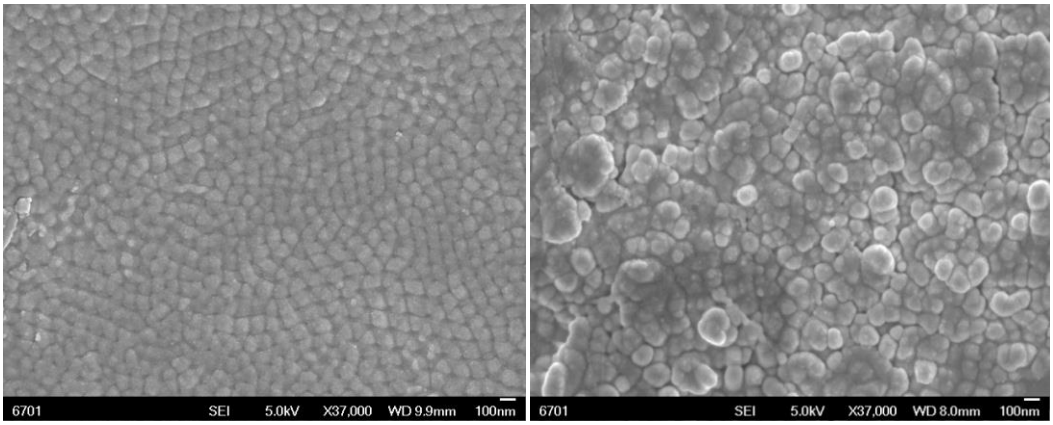

Figure 4. 29 FESEM images, 60V–3min (left) and 100V–1min (right)

Among the grain size, the other important parameter is the thickness of bonding layer as previous discussed (Figure 4. 29). The bonding layer thickness of 100 V was 150–180 nm which is 30 nm thicker than bonding layer generated by 60 V (120–150 nm). Indicates the grain growing rate of high voltages were faster than applied lower voltage. The maximum grain growing rate of 100 V is 180 nm/60 s=3 nm/s, while the maximum rate of 60 V is 150 nm/180 s=0.83 nm/s. Two possible speculations that observes a thick bonding layer in shorter duration, one possible route is faster growing rate generates the bonding layer with less compactness, the other possible phenomenon is fabricates larger grain during the anodization.

4.4 Discussion

As the nanotubes (both NT and SO-NT) were generated on the different shape titanium substrate successfully, such as titanium foil, titanium sheet and titanium alloy medical screws. Regardless the shape of titanium substrate, the arrangement of nanotubes were vertical arranged with the in-situ area. Indicates the nanotubes are

featured with consistent ordering, top toward bone tissue and bottom contact titanium implants. The consistent arrangement allows cells could only interact with nanotubes top area. Moreover, the generation methodology, anodization also greatly improves the potential application in orthopaedic and dental implants due to diverse designing of implants might restricted coating technology. Compared with HAp sprayed technology, the advantage of anodization is capable to fabricate nanotubes on various implants surfaces, such as screws thread, porous implants. Furthermore, the nanotubes can also fabricated on titanium based alloy, such as Ti_6Al_4V medical grade TC4.

The nanotubes growing on Ti_6Al_4V alloy in fluorine containing electrolyte was described by researchers. Due to the Ti_6Al_4V alloy where vanadium containing phase (also aluminum rich phase) enhanced etching in fluorine, leads to selective dissolution and an inhomogeneous pits formation. And for this etching attack supposedly due to the high solubility of vanadium oxides in the F-containing electrolyte [156]. The vanadium oxides forms pits are dissolving during the nanotubes growing process, leads to the alloy substrate exposed during and after anodization (Figure 4. 30). The EDX results of NT and SO-NT on pits areas have demostrated the difference chemical composition. It is remarkable that due to the substrate exposure in pits areas on NT, the areas are vulnerable under fluorine containing electrolyte. Metal ion released from substrate into solution, and the etching attack leads to pits corroded deeper and deeper. However, the induced bonding layer in SO-NT covers the pits areas, effectively protected the substrate from corrosion (will discuss in detail in

following chapters). SO-NT EDX results of pits areas exhibit highly similar chemical composition with that in nanotubes areas, due to the bonding layer presence.

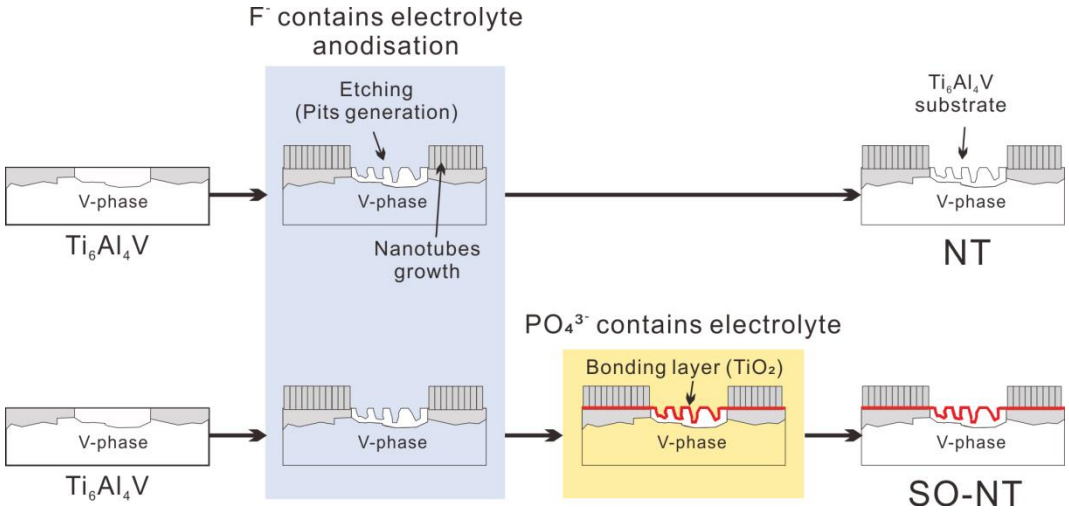

Figure 4. 30 The vertical arrangement of nanotubes (both NT and SO-NT) on TC4 screws and the corrosion etch mechanisms of NT and SO-NT

The physical and chemical properties of nanotubes have been systematically evaluated by SEM, 3D topography observation (roughness), XRD, XPS and Vicker's hardness. The XRD results show the nanotubes are mainly amorphous, and annealed nanotubes increased the component of anatase phase. However, the topography of nanotubes has cracking damaged after heat treatment. The chemical composition of NT contains titanium dioxide, and fluorine which might left during the anodisation process. Compared with NT, SO-NT contains with phosphorous and less fluorine presence. The phosphorous mineral deposition plays a key role in affects osteoblasts behavior and bone regeneration process [157].

Moreover, a novel SO-NT which consisted a hyperfine with 100 nm grains bonding layer at the bottom of nanotubes layer exhibits an improved mechanical stability than conversional NT. The enhanced mechanical properties has been evaluated by

shocking, bending, twisting and industry impact. The nanoidentation well proved that the increased mechanical stability of SO-NT was not enhanced by changing nanotubes layer, instead, the bonding layer plays a vital role for mechanical performance. The FE analysis indicates with the inducement of bonding layer, less stress concentrated at the nanotubes layer titanium substrate interface, leads to the mechanical stability improvement. To further understanding and optimise the bonding layer, both voltage and anodize duration have been comparable analyzed, as the higher voltage applied (100 V), the grain size has increased and the arrangement of grains has more trend to disordering arrangement. The different size of grain and disorder arrangement might leads to stress concentrated at areas under shear application. Above all parameters for interfacial bonding layer, the parameter of 60 V with 3 min exhibits the well arrangement and high similarity grain size.

4.5 Conclusions

In this chapter, although SO-NT exhibits an improved physiochemical and mechanical stabilities than NT, the clinical orthopaedic and dental devices are place a more harsh tribological requirements and complicated stress distribution on implants surface. The prolonged duration, above 20 years implantation in human body can pose a great challenge for of the implants surface coating. After surgery implantation and the establishment original mechanical contact of bone implant surface, the implants are subjected to relatively micro motion with bone while under loading. The micro-movements at bone implant interface and consequently to shear stresses at

that place. Furthermore, the micro movement behaves under the presence of a corrosive biological environment. Micromotion damage combines corrosion can cause biotribological and biocorrosion degradation, known as fretting corrosion. As a consequence, the deboned wear particles trapped at adjacent bone tissue induce adverse biological reactions and leads to loosening.

As reported in chapter three, regarding the three severe fretting corrosion failure screws, the further research of biotribology and biocorrosion of NT and SO-NT is fundamental and necessary. The systematical research of biotribology and biocorrosion evaluation of titanium (titanium based alloy), NT and SO-NT will be discussed in following chapters.

Chapter 5

5. Biotribology and biocorrosion of titanium, TiO_2 nanotubes and structure optimised TiO_2 nanotubes

This chapter investigated and analysed biotribological and biocorrosion behaviour of titanium (titanium based alloy), TiO_2 nanotubes (NT) and structure optimised TiO_2 nanotubes (SO-NT) surfaces on flat substrate and medical bone screws. The nanotubes de-bonding mechanisms were discussed, it was observed that SO-NT has demonstrated improved wear resistance and corrosion resistance than NT and titanium surface by systematically biotribological and biocorrosion tests. The presence of bonding layer on SO-NT has well solved the drawback of mechanical limitation of NT and has proven a further potential for clinical usage.

5. 1 Introduction

The biotribology and biocorrosion properties of implant surface materials strongly affects the performance of implants. Tribology behaviour is commonly presence in orthopaedic implants. Not only the heavy wear at articulating surface of artificial joint, the fretting corrosion at tapping area on hip replacement, but also the mild fretting at bone implant interface. The objectives of the biotribology and biocorrosion investigation of this Chapter is to evaluate wear resistance and nanotubes degradation mechanisms by pin on disk wear test, ball on disk and fretting with bone. And further investigate the biotribological performance of pristine Ti, NT and SO-NT engineered surfaces on bone screws under various conditions, such as interface fretting.

5. 2 Materials and Methods

As the methods illustrated in Chapter two, the biotribological test was mainly performed on pin-on-disk, two parts of pin-on-disk experiments were employed to evaluate the biotribology performance of titanium surface, TiO_2 nanotubes (NT) and structure optimised TiO_2 nanotubes (SO-NT). Testing materials were tested in pairs under non-abrasive conditions, pins in wear testing were manufactured with radius tip. The relative wear motion was located at the testing disk specimen center. Because of aim was to evaluate the biotribology performance of NT or/and SO-NT layer during wear process. Furthermore, the thickness of NT and SO-NT were 2~3 μm, indicates

that the heavy wear (titanium substrate abrasive loss) needs to avoid in the case. Due to that, the wear test cycles were set to 1.2×10000 mild wear. The test parameters are shown in Table 5. 1 as below.

Table 5. 1 Parameters of pin-on-disk comparison wear test for NT surface and Ti surface

Pin (R=60mm)	Lubricant	Contact stress (MPa)	Load (N)	Cycles (x1000)
316 stainless steel	25% diluted bovine calf serum	122.8	5.85	12

Frequency (Hz)=1, Sliding distance (mm)= 10

As the illustration in Chapter two, the volume loss of each specimen was estimated after the wear tests. Meanwhile, a fretting screw model was proposed to evaluate the pristine Ti, NT and SO-NT modified bone screws. Although the pin-on-disk and ball-on-disk tests can be systematically evaluate the biotribological behaviour, and the degradation mechanism was discovered by wear track analysis and friction coefficient analysis, the practical application may exhibits a more complicated tribology conditions, such as fretting. As the parameters were choose as below in Table 5. 2.

Table 5. 2 Parameters of fretting experiment model

Bone	Lubricant	Temperature (°C)	Load (N)	Cycles (x1000)
Sheep bone	none	37	100	36

Frequency (Hz)=10, Sliding distance(um)= 300

After the fretting test, the wear region was calculated. Herein, a method was applied to quantify and compare the debond off area of nanotubes film on NT and SO-NT screws. The SEM observation locations on self-tapping screw were shown in Figure 5. 1. Screw thread is concentrated with mass stress while operative insertion, and the

material on thread can be easily removal. To comparative analyze the wear with machined, NT and SO-NT surface on thread, locations at point 1, 2, 3, 4, 5 on thread were analyzed by SEM, the five areas were the areas passed by central line. Central line was defined by passing the drill tapping plane. Using the method, five certain areas on NT and SO-NT screws were selected, the debond off nanotubes areas proportion was measured by ImageJ software. The SEM view area was 1.01×10.1 mm^2, the debond off area (Figure 5. 1, Debond off area) were calculated. With the average debond off area value of the five observation points, a lift area on one circle of thread (φ) can be calculated by equation 1, basis on the hypothesis that the wear damage were equivalent of areas on thread. Nevertheless, the method above is inappropriate to calculate the debond off area of titanium alloy screw due to the damage areas were indeterminacy by SEM observation. Furthermore, the damaged areas on titanium alloy screw were with the identical chemical composition and no significant distinction of topography compared with screw before fretting. It is uncertain to define the worn area by SEM. Therefore, the fretting titanium screw was only been topography compared with NT and SO-NT screws.

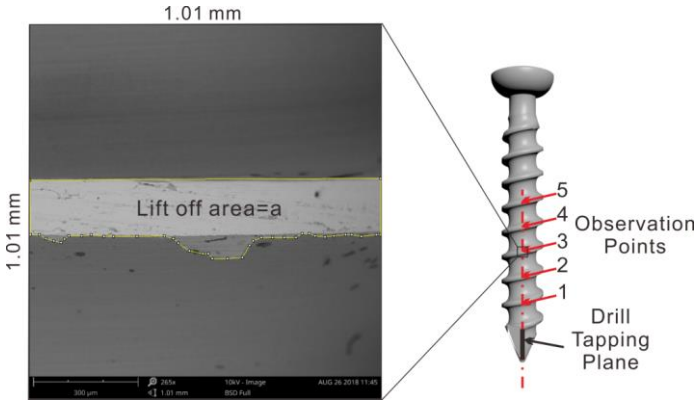

Figure 5. 1 Observation locations on screw surface

$$\varphi = \frac{\frac{(a_1+a_2+a_3+a_4+a_5)}{5}}{\frac{1.01}{2\pi r}}$$ Equation 5. 1

Where,

φ is the debond off area on one circle of thread, mm^3,

a is each observation points of actual nanotubes debond off area, mm^2,

π is constant 3.14,

r is the radius of thread of screw, is 1.75 mm.

Apart from fretting track measurement, the abrasion loss on thread could also be compared by measuring the width of thread after fretting test. Worn thread became thicker than pristine thread, and due to the wear, thread width was increased by worn degree. Fretting pristine machinery, NT and SO-NT thread width were measured and analyzed by SEM. Three locations width on the identical circle thread were measured by image J.

5. 3 Results

5. 3. 1 Wear study

Wear behaviour of Ti and NT surface

After pin on disk test with aforementioned parameters as reported in chapter two, the wear track profile on the disk and the wear scar profile of the pin were measured by a tester, TESA under ISO4287 to calculate the volume loss of each friction pair.

Figure 5. 2 shows the volume loss of the pristine titanium and NT modified titanium. It was observed that Ti substrate exhibited a wear volume of 0.32 mm^3, this is much

higher than that of NT which has a volume loss of 0.19 mm^3 under the same test condition. Furthermore, the volume loss value of countering Pin exhibits similar trend, volume loss of Pin (Ti) reaches 0.049 mm^3, which is 3.7 times higher than Pin (NT), with 0.013 mm^3 value. From the calculation results of volume loss of pin and disk, it is obvious the NT layer has contributed to the improvement in wear resistance, as confirmed in the test (1.2 × 10000 cycles friction). From the wear scar quantify analysis, the improved wear resistance of NT surface effectively played as a protection layer for the substrate, physical isolated the shear on implant surface. Furthermore, the presence of nanotubes layer reduced the wear particle formation.

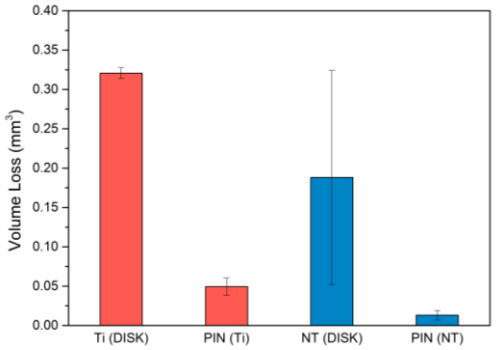

Figure 5. 2 Volume loss of pristine Ti and NT modified titanium disk and pin, respectively

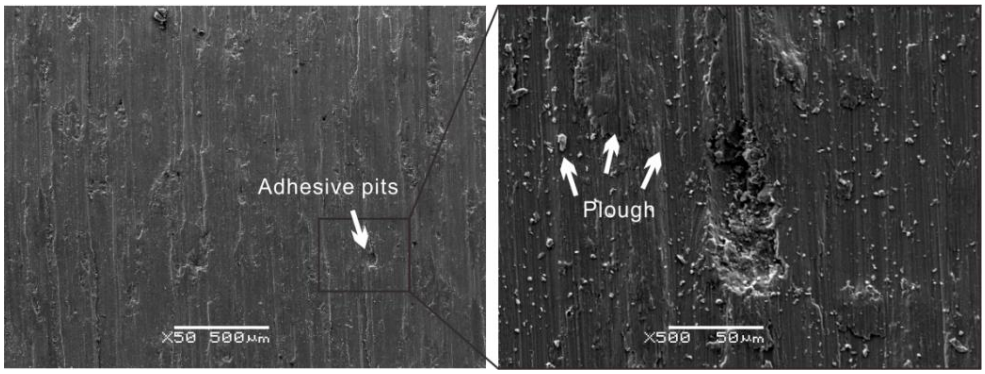

Figure 5. 3 Wear track of Ti after Pin on disk wear test, the worn surface was full of plough marks, and adhesive pits were also exhibited

Wear track of Ti displayed a combination of abrasive wear and adhesive wear characteristics, as observed from Figure 5. 3, the full distribution of plough indicates the mechanically removal mechanism dominated, however, in some areas exhibits adhesive wear. Ti materials was removed by adhesion of counter stainless steel pin, presence with the pits on the articulating surface.

In addition to investigate wear behaviour and degradation mechanism of NT surface, topography of worn NT surface was investigated by SEM as Figure 5. 4 shown, as share force concentrated at articulating surface of pin with disk can cause the tiny cracks and defects generated in the NT layer or beneath layer, which could lead to deformation of tubes, then the inhomogeneous distribution of normal force might bending, destructed nanotubes structure.

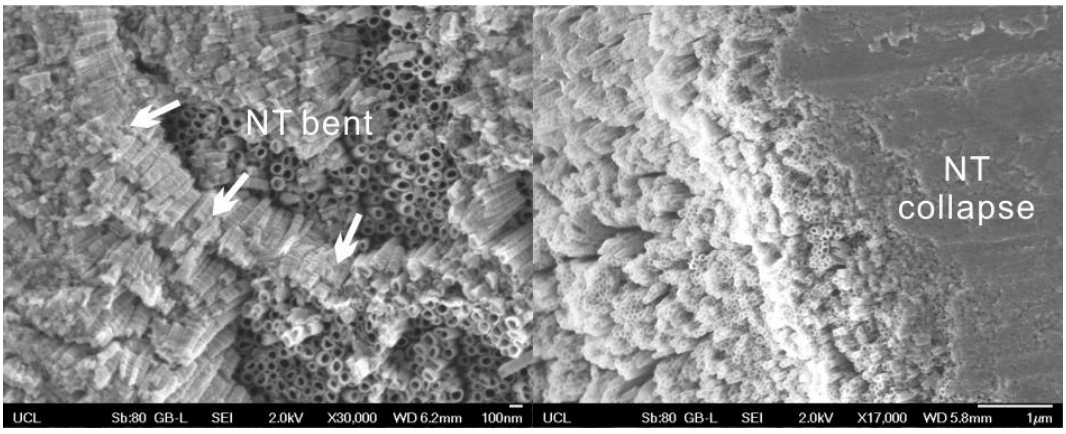

Figure 5. 4 Bending areas of nanotubes on NT after Pin on disk wear test, the nanotubes firstly bent as the stress concentrated and then nanotubes collapsed

The bent or deformed nanotubes can not only fail to improve osteointegration due to the collapse of nano structure, but also tend to detach from the substrate leads to wear debris generation. The detached nanotubes debris can easily trapped at bone

implant interface.

For the wear debris analysis, as the nanotubes break generates nanosized wear debris, it was difficult to obtain nanosized wear debris. However, the wear track measurement was an accessible method to investigate tribological behaviour as the pristine nanotubes topography was highly ordered, it was facile way to analysis the wear damage or wear scars from the specimen surface.

Wear behaviour of NT and SO-NT surface

As aforementioned the presence of NT improved the wear resistance of titanium surface, the further comparison pin on disk experiment was setup to further investigate the wear behaviour of NT and SO-NT. After six-stations pin on disk procedure was conducted to evaluate and quantify the volume loss of the NT and SO-NT samples after the wear tests (Figure 5. 5). After 1.2 × 10000 test cycles, the wear scar morphologies and wear volumes were examined. As shown in Figure 5. 5, the surfaces of three NT samples exhibited heavy wear and the Ti substrates were exposed, whereas light wear tracks were observed on the SO-NT samples. In addition, the morphologies of the spherical-ended stainless steel pins were examined. The wear tracks of the pins encountering NT were heavy and those encountering SO-NT were slight. To quantitatively analyse the volume loss of wear tracks for disks and pins, the aforementioned theoretical model in chapter two was employed. The calculation results showed that the volume losses were 0.48 mm^3 and 0.032 mm^3 for the NT disks and pins encountering the NT, respectively. By contrast, the volume losses were only

0.07 mm^3 and 0.007 mm^3 for the SO-NT disks and pins, respectively.

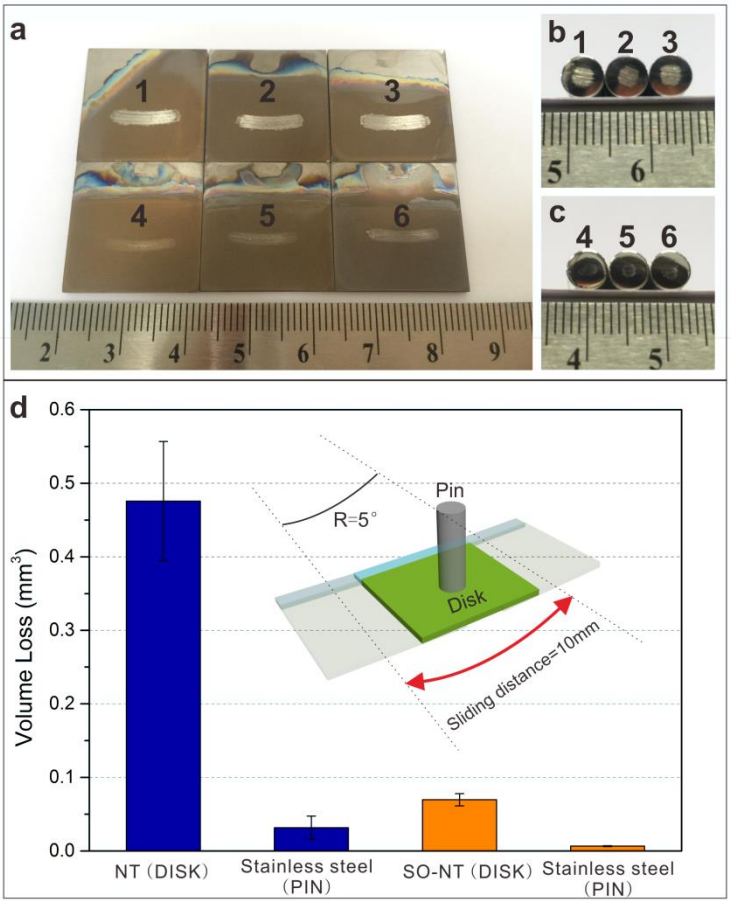

Figure 5. 5 Optical images of wear scar of NT and SO-NT after pin on disk test, a, b and c, volume loss, the pin on disk wear motion is illustrated in d

Apart from pin on disk tester, the ball on disk displayed similar trend. A ball-on-disk contact mode was used to investigate the tribological property. After the tests, the morphologies of the wear tracks were investigated. As shown in Figure 5. 6 a1 and b1, the widths of the wear tracks of the NT sample were approximately two times those of the SO-NT sample. The centre area of the wear tracks was selected to characterise the micro-area topography of scratches using a 3D MicroXAM-800 (Figure 5. 6 a2 and b2). Micro-sized ploughs were distributed on both samples, whereas the SO-NT sample exhibited less ploughs with clearer edges (Figure 5. 6 b2). The ploughs were

further investigated via HR-SEM. Examples can be seen in Figure 5. 6 a3 and b3. The plough width on the NT sample was 25 ±1 μm, which was approximately two times the width of that on the SO-NT sample (10 ±1 μm). Further, mass cracks in the vicinity of the plough on the NT surface were observed. By contrast, the SO-NT surface exhibited no cracks.

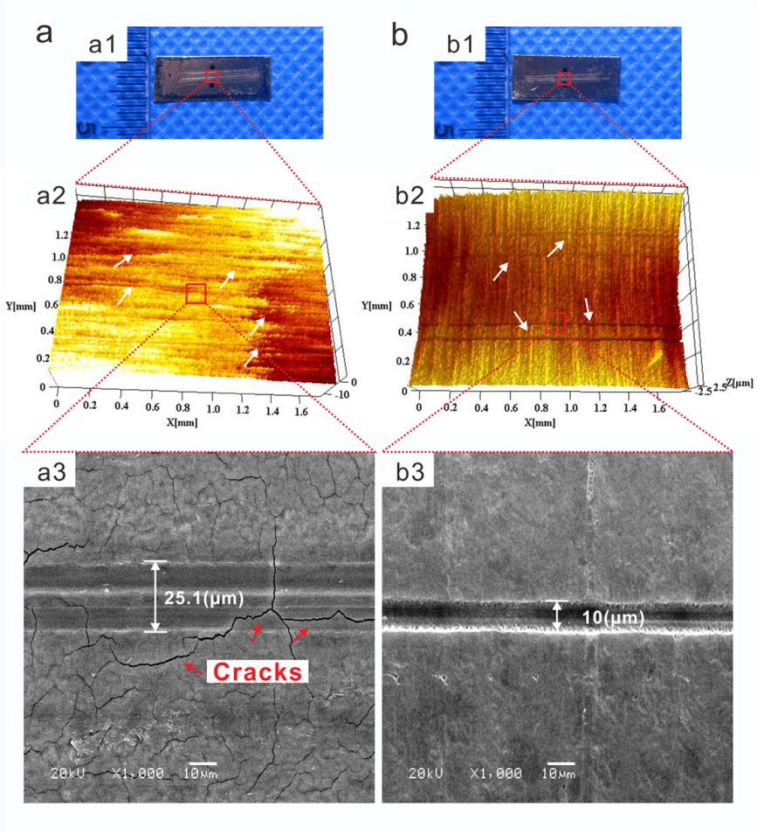

Figure 5. 6 Wear track of ball on disks (a) NT and (b) SO-NT samples. (a1,b1) Optical images, (a2,b2) topography of centre area in wear tracks, (a3,b3) and SEM images of ploughs

5. 3. 2 Friction study

Preliminary comparative analysis of flat Titanium surface and TiO_2 nanotubes structure

As biotribological performance including wear and friction, of Ti with polished surface and NT with nanotubes surface were further examined by monitoring friction coefficient during the biotribological test. The variation of friction coefficient with sliding cycles is show in Figure 5. 7. It was observed that the friction coefficient of Ti shows a typical abrasive wear as the coefficient raise with the increasing of cycles. At the initial sliding stage (up to 600 cycles), the coefficient was fluctuated around 0.15, then it the friction coefficient increased significantly. The coefficient increased to about 0.25 at after 1000 cycle test. after 1000 cycles, the increase rate of coefficient slow down but with steady increase.

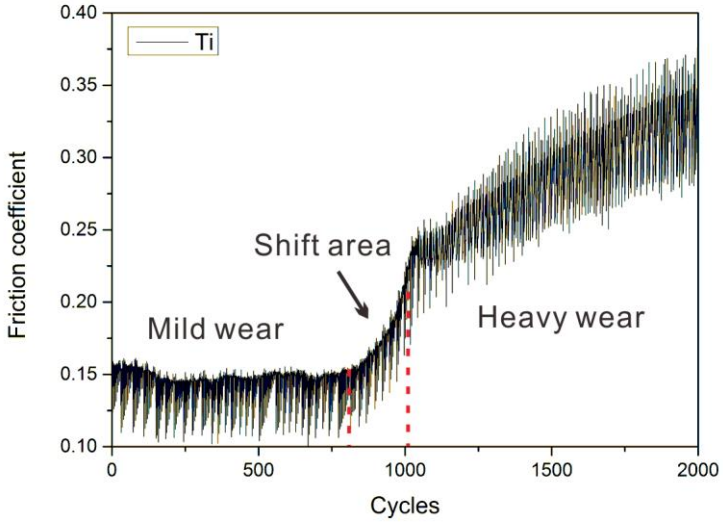

Figure 5. 7 Variation of friction coefficient of Ti with wear cycles countering stainless steel ball

The friction coefficient of NT exhibited a complete different behavior, the first stage of NT displayed 0.3 friction coefficient value higher than Ti (0.15) due to the higher roughness, in this stage, NT possibly featured with mild damage such as bending or/and smashed. However, the NT coefficient increased significantly at 600 cycles, the

phenomenon could be explained as the collapsed nanotubes detached and trapped at articular interface that generated a large amount of wear debris, these debris strongly affected the in situ roughness of articulating surface, led to the mass fluctuation friction coefficient at 600 to 1000 cycles. After 1000 cycles, the NT complete detached from substrate, and the coefficient were stable at 0.2 with slightly increase (turn to Ti surface wear behavior).

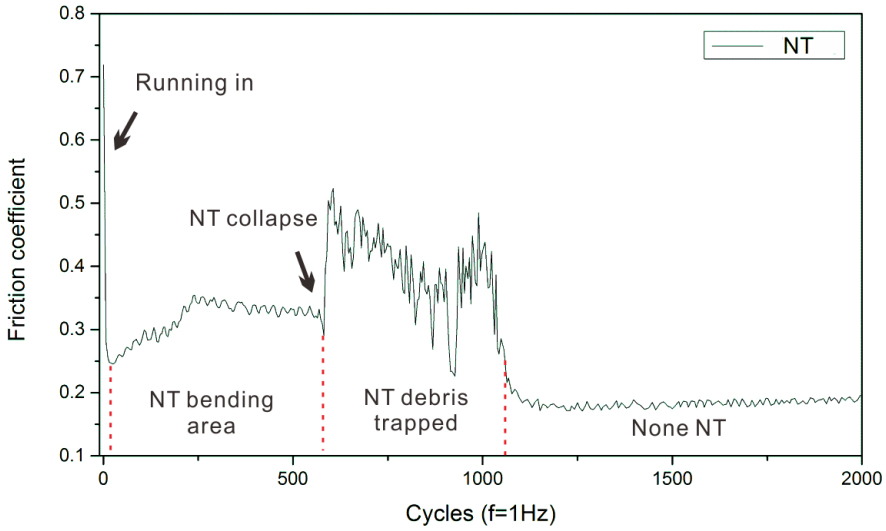

Figure 5. 8 Friction coefficient of NT with 2000 cycles countering stainless steel ball

Ti, NT and SO-NT friction coefficient investigate under constant condition

As the PTFE ball on disk with aforementioned parameters, the friction coefficient of Ti surface shows a slight above than 0.2 (Figure 5. 9). However, the coefficient displays two obvious signal fluctuations at 5500 cycles and 6000 cycles, and after 6000 cycles, the coefficient has a slight increasing then decrease to 0.2. Indicates the Ti surface started to be damaged and wear debris formed at the obvious fluctuations caused roughness increased instantly. After the two obvious fluctuations, the coefficient tends to decrease and mild. the magnified coefficient proves the slight but regular

fluctuations presence on Ti surface.

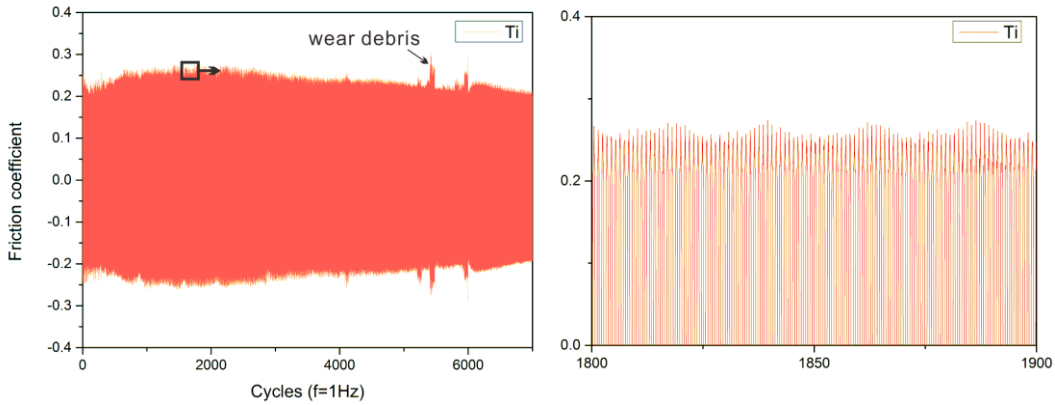

Figure 5. 9 Variation of friction coefficient of PTFE ball on Titanium disk (7 × 1000 cycles) and magnified coefficient from 1800-1900 cycles

Friction coefficient of NT illustrates different with Ti, the micro fluctuation of signal presence before 6000 cycles, especially around 2000 cycles (Figure 5. 10). As the magnified coefficient image indicates the features of NT, the coefficient was slight higher than 0.2, moreover, presence a mass wave around 0.2. The might due to the poor mechanical stability of NT, bend or detach under the shear, the detached nanotubes formed wear particle could lead to friction coefficient micro fluctuated.

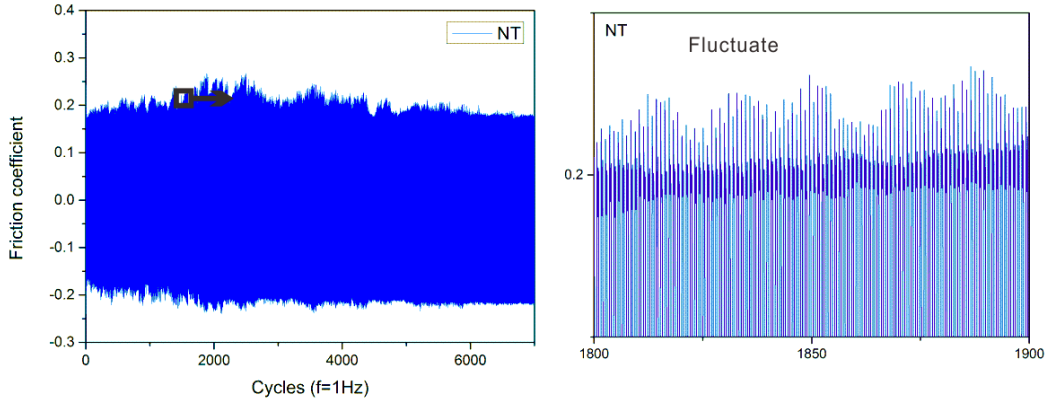

Figure 5. 10 variation of friction coefficient of PTFE ball sliding on NT modified Titanium disk (7×1000 cycles) and magnified coefficient from 1800-1900 cycles

As Figure 5. 11 shows, the SO-NT also exhibits slight below than 0.2 value of

coefficient. Furthermore, the significant difference between NT is the SO-NT not only with slight lower coefficient, but also performed much less micro fluctuation than NT. It was remarkable the absence of obvious fluctuations in SO-NT coefficient during 7000 cycles test, and the coefficient was more stable than that of Ti and NT. This indicates the SO-NT has generated the less wear debris than other two, and reserved the highest level of structure integration. The improved stability of friction coefficient maybe ascribed to the presence of bonding layer.

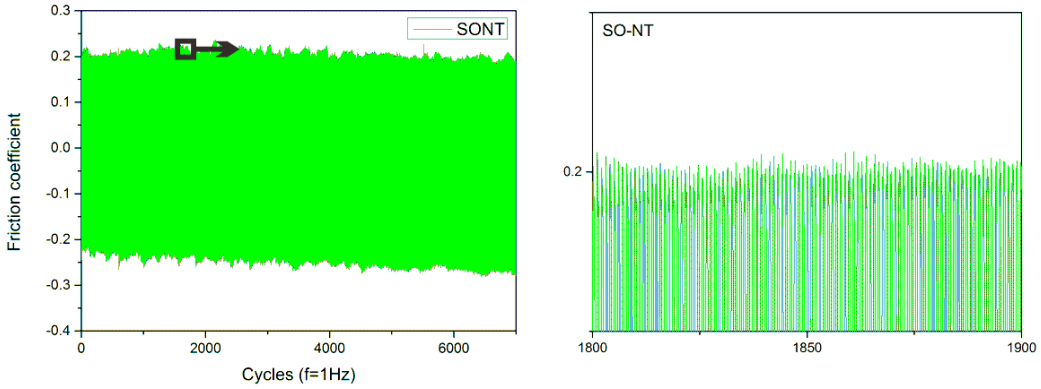

Figure 5. 11 Friction coefficient of SO-NT with PTFE ball on disk (7 × 1000 cycles) and magnified coefficient from 1800–1900 cycles

5. 3. 3 Fretting corrosion on Ti_6Al_4V medical grade bone screws

The fretting corrosion experiments were setup as illustrated in Chapter two, the characterization methods were illustrated aforementioned in materials and methods in this Chapter.

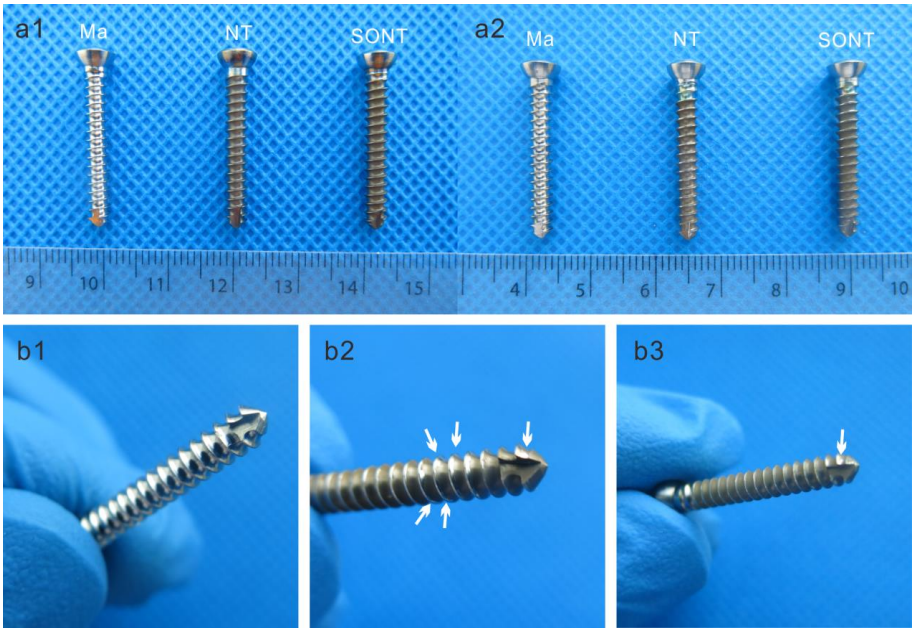

Figure 5. 12 Optical image of pristine Ma, NT and SO-NT screws (a1), after fretting (a2) and thread image after fretting b1 machined, b2 NT and b3 SO-NT

NT, SO-NT three screw surfaces were prepared (as machined, NT modified and SO-NT modified) for fretting corrosion test, as reported in Chapter 2. Optical microscope examination demonstrate that the majority of nanotubes film on both NT and SO-NT were maintained and no severe damaged after fretting test (Figure 5. 12 a1, before fretting and 12 a2, after fretting). However, obvious damages that exposure the alloy substrate were observed mainly located at thread ridge part. Thread bottom surfaces had no significant difference with screws before fretting. Obvious substrate exposure was also detected at the tapping areas on both NT and SO-NT, see Figure 5. 12 b2 and 12 b3. From Figure 5. 12 b2 and 12 b3, the optical observations showed areas of nanotubes film on NT threads ridge deboned, and the nanotubes on SO-NT were less damaged. However, the further investigate of detachment level by SEM is necessary.

Wear evaluate at tapping areas

Figure 5. 13 has shown the morphology of the fretting tested specimens. It revealed that three samples of drill areas was worn by countering cortical bone, the surface was possibly be damaged during the insertion. Figure 5. 13 b1 and c1 illustrates that the nanotubes layer on both NT and SO-NT screws tapping area were peeled with different level, however, b2 and c2 proved that the nanotubes layer on SO-NT was more integrated as it remained in the same area. NT screws on tapping exposed more substrate areas than SO-NT (Figure 5. 13 b1, b2, c1 and c2, white arrow). Ma surface also exhibits the worn at areas due to the asperity surface presence, however, it is difficult to compare damage level with NT and SO-NT.

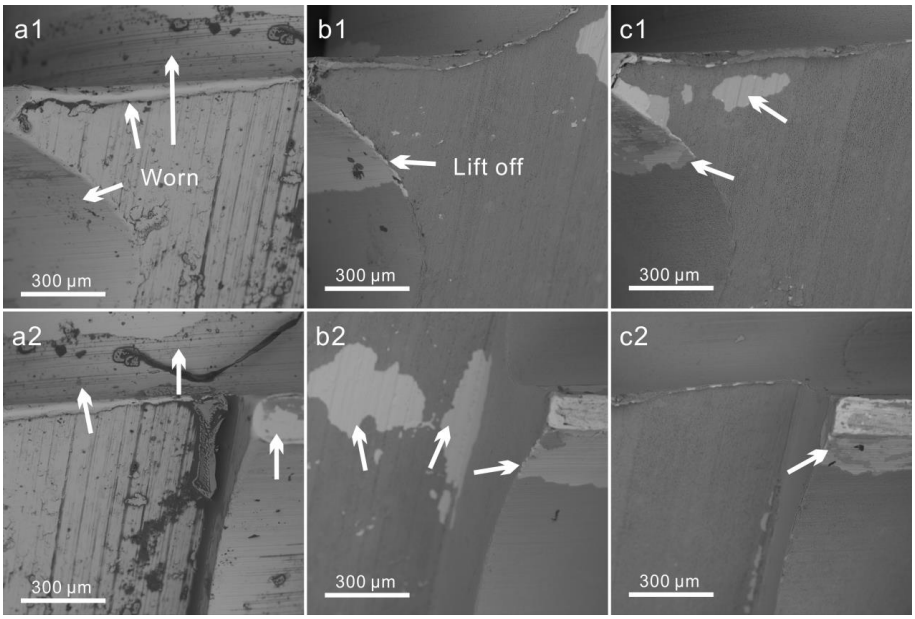

Figure 5. 13 Morphology after fretting on drill tapping plane, Ma screw a1 and a2, NT screw b1 and b2, SO-NT screw c1 and c2

NT and SO-NT integrity on thread

Figure 5. 14 illustrates Ma screw thread part has worn heavily. Apart from the thread worn, the surface damage was also remarkable at both above and beneath the threads (white arrows in Figure 5. 14, Ma-1 and Ma-4). However, the areas severe

worn on NT and SO-NT were not obvious due to the nanotubes layer plays a role of protective and isolative layer to screw substrate. The worn areas on NT and SO-NT were mainly distributed around the thread tip areas, all the nanotubes layer on five thread tips (Figure 5. 14, from point 1 on NT screw, NT-1 , to point 5 on NT screw, NT-5) was removed from NT screw. Furthermore, nanotubes at areas adjacent thread tip were also damaged and led to the exposure of substrate (see Figure 5. 14 NT-2, NT-3 and NT-4, white arrow). SO-NT exhibited an improved mechanical stability, as the nanotubes remained even in some thread areas (SO-NT-2 and SO-NT-5, black arrow). Moreover, some areas of destroyed nanotubes were displayed light gray (different with the substrate), indicating that the bonding layer still covered the titanium substrate (SO-NT-1 to SO-NT-5, red arrow).

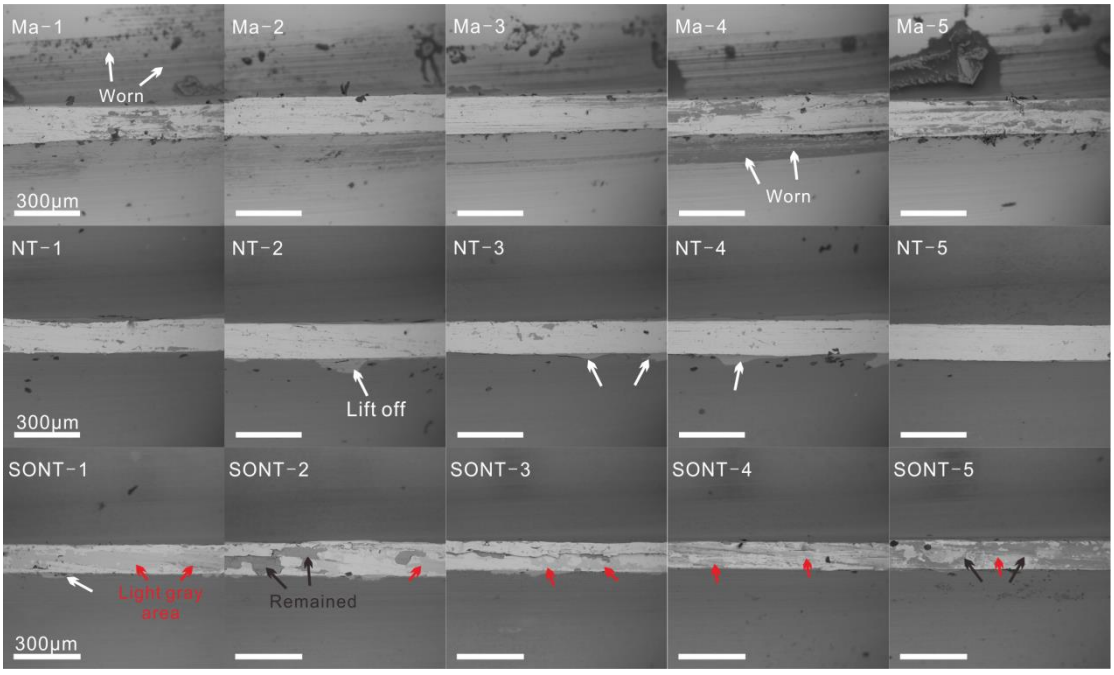

Figure 5. 14 Each SEM observation points on thread of machined (Ma 1-5) NT (NT 1-5) and SO-NT (SO-NT 1-5) screw, bar=300 μm

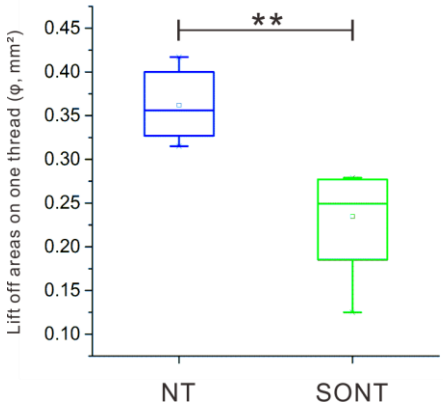

*Figure 5. 15 Debond off areas of nanotubes layer on thread for NT and SO-NT decorated screw, **, p<0.01. p value: 0.0051, Error bars represent standard error with the mean (s.e.m)*

With the methodology of lifted nanotubes quantitative analysis illustrated in chapter two fretting track observation, the debond off areas on one thread of NT and SO-NT were calculated. Figure 5. 15 illustrates the debond off areas on one thread (φ) of NT and SO-NT screw thread tip. SO-NT exhibited an average of 0.23 mm^2 areas damage, compared with 0.36 mm^2 value of NT, decreased 36.11%. In the five SEM selected points, it was interesting to note that point number 5 of SO-NT had a lowest damage of only 0.06 mm^2. The statistic shown the significantly difference between NT and SO-NT with a p value of 0.005 .

Ma, NT and SO-NT thread width measurement

Figure 5. 16 illustrates the selective measurement points (marked with 1, 2 and 3) on thread of Ma, NT and SO-NT. From the image, it was obvious that the thread width of Ma has highest value than NT and SO-NT, and NT thread was wider than SO-NT. Apart from the width, worn was observed at thread adjacent areas on Ma, and the nanotubes layer was detached and substrate exposed on NT thread. The quantitative

measurement proved that Ma screw displays the highest value of thread width measurement, with 172.13 µm in average, NT screw reached 154.81 µm and 121.25 µm for the SO-NT screw (Figure 5. 16).

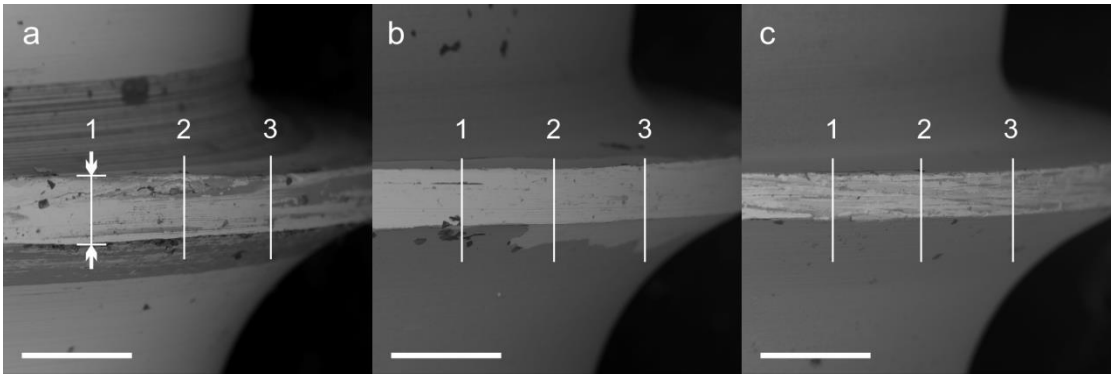

Figure 5. 16 Thread width measure points (white bar areas) of Ma(a), NT(b) and SO-NT(c), bar=300 µm. The thread width of SO-NT exhibited the minimum width than Ma and NT screw

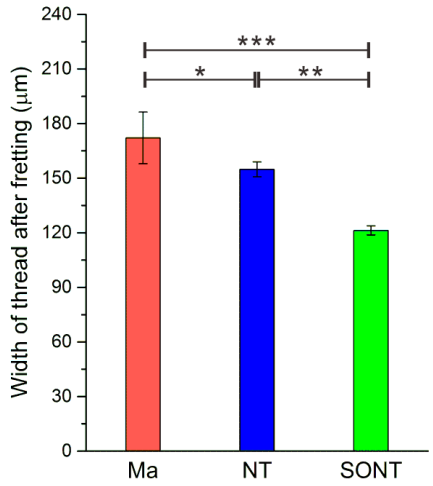

Figure 5. 17 Thread width of Ma, NT and SO-NT after fretting, *, p<0.05, **, p<0.01, ***, p<0.001

5. 3. 4 Biocorrosion of Ma, NT and SO-NT

Comparative analysis of Ma, NT and SO-NT screws by open circuit potential (OCP) before and after fretting test

Since Ti implant could be applied to implant surfaces that are commonly surrounded by blood-rich tissue, the corrosion resistance of titanium based implants plays a key role for implant success. Thus, the biocorrosion behaviours of Ma, NT and SO-NT should be evaluated. As described in Chapter two, the open-circuit potentials (OCP) of the Ma, NT and SO-NT samples were measured in a simulated body fluid (SBF) to mimic *in-vivo* atmosphere. Before fretting test, both SO-NT and Ma OCP curve were stabilized at –0.17 V *vs.* SCE, indicates the lowest tendency to corrosion (Figure 5. 18). By contrast, NT presented a lowest OCP value with –0.28 V *vs.* SCE. The results are in contrary with the previous studies of anodization on pure titanium [95].

After fretting test, the worn screws were immersed in refreshed SBF once again, and the Ma, NT and SO-NT surface all displayed decreased OCP value. Remarkable decrease of the OCP value was observed for Ma screw; once natural titanium oxide is mechanically depassivated during fretting with countering bone (or removal during insertion), the Ma screw exposed to corrosive environment, led to decreased OCP value, from –0.17 V to –0.36 V *vs.* SCE, with 0.19 V *vs.* SCE decreased value (Figure 5. 18 b.). In contrast, the decreased OCP value of NT was only approximately 0.04 V *vs.* SCE, from –0.29 V to –0.33 V *vs.* SCE. Meanwhile, the SO-NT was decreased same value, 0.05 V *vs.* SCE from –0.17 V to –0.22 V *vs.* SCE. However, SO-NT exhibits the highest value of OCP even after fretting, suggesting the mechanical stability of bonding layer to protect titanium against corrosion.

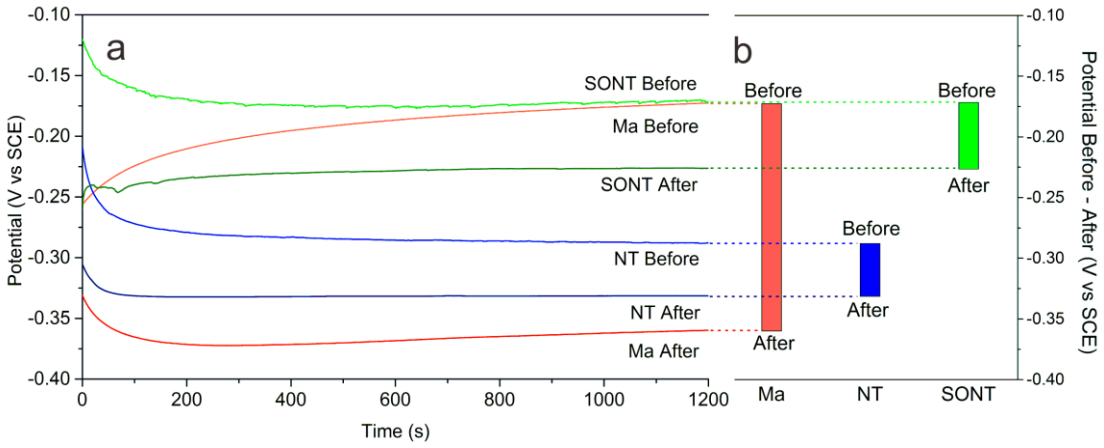

Figure 5. 18 Open circuit potential of Ma, NT and SO-NT before and after fretting (a) and decreased OCP of each screws after fretting (b)

Further comparison OCP value between NT and SO-NT

As the NT and SO-NT surfaces both with improved corrosion resistance than Ti, the further investigation of NT and SO-NT were soaked for 60 min in SBF with pristine foil samples, the OCP was recorded for 1500 s. As shown in Figure 5. 19, SO-NT (approximately –0.06 V) presented a lower corrosion tendency than NT (approximately –0.28 V). The OCP value indicates the sample surface activation, which can be active or passive. The electrochemical attack in SBF, which can erode the sample surface, leads to an ion release from the substrate into the medium.

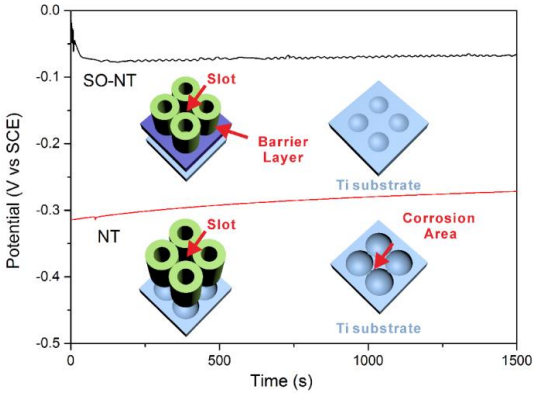

Figure 5. 19 OCP versus time and 'barrier function' of interfacial bonding layer in SO-NT

5. 4 Discussion

Biotribological performance

As SO-NT exhibits a significantly improved biotribology and biocorrosion resistance performance compared with Ti surface and NT surface. The effect of SO-NT on improving biotribology and biocorrosion-resistant were also observed on Ti_6Al_4V medical grade bone screws although the NT and SO-NT have a similar nanotubes topography, as shown in Figure 5. 20.

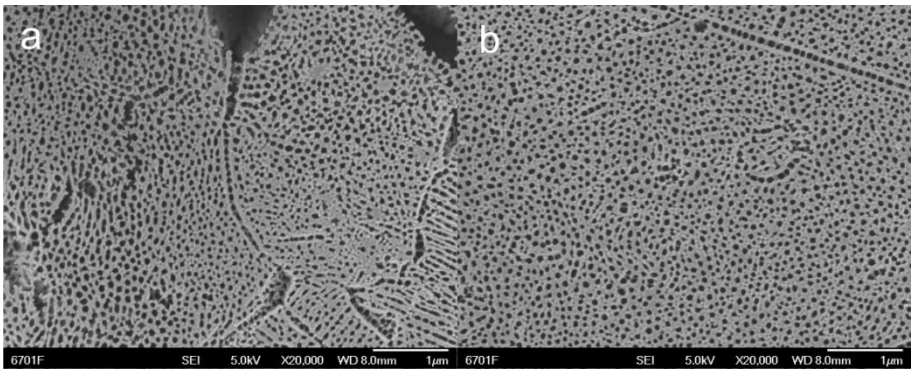

Figure 5. 20 Surface topography of NT (a) and SO-NT (b) modified Ti_6Al_4V

The excellent biotribological performance of the SO-NT layer can be attributed to interfacial bonding layer that strongly joint the nanotube layers to the titanium substrate. The surface hardness of the TiO_2 nanotube is quite different from that of the Ti substrate, this leading to the debonding of the nanotube layer from the Ti substrate under stress. As observed in nanoindentation test, the E-modulus of NT and SO-NT was no significantly difference (results are shown in Chapter 4, see Figure 4. 18), the improved tribological performance was not contributed by inducement of bonding layer. Owning to the interfacial bonding layer, the stress of the surface nanotube was gradually transit to the substrate. This contributed to the improved biotribological

performance of SO-NT modified surface.

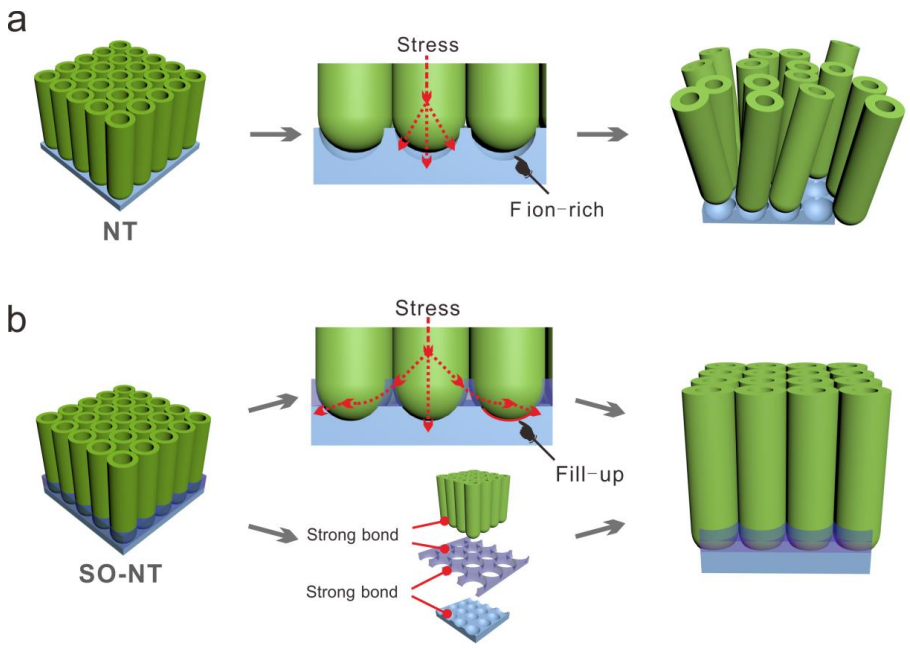

Figure 5. 21 Mechanism of interfacial layer for mechanical stabilities of (a) NT and (b) SO-NT samples under stress. The red dotted arrow represents the direction of stress conduction

According to the experimental results and FE analysis, the produced SO-NT samples exhibited excellent mechanical stabilities under harsh bending, twisting, shocking, ultrasonic radiation, and biotribological performance including fretting behaviour. The results illustrate from the special stress dissipation in SO-NT under shearing. Regarding the traditional NT samples, the accumulation of external stress caused an irregular arrangement of the once vertically arranged NT. The aggregation of disordered NT generated cracks, which led to the peel-off of the NT layer from the Ti substrate (Figure 5. 21 a). By contrast, SO-NT exhibited an impressive dissipation with no crack generation in the vicinity of the wear track. This observation indicates the possibly advantageous mechanisms of the SO-NT sample compared to

conventional NT samples (Figure 5. 21 b). Furthermore, the thickness of bonding layer plays a dominate role by affecting the adhesion strength; A thicker anodic layer tends to detach, however, the bonding layer in this study measured only 120–150 nm. Apart from these two characteristics, the improved mechanical stability of SO-NT is possibly related to the strong bonding at the two interfaces (bonding layer–Ti substrate and bonding layer–NT layer). The strong bonding interfaces are essential for a continuous dissipation of external stress without stress concentrations at the half-spherical bottoms of the NT layer. The FESEM bottom view (Figure 4. 6 c and d) shows that the contact area of the SO-NT–Ti interface was covered by the bonding layer. With bonding layer, the original NT bottom with half-spheres exhibited tiny bulges and the bonding layer filled the space between NT bottoms and Ti substrate, which was generated by fluorine ions during anodization. According to the cross-section images (Figure 4. 6 a and b), no edge existed at the bonding layer–NT interface. Hence, the bonding layer was tightly wrapped around the NT bottoms. Another possible mechanism is the altered stress dissipation of the NT layer through the bonding layer. Owing to the strong bonding at the bonding layer–NT interface, the stress is distributed and dissipated. The subsistence of a hyperfine bonding layer with 100 nm grain (Figure 4. 5) contributes to a reduction of stress concentrations via a stress transmission from the in-situ tube bottom to grains on the bonding layer and adjacent tubes, thereby acting as a ground foundation. The assumption is confirmed by the analysis on wear ploughs and wear tracks (Figure 5. 4 and Figure 5. 5).

The improvement also effective to fretting behaviour on bone screws, fretting

corrosion are widely presence in many kinds of orthopaedic and dental implants. Despite with the widely investigation of fretting corrosion caused by module designing of implants (hip taper), the fretting corrosion at bone implant interface should be given more attention. As inserted implants with appropriate initial contact to adjacent bone generates physical stress at the interface, however the shear featured with relative micromotion also generated at interface. The continuous micromotion combined with biological corrosive (fretting corrosion) generates foreign debris are convinced leads to chronic inflammatory and/or aseptic loosening [88, 126, 158, 159]. Meanwhile, the NT has been proved as its ability to improves osteointegration in many in vitro and in vivo studies, however, the long term of fretting corrosion of NT was hardly reported. After insertion, according to the fully mechanical contact at bone-thread interface, threads tips have a more severe fretting in some areas than others. By the methodology aforementioned of quantify nanotubes debond off areas, the SO-NT exhibited 40% less of nanotubes debris released than that of NT. Although the damage was only at square micro meter range, detached nanotubes from substrate might substantial individual tube generate a micro sized cluster would release into the bone and cause tissue reactions. In vivo tissue reactions for nanotubes are still barely studied, nevertheless the micro-sized wear debris released in tissue has been widely proved to be toxic to cells.

Furthermore, nanotubes layer as a layer of TiO_2 covers alloy substrate and plays a vital role to protect titanium implant, the nanotubes detached areas on implantation would expose substrate directly into the biocorrosive in vivo atmosphere, leads to the

metal ions release from the areas. Moreover, the measurement of thread width of three screws also proved the SO-NT was with the highest capability to protect thread worn, as debris generated by worn of thread could be easily trapped at interface.

Biocorrosion Improvement

The erosion process of NT can be initiated in locations where the fluid directly touches the Ti substrate through slots or structural defects between adjacent tubes, thereby attacking the Ti–NT bottom interface. The ions from the adjacent substrate can be transmitted to the area of initiated erosion and react with the ions in the media, which leads to point corrosions at the NT–Ti interface. Further, the process might increase the ion release of Ti and generate micro pits at the interface, which would cause a lift-off of the NT layer in the long term. In this study, the 120–150 nm dense bonding layer acted as barrier to isolate the SBF solution from the slots between NT (Figure 5. 22).

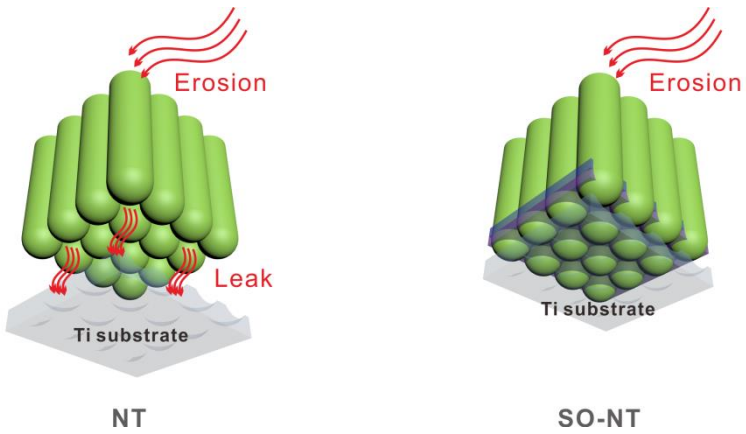

Figure 5. 22 The bonding layer at nanotubes bottom acts as isolating barrier from corrosion

Moreover, the barrier was tightly connected to the NT bottoms and prevented the media from reaching the Ti substrate. This characteristic promotes a passive

electrochemical environment and improves the SO-NT corrosion resistance.

The biocorrosion-resistance improvement of the bonding layer presence is more effective due to the difference growth mechanism between NT and SO-NT on Ti_6Al_4V alloy. As the NT and SO-NT were successful generated on TC4 medical screws, micro pits were formed on the both nanotubes surface was due to erodes attack of the vanadium oxide during the anodisation in fluorine containing electrolyte, which was reported by Patrick [82, 156]. The EDX measurement well proved the presence of bonding layer at micro pits areas. On nanotubes areas, both NT and SO-NT consist above 55% of oxygen, 23–25% of titanium, 10% fluorine, 7–8% carbon and less than 3% vanadium (Figure 4. 15 and 4. 16). However, the chemical composition in pits area shows a significant difference. As NT pits contains 54% titanium, 21% fluorine, 17% carbon, 5% aluminum and 3% vanadium. Indicates the composition of alloy substrate without the presence of large amount oxides. Furthermore, the fluorine contains was two folds than that at nanotubes areas. This has been ascribed to selective dissolution, the vanadium contains phase (β phase) was enhanced etching in fluorine containing electrolyte, due to the high solubility of vanadium oxide [156]. The chemical composition of SO-NT pits areas contains same value of oxygen, titanium, fluorine compares with nanotubes areas. Confirmed a layer of titanium oxides was formed at pits areas.

The lower OCP value of NT on Ti_6Al_4V could be ascribed to the formed micro pits during anodization, the formed pits were 'channels' linked corrosive bio-fluid to substrate while immersed in SBF environment, led to NT surface corroded. The

improvement of corrosion resistance of SO-NT are related to bonding layer at the interface of nanotubes bottom and alloy substrate, as it protects the screw from erosion. From the initial OCP value of SO-NT, the bonding layer sealed the micro pits at nanotubes bottom to obstruct the aforementioned 'channels' (Figure 5. 23).

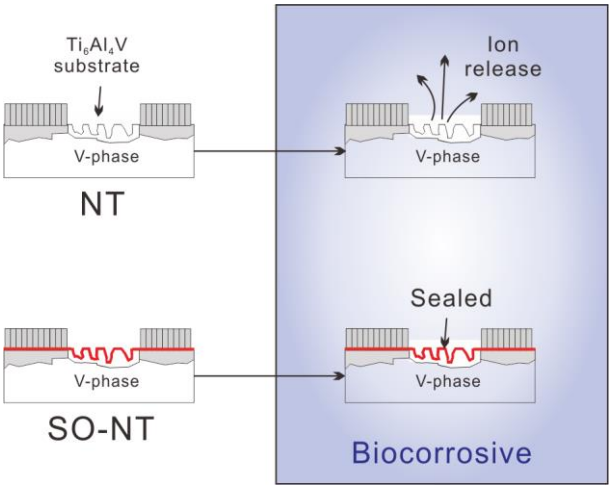

Figure 5. 23 The containing vanadium phase dissolve during nanotubes generation process that caused micro pits formed, leads to substrate exposure. Bonding layer plays vital role to seal the pits

5. 5 Conclusion

To improve the mechanical stability of traditional NT on titanium substrate, in particular their biotribological performance for potential applications as implants, we prepared SO-NT by creating an interfacial layer between NT layer and titanium substrate (or Ti_6Al_4V alloy) that join the NT layer and Titanium layer strongly. The bonding layer could effectively resist a debonding and improve the mechanical stability of the NT array under dynamic shearing. Moreover, electrochemical OCP tests revealed that the produced SO-NT material possessed an improved

anti-corrosion behaviour according to its higher open-circuit potential (–0.06 V) compared to that of NT (–0.26 V) in SBF on flat Ti surface.

Furthermore, the NT and SO-NT were generated on medical grade TC4 screws and the fretting and corrosion behavior were investigated by a bone screws ex-vivo fretting simulation system and OCP carried out in SBF before and after fretting. Fretting tests conclusions include:

1. OCP value of NT on was lower than that of Ma surface, indicating that NT on alloy has more tendency to erosion. OCP of Ma screw decreased significant after fretting that exhibited a poor mechanical stability of a bare alloy surface.

2. SO-NT displayed highest OCP value both before and after fretting (before fretting exhibited 0.001 slightly high than Ma). Before fretting, Ma OCP value was similar with SO-NT, after fretting changed to 1.59 fold than that of SO-NT. Furthermore, NT OCP was 1.68 fold than SO-NT OCP before fretting, and was 1.46 fold than SO-NT OCP after fretting. Impressively, the OCP value of SO-NT after fretting was still higher than NT OCP before fretting, means even after fretting damaged SO-NT screw showed an improved corrosion resistance than pristine NT screw.

3. From the friction study, the degradable process of nanotubes was nanotubes bending, collapse and debris generation. The friction of Ti, NT and SO-NT were measured by tribometer, with 0.2 value.

4. SO-NT has displayed with great improved wear resistance than NT as the bonding layer can dissipate external stress. Owing to the strong bonding at the bonding layer–NT interface, the external stress is distributed and dissipated. From pin-on-disk

wear test, the calculation results have showed that the volume losses of NT was 0.48 mm^3, whereas the SO-NT volume loss was only 0.07 mm^3.

5. The fretting tests demonstrated that the proportion of SO-NT deboned area was 62.64% in NT debonded area, indicates if consider the lifted debris all trapped at bone-implant interface, the SO-NT screw would release 40% less debris than NT screw. Furthermore, the SO-NT thread width (121.25 μm) was narrower than NT (154.81 μm), meaning the alloy substrate beneath SO-NT film was less damaged and worn. SO-NT surface displays an enhanced fretting and biocorrosion resistance compared to NT and Ma surface screw.

6. The contribution of improved biocrrosion on Ti_6Al_4V with the presence of bonding layer on SO-NT not only covers the slots or defect on nanotubes areas, but also seal the pits that exposed Ti_6Al_4V substrate on pits areas. Combined these two mechanisms, the corrosion resistance of SO-NT enhanced significantly than NT.

Chapter 6

6. Cell–material interactions through ECM adsorption on nanomaterials

This chapter investigated osteoblast attachment to titanium dioxide (nano) on pristine titanium, NT- & SO-NT-modified surfaces, as well as the effect of nanostructures such as nanoflat, nanoconvex and nanoconcave ones. Osteoblasts were cultured on titanium, NT and SO-NT to test the attachment and viability of cells. Titanium with NT and SO-NT demonstrated enhanced cell attachment. However, the osteoblasts' attachment behaviour mechanism was unclear. To understand the mechanism of initial attachment of osteoblasts, nanoflat, nanoconvex and nanoconcave surfaces were fabricated and the cells' attachment to these surfaces was examined. The attractive force between charged nanotopography and ECM–Coulomb force was estimated and calculated to explain the cell attachment though ECM adsorption on nano topographies. From the calculative model, the effective attachment of osteoblasts on nanoconcave surfaces was ascribed to the uniform distributed fibronectin attracted by Coulomb's force on concave surfaces, caused by electron dynamics during fibronectin adsorption. Meanwhile, the nanoconvex surface also generated a Coulomb force with different electron dynamics, compared with nanoconcave ones; the Coulomb force produced on a convex surface is higher and more concentrated, leading to an inhomogeneous fibronectin distribution. Coulomb's

force on the nanoflat surface was too weak to 'anchor' fibronectin onto the surface, affecting the formation of stress fibre formation and leading to the formation of a spherical cytoskeleton rather than the spindle shape observed on nanoconcave surfaces.

This work first demonstrated the influence of micro attractive forces at the ECM-nanomaterial interface by experimental investigation. The electrostatic attraction–Coulomb force, through negatively charged fibronectin mediated by cations attracted to the negatively charged titanium surface (Figure 6. 1), is the dominating factor at the nanoscale in terms of regulating cell attachment. This work has also extended the knowledge of cell-material interactions. The reported nanoconvex and nanoconcave surfaces have the same value of surface ratio; however, they have different cell responses, indicating a more complex underlying mechanism for the cell-material interactions.

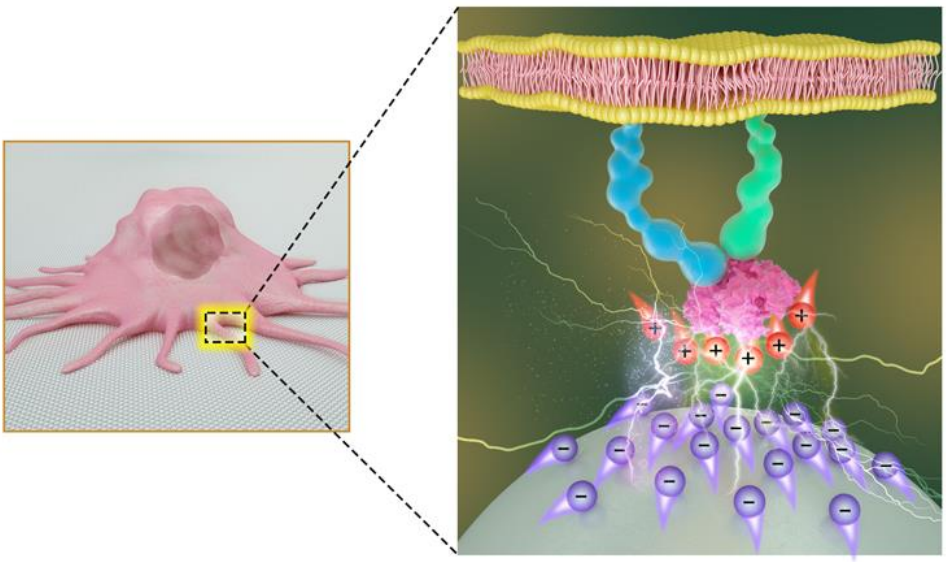

Figure 6. 1 Cell-Nanoconvex interaction, fibronectin adsorbed on nanoconvex top mediated by cation, and dominated by Coulomb's force

6.1 Introduction

Cell responses to implant material are crucial for the service performance of the implants. Since the artificial implant was invented, this area has become the central issue of tissue engineering. However, cell-material interactions are still not fully understood [160]. Such interactions referred to comprise the phenomena involved in adherent cells' attachment to a biomaterial surface, and their related cell functions such as growth, differentiation, migration or apoptosis. Furthermore, the extracellular matrix (ECM), a three-dimensional network of macromolecules, interact with cell membrane receptors and provide structural and biochemical support for surrounding cells [161].

Because NT represent a novel nanomaterial used to promote osteogenesis arising from culture hMSC on NT, one of the key findings was, for cells on NT, the NT diameter significantly affects almost all aspects of cell viability [82]. For example, 15 nm diameter NT strongly promote mesenchymal stem cell adhesion, proliferation and differentiation, whereas 100 nm diameter NT were found to be detrimental, inducing programmed cell death [57]. However, other researchers have shown contrasting results—for small NT, there was no difference in adhesion promotion, and the large NT significantly induced osteogenic differences [55]. Thus, slight differences in nanotopography can strongly affect cellular behaviours. Under the cell-sense scale, NT topographies contain tube ridge (the thickness of tubes) changes from 10–30 nm; the hollow space inside tubes varies from 15–100 nm in diameter and the interspace

changes between tubes. Which structure affects or adsorbs ECM is unknown; hence, NT could be seen as a nanotopography comprising three kinds of sub-nanotopographies, as aforementioned. This unsolved question is one of the main barriers that limits NT's application. A concise understanding of cell material interaction includes a thorough determination of cell biology and cell-ECM interactions to be extrapolated to the biomaterial surface for tissue engineering applications [162].

In this chapter, previous research findings into cell material interactions are reviewed. Furthermore, preliminary research of cell material interactions was investigated through the comparative analysis of nanoflat, nanoconvex and nanoconcave nanotopographies. This chapter aims to develop nanofeatured materials that can reveal and/or further understand the interaction of ECM and nanomaterials.

6.1.1 Cell–Material interaction: Theoretical model

Recently, the interaction between cells and material has been investigated using a molecular dynamics method. One of the proposed but important explanations was that the attraction between the negatively charged titanium surface and a negatively charged osteoblast is mediated by charged proteins (such as cation-mediated fibronectin) with a distinctive quadrupolar internal charge distribution [59]. Because osteoblasts are negatively charged, they are electrostatically repelled by the negatively charged titanium surface as long as some other attractive forces are not present in the system [163].

It has also been theoretically calculated that osteoblasts are strongly bound along the

nanosharp convex edges of nanorough titanium surfaces where the magnitude of the negative surface charge density is the highest due to the higher concentration of electrons. Therefore, the electric field strength adjacent to the highly curved edge of a titanium surface was estimated in the limit of a particularly sharp edge. Then, equilibrium and dynamic models were constructed by Ekaterina and co-workers to test the effects of integrin molecule-binding energy, aggregation energy and intrinsic curvature on the integrin-mediated adhesion of osteoblasts to nanorough and -smooth titanium surfaces [59]. In the process, surface-bound proteins and biomolecules play vital roles in cell material interactions. Furthermore, it was suggested that the contact and/or interaction between osteoblast plasma membranes and materials is established in two steps—the electrostatic force (Coulomb's force) generated by the material surface leads to the cell membrane first making a nonspecific contact, followed by a second step of specific binding, such as integrin assembly behaviours into focal contact [57, 164]. The original attractive interactions between mediated positively charged proteins and material and cells in the first step are illustrated in Figure 6. 2. Because two adjacent negatively charged titanium and osteoblast surfaces repel each other without proteins, once a sufficiently high concentration of bound proteins with a quadrupolar internal charge distribution occurs, the force between two negatively charged titanium surfaces and cell membrane becomes strongly attractive, leading to an equilibrium distance approximately equal to the dimension of the proteins [59].

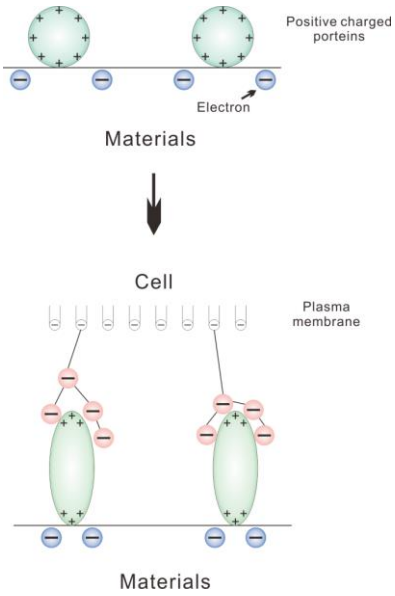

Figure 6. 2 Schematic of the orientation of quadrupolar proteins with positively charged tips attached to a negatively charged titanium surface. The quadrupolar protein mediated attraction between a negatively charged titanium implant surface and a negatively charged osteoblast surface [59]

Due to the behaviour of mediated quadrupolar proteins affected by material surface charge density, the increased electric field strength and surface charge density at the nanorough areas may promote protein adhesion.

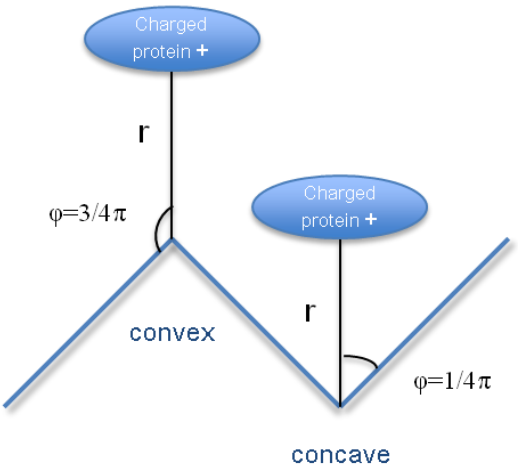

Figure 6. 3 Schematic illustration of Electric field (E) at convex and concave [59]

For example, a nanoconvex surface with a particularly high curvature (Figure 6. 3). According to the model provided by Ekaterina [59], the electric field (*E*) at convex is:

$$E\left(\varphi = \frac{3}{4\pi}\right) = -\frac{2A_1}{3}\frac{1}{r^{1/3}}e_r \qquad \text{Equation 6. 1}$$

where,

φ is the clockwise angle with the material surface,

r is the distance between convex and charged protein,

A_1 is a constant determined from the additional boundary condition,

e_r is unit vector,

and the surface charge density (σ(r)) is:

$$\sigma(r) = \varepsilon_r\varepsilon_0 E_n(r, \varphi = 0) = \varepsilon_r\varepsilon_0 E_n(r, \varphi = 3\pi/2) = -\frac{2A_1}{3}\frac{\varepsilon_r\varepsilon_0}{r^{1/3}} \qquad \text{Equation 6. 2}$$

where,

ε is the permittivity of the free space.

From equation (2), the surface charge density (σ) grows rapidly and would be infinitely large at the infinite sharp convex tip (positive correlation with curvature).

Meanwhile, the E of the concave surface was also illustrated:

$$E\left(\varphi = \frac{1}{4\pi}\right) = -2A_1 r e_r \qquad \text{Equation 6. 3}$$

where,

φ is the counter-clockwise angle with the material surface,

r is the distance between convex and charged protein,

A_1 is a constant determined from the additional boundary condition,

e_r is unit vector,

and the surface charge density (σ(r)) is:

$$\sigma(r) = -2A_1\varepsilon_r\varepsilon_0 r \qquad \text{Equation 6. 4}$$

where,

ε is the permittivity of the free space.

Equation 6. 4 means an infinitely sharp concave corner, leading to a zero surface charge density σ.

Thus, the surface charge density of the convex edge would decrease in magnitude with increasing curvature radius. In contrast, the surface charge density and the electric field strength would monotonously increase with increasing curvature radius of the corner (concave edge).

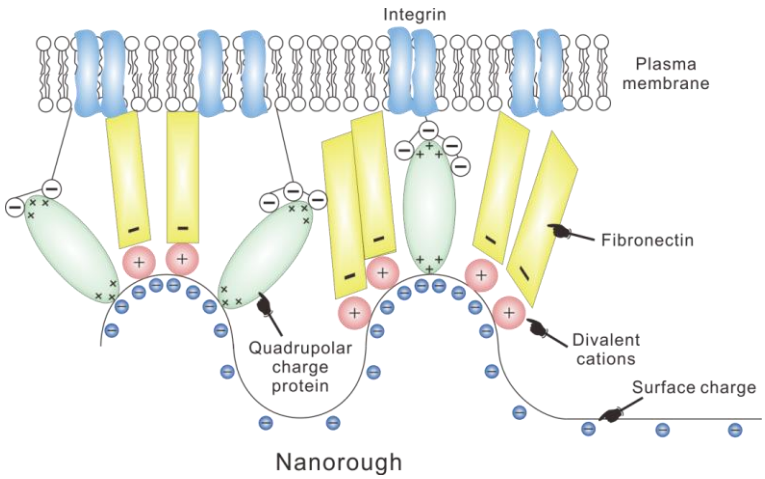

Figure 6. 4 The protein mediated adhesion of cell to the nano-rough region is facilitated by the increased surface charge density and electric field strength at highly curved convex edges and spicules

As illustrated in Figure 6. 4, the charged proteins are more likely to be distributed at edging regions of the convex, concave and flat surface, which have higher surface charge density, leading to initial protein binding. The theoretical model has explained the mechanism of cell nanorough material interaction well for the nanoscale of proteins' initial adsorption/immobilisation/binding process on nano topography. Meanwhile, this model can only be applied on metal-based nanorough materials due

to the completely passive charge on metal surfaces (electrons are distributed at the metal surface). However, the theoretical model has not been demonstrated by experimental investigation yet due to the fabrication difficulty of nanorough topography as a result of regularly changing the curvature.

6.1.2 Cell–material experimental investigation

Because nanotopography can influence stem cell behaviour, experimental investigations mainly focus on fabricating pillars/pits on a nano scale and changing the arrangement. With different topographies, cellular responses to these surface features are observed with respect to filopodia extension, mechanotransduction and stem cell differentiation. All cellular responses are related to the behaviours of receptors, including internal and cell-surface ones.

Prof. Dalby has contributed impressive works in this field. Cell adhesion to a material is often mediated through an intermediate layer of proteins adsorbed onto the material surface, termed the extracellular matrix (ECM) [165]. One of these receptors—integrins—play the key role in tethering the ECM to the transmembrane, and ligate to peptide motifs such as arginine, glycine and aspartic acid (RGD) tripeptide [166]. Due to the actin cytoskeleton being tethered to integrins, the interaction between matrix and integrins causes pulling and clustering of integrins into groups, and the integrin clusters form cell adhesions [167, 168].

The size of cell adhesion, focal adhesion is critically important for cell behaviours such as cell fate. The adhesion types can include dot and dash adhesion; dot adhesion are

of small size and related to cell motility, whereas dash adhesions are elongated and associated with stability and cytoskeletal tension [169]. However, further classification of cell adhesion was necessary; today, adhesions are classified with focal complexes (<1 μm), focal adhesion (1–5 μm) and supermature/fibrillar adhesion (>5 μm) [170]. Furthermore, due to the integrins having no enzymatic activity, the cell adhesion process can cause an intracellular signalling cascade triggered by protein tyrosine kinases, such as focal adhesion kinase (FAK) accumulating at the integrin cluster [171]. Because lithographical techniques are used to immobilise RGD peptides at various nanoscale densities, a packing density below 70 nm enables cell adhesion formation. However, above this density, clustering and maturation into focal adhesion are inhibited [167].

The focal adhesion behaviour is also crucial for mesenchymal stem cells (MSCs). MSCs can attach but cannot form mature adhesions on 2D stiffness modified polymer surfaces; furthermore, MSCs differentiate into adipocytes [172, 173]. However, MSCs need to generate/form supermature, larger-than-5 μm adhesions to differentiate into osteoblasts. The Rho-associated protein kinase (ROCK) plays a key role in this process, due to supermature adhesion facilitating intracellular tension through ROCK, triggering the expression of osteoblast-specific genes [174, 175]. It has been documented that the extent of intracellular tension, defined by formation of cell adhesions, guides MSC differentiation involving low tension that leads to adipogenesis, whereas high tension facilitates osteogenesis [172, 173].

MSC differentiation into osteoblasts was investigated by seeding cells onto a

nanotopography (nanopits) with disordered, highly ordered and randomly ordered arrangements. Electron beam lithography (EBL) was used to create nanopits on a silicon surface of 120 nm in diameter and 100 nm in depth with a random displacement in ± 50 nm (NSQ50), and the NSQ50 has been demonstrated with powerful osteoinductive cues. By contrast, highly ordered symmetries (with a decreased osteoprogenitor cell density compared with a planar control) were noted, particularly on a hexagonal array (centre to centre); furthermore, the highly ordered nanotopography produced low to negligible cellular adhesion and osteoblastic differentiation [174]. This work provides an effective strategy for orthopaedic implant surface nanotopography design. In addition to nanopits generated by EBL, nanopillars were also fabricated by anodisation in combination with a PS-bP4VP block templates mask method. This method can produce titanium nanopillars of precisely controlled dimensions, and positioning can be used to form lithography-like patterning. MSCs of 8 nm and 15 nm patterned nanopillars exhibit a trend of a higher number of large, supermature (>5 μm) osteogenic focal adhesions compared to control flat titanium surfaces [176].

6.2 Materials and Methods

6.2.1 Osteoblast culture on Ti, NT and SO-NT

Cell culture

Osteoblasts (MG63) were cultured on specimens (cut into 10×10 mm) for 24 h and 72

h with 10,000 cells on each specimen. Cells were maintained with DMEM containing 1% penicillin and 0% foetal bovine serum (FBS).

Live/Dead cell viability

A Live/Dead Cell Double Staining Kit was utilised for simultaneous fluorescence staining of viable and dead cells. This kit contains calcein-AM and propidium iodide (PI) solutions, which stain viable and dead cells, respectively. After staining, a Zeiss microscope was applied to observe the live/dead cells, then ImageJ 1.47V software was used to count cell numbers.

6.2.2 Nanoflat, Nanoconvex and Nanoconcave topographies fabrication

Nanoconvex and nanoconcave topographies used in this work were fabricated on pure titanium foil (99.6+% purity, 1.5 mm thickness, GoodFellow) using anodisation. In brief, the titanium foils were immersed in ethylene glycol (Fisher Chemical) with 0.5 wt.% NH_4F (>98.0%, Fisher Chemical) as the anode; the countering cathode was a graphite sheet. The reaction was performed under a constant 40V (DC) for 30 min. Then, the titanium foil was immersed into DI water and vibrated in an ultrasonic cleaner to polish the titanium. Again, the polished titanium foil was anodised in similar conditions for 30 min to generate a TiO_2 nanotube film, and dried in air. After that, the anodised surfaces were coated with epoxy glue (rapid adhesive, Araldite) to peel the TiO_2 nanotube layer off the titanium foil. Thus, the topography on epoxy-based nanoconvex, and nanoconcave topography was on titanium foil. The nanoflat topography was fabricated on silicon wafers using an electron beam evaporator, with

a layer of titanium (~50 nm, thickness ±10%) deposited by an electron beam evaporation method with a 0.02 nm/sec deposition rate. After evaporation, the nanoflat titanium silicon wafer was cut into 10×10 mm^2 squares.

6.2.3 Topographical & Surface charge characterization–Atomic force microscopy (AFM) & Kelvin probe force microscopy (KPFM)

AFM

The precise shape and dimensions of nanoconvex and nanoconcave surfaces were examined using an atomic force microscope (AFM, Bruker AXS Dimension Icon) with a ScanAsyst cantilever (0.4 N/m) in PeakForce Tapping mode. High-resolution scans were carried out for the nanoflat topography.

KPFM

Surface potential was characterised by a Kelvin probe force microscope (KPFM, Bruker AXS Dimension Icon) with a sample bias model (Wsample = Wtip + potential). For nanoconvex and nanoconcave topographies, the Kelvin probe used a PFQNE-AL cantilever 0.8N/m in PeakForce Tapping Kelvin probe AM. The tip function was 4.4 eV KPFM surface charge for the nanoflat surfaces and was applied with the blunter tip that provides lower resistance, and with sample bias; the tip work function was 4.29 eV calibrated on freshly cleaved HOPG (4.6 V).

6.2.4 Human osteoblast initial attachment

Fibronectin adsorption

Nanoflat, nanoconvex and nanoconcave topographies were cleaned using DI water and sterilised with EtOH. After drying in a hood, the nanotopographies were adsorbed with human plasma fibronectin (from Sigma Merck) solution at 5 μg/mL in phosphate-buffered saline (PBS) buffer for 30 min. The solution was then adsorbed onto the surface, and the specimens were dried in a hood.

Cell culture

Human osteoblasts (from Sigma Merck) were cultured on specimens for 3 hours with a 120 μl/sample density. Each specimen were seeded with 600 cells and maintained with DMEM containing 1% penicillin and no FBS.

Fluorescence staining

Before confocal observation, cells were washed with 3×PBS and fixed with 4% formaldehyde diluted in DI water at 4 ˚C for 12 h. After that, 0.1 mL of Triton X was added for 30 min at room temperature. Cells were blocked for nonspecific binding using 1% BSA and incubated at 37 ˚C for 5 min. After blocking, the primary antibody (Anti-Vinculin, mouse from Sigma Merck, UK) was added for 12 h at 4 ˚C. Alexa Fluor 594 Phalloidin, 1:300, (from ThermoFisher, UK), Hoechst 33258, (from ThermoFisher, UK) were applied at room temperature for 1 h. Cells were next washed with 0.5% Tween in PBS (PBST) three times. Then, a biotinylated secondary antibody (mouse, UK) was added and incubated at room temperature for 1 h.

6.2.5 Coulomb force (Electrostatic force) calculation

The Coulomb force was semi-quantified based on KPFM surface potential using

Laplace's equation as listed below.

For comparative analysis of Coulomb's force of areas on nanoconvex and nanoconcave surfaces, the general mathematical solution of the Laplace equation in spherical coordinates r and θ is:

$$\nabla^2\varphi = \frac{1}{r^2}\frac{\partial}{\partial r}\left(r^2\frac{\partial\varphi}{\partial r}\right) + \frac{1}{r^2\,sin\,\theta}\frac{\partial}{\partial\theta}\left(sin\,\theta\frac{\partial\varphi}{\partial\theta}\right) + \frac{1}{r^2\,sin^2\,\theta}\frac{\partial^2\varphi}{\partial\emptyset^2} = 0 \quad \text{Equation 6. 5}$$

$$\varphi(r,\Theta,\Phi) = R(r)\Theta(\theta)\Phi(\phi) \quad \text{Equation 6. 6}$$

Then

$$R(r) = A_n r^n + B_n\frac{1}{r^{n+1}} \quad \text{Equation 6. 7}$$

$$\Phi(\phi) = C_m\,sin(m\varphi) + D_m\,cos(m\varphi) \quad \text{Equation 6. 8}$$

$$\Theta(\theta) = kP_n^m(cos\,\theta) \quad \text{Equation 6. 9}$$

The single Nanoconvex is symmetry by ϕ,

Then ϕ is related with r, θ,

$$\varphi(r,\theta) = \sum_n(a_n r^n + b_n\frac{1}{r^{n+1}})P_n\,(cos\,\theta) \quad \text{Equation 6. 10}$$

Where, $P_n\,(\cos\,\theta)$ is the Legendre equation,

$$P_0(cos\,\theta) = 1, \quad \text{Equation 6. 11}$$

$$P_1(cos\,\theta) = cos\,\theta,$$

$$P_2(cos\,\theta) = \frac{1}{2}(3\,cos^2\,\theta - 1)$$

...

Here, P_0 and P_1 were taken into account for the contribution of $\phi\,(r,\,\Theta)$,

$$\varphi(r,\theta) = a_0 + \frac{b_0}{r} + (a_1 r + \frac{b_1}{r^2})\cos\theta \qquad \text{Equation 6. 12}$$

when $\mathrm{r} = \infty$, $\theta = 0$, $\Phi(\infty, 0) = 0$, then

$$\varphi(r,\theta) = \frac{b_0}{r} + \frac{b_1}{r^2}\cos\theta \qquad \text{Equation 6. 13}$$

where, b_0 and b_1 are undetermined coefficients and can be determined by KPFM.

6.3 Results

6.3.1 Osteoblast viability on Ti, NT and SO-NT surfaces

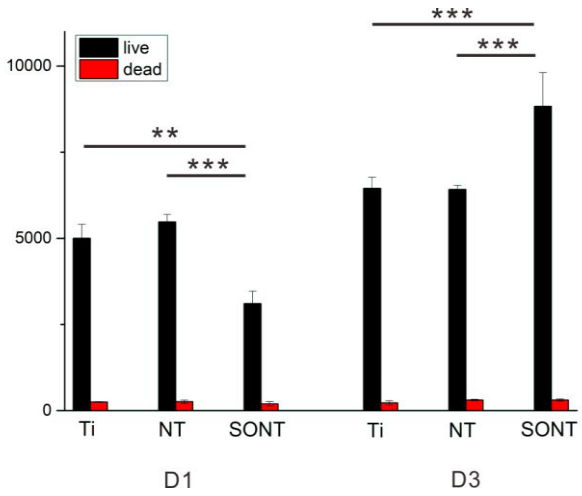

Figure 6. 5 Osteoblast viability on Ti, NT and SO-NT at 24 h and 72 h, y axis is cell counts

As Figure 6. 5 illustrates, the MG63 osteoblasts' viability showed no significant difference between seeding on titanium and NT; however, the cell number on SO-NT significantly decreased after 24 h culture. This reduced cell number may due to two reasons: 1) the cells' media droplets slipped off from the SO-NT surface during the seeding procedure, and 2) the SO-NT caused some cell apoptosis. Meanwhile, from the dead bar value for day 1, the cells initially attached to the SO-NT may be substantially less compared to the other two surfaces. However, the D3 after 72 h cell

viability demonstrated that the SO-NT has significantly higher values than Ti and NT. The microscopic images illustrated that the osteoblasts were spreading more on NT and SO-NT than for Ti (Figure 6. 6). After 24 h seeding (D1), it was observed that the morphology of osteoblasts was spindle shaped on both NT and SO-NT in comparison to Ti—the osteoblasts on Ti were spherically shaped and exhibited obvious elongation after 72 h culturing (see D3 Ti, microscope image). Meanwhile, osteoblasts on NT and SO-NT were further spreading after 72 h.

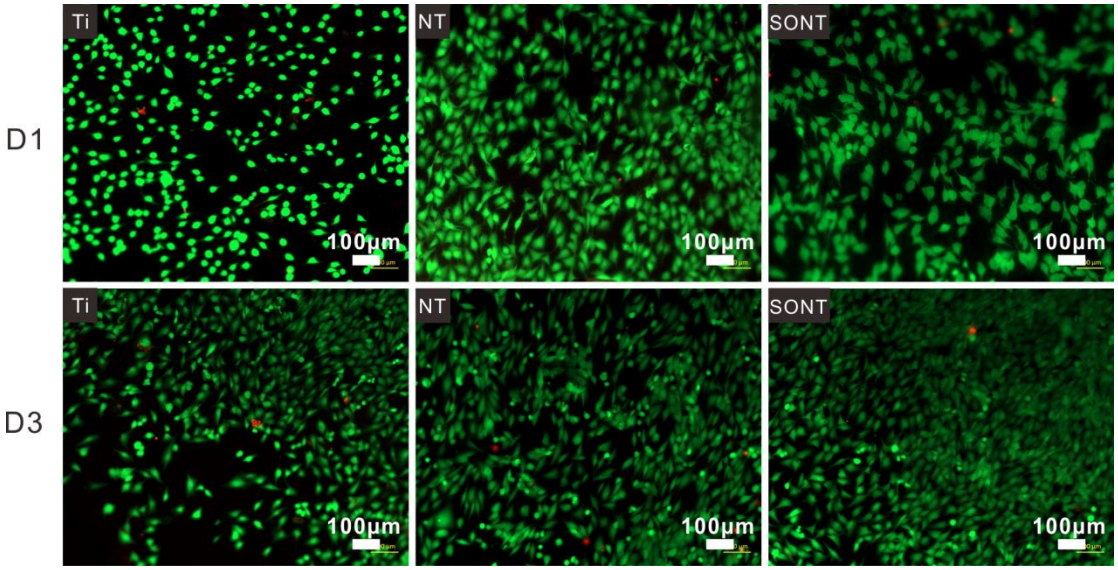

Figure 6. 6 Osteoblast cell morphological characterization of spreading on Ti, NT and SO-NT for 24 h and 72 h

6.3.2 Topography of Nanoflat, Nanoconvex and Nanoconcave

As Figure 6. 7 illustrates, the topographical characterisation of nanoflat, nanoconvex and nanoconcave surfaces. a, Arrangement of nanoflat, nanoconvex and nanoconcave surfaces by SEM, illustrating the nanoscale flat topography of nanoflat, and highly ordered arrangement of subunits on nanoconvex and nanoconcave

surfaces. b, Three-dimensional illustration of nanoflat, nanoconvex and nanoconcave surfaces by AFM tapping mode in a 500×500 nm^2 square area. c, Sectional dimensions of three topographies. d, Based on AFM section measurement, the statistical dimensions of nanoflat (height), each nanoconcave subunit (height and width) and each nanoconcave subunit (height and width). Ten subunits on different regions were analysed. ＊＊＊, $p<0.001$; (n.s., not significant. Error bars represent standard error with the mean (s.e.m). e, Surface area of nanoconvex and nanoconcave surfaces). Nanoconvex and nanoconcave surfaces are seen as spherical domes. f, Schematic illustration of average nanoconvex and nanoconcave dimensions.

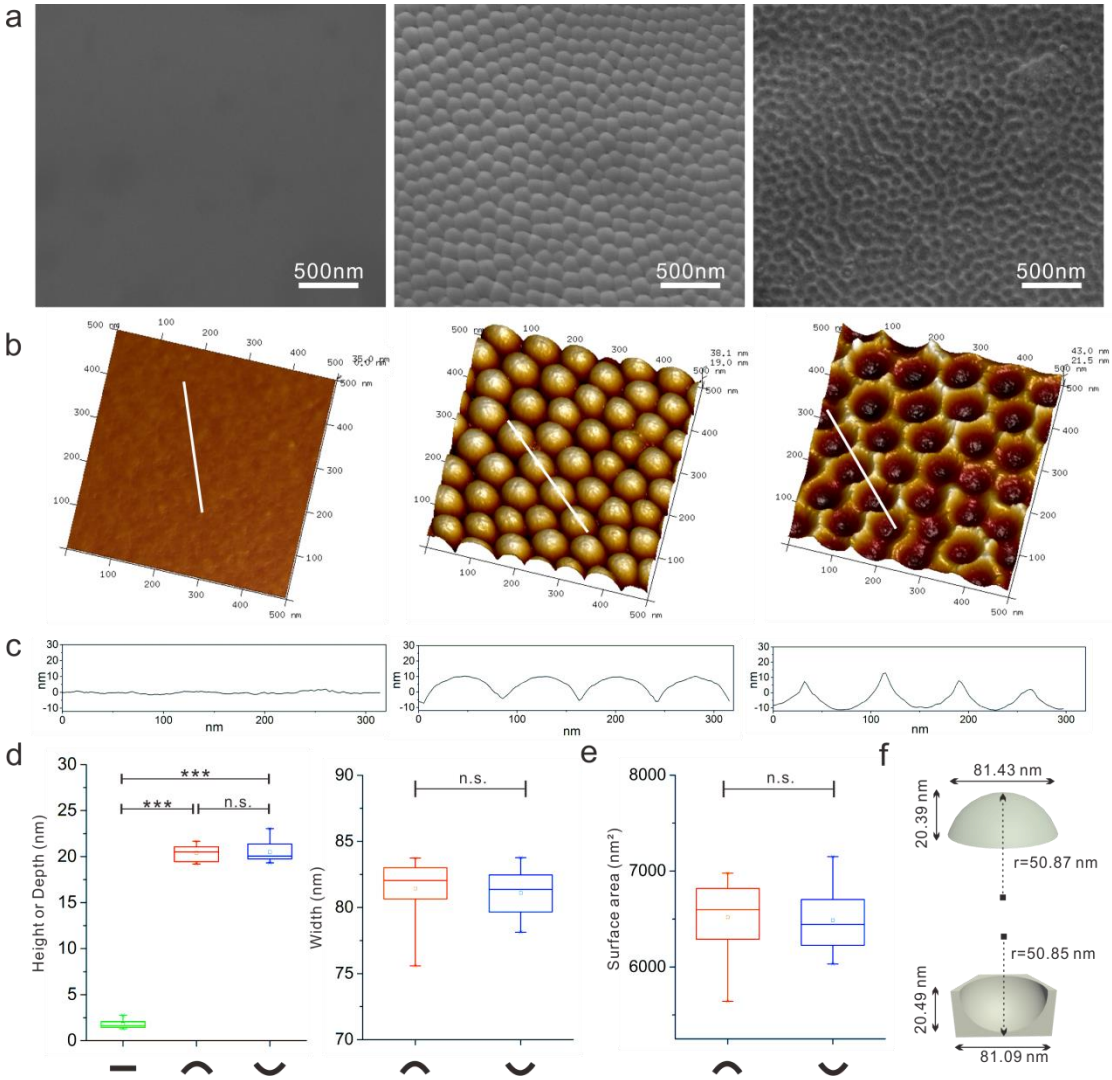

Figure 6. 7 Topographical characterization of Nanoflat, Nanoconvex and Nanoconcave. a, arrangement of nanoflat, nanoconvex and nanoconcave surfaces by SEM. b, Three-dimensional illustration of nanoflat, nanoconvex and nanoconcave surfaces by AFM. c, Sectional dimensions of three topographies. d, Based on AFM section measurement, the statistical dimensions of nanoflat (height), each nanoconcave subunit (height and width) and each nanoconcave subunit (height and width). e, Surface area of nanoconvex and nanoconcave surfaces)

6.3.3 Surface charge distribution of Nanoflat, Nanoconvex and Nanoconcave

Figure 6. 8 illustrates the relative surface potential distribution on nanoflat,

nanoconvex and nanoconcave surfaces. a, AFM topographical characterisation of nanoflat, nanoconvex and nanoconcave surfaces by tapping mode in 1×1 μm^2 square area. b, Surface potential distribution measured by Kelvin probe force microscopy (KPFM) with sample bias model in identical topography 1×1 μm^2 square area. The surface potentials of each topography are highly correlated with the topographical features. With sample bias model, topographical bumps on nanoconvex surfaces are shown bowls curve in potential distribution; nanoconcave surfaces display a constant shape in both topography and surface potential distribution. c, Sectional potential distribution in relative value on nanoflat, nanoconvex and nanoconcave surfaces. d, The absolute potential difference on each subunit of nanoflat, nanoconvex and nanoconcave surfaces. Five subunits on the different surfaces were analysed. ＊＊＊, $p<0.001$; n.s., not significant. Error bars represent standard error compared with the mean (s.e.m). e, Schematic illustration of correlation between topography and surface potential distribution on nanoconvex and nanoconcave surfaces. For each subunit on the nanoconvex surface, top area (A) has higher potential than bottom area (B), A>B; for each subunit on nanoconcave surface, bottom area (A) has higher potential than top area (B) A>B.

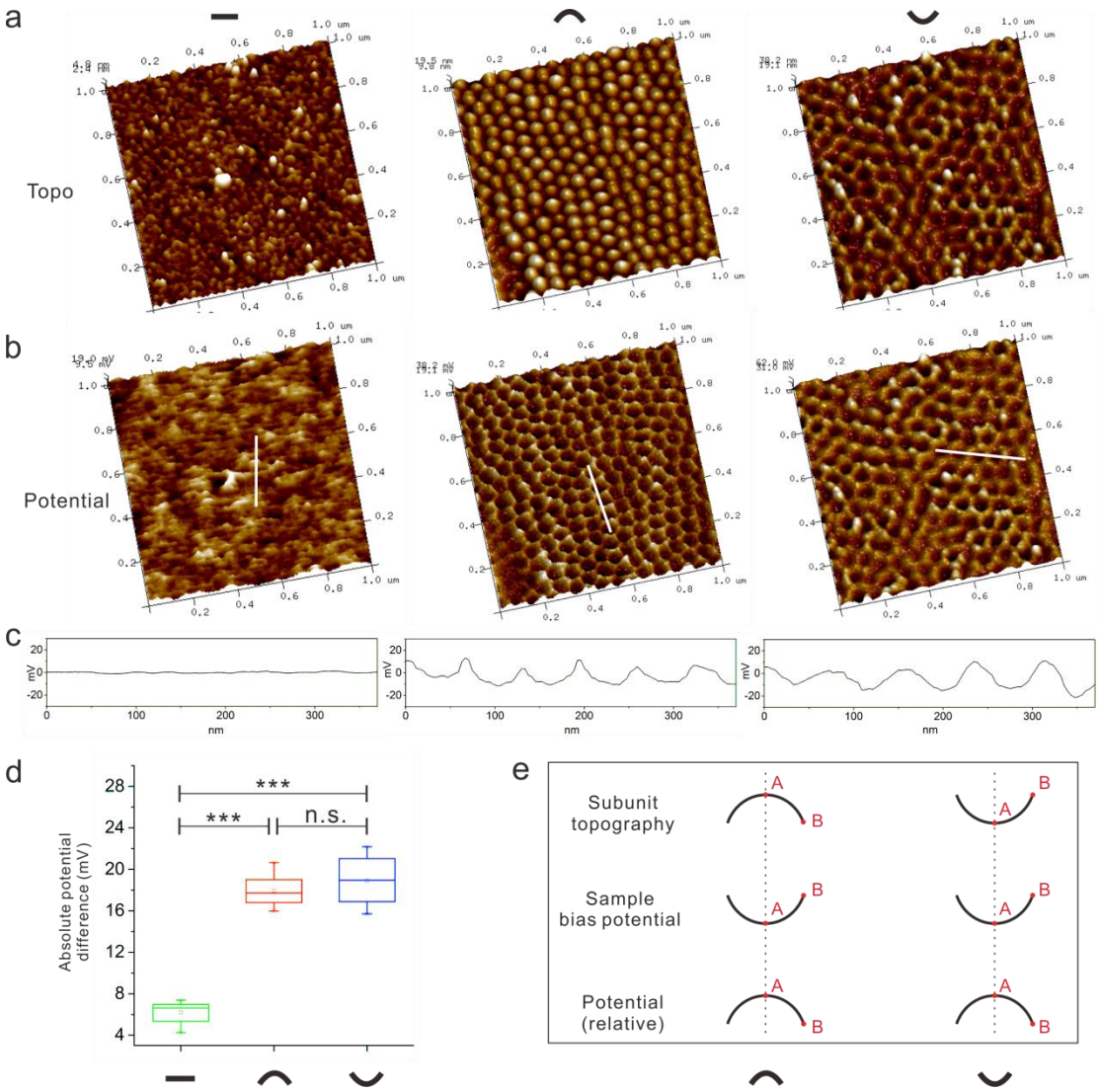

Figure 6. 8 Topographies of Nanoflat, Nanoconvex and Nanoconcave and corresponding surface charge. a, AFM topographical characterisation of nanoflat, nanoconvex and nanoconcave. b, Surface potential distribution measured by Kelvin probe force microscopy (KPFM). c, Sectional potential distribution in relative value on nanoflat, nanoconvex and nanoconcave surfaces. d, The absolute potential difference on each subunit of nanoflat, nanoconvex and nanoconcave surfaces. e, Schematic illustration of correlation between topography and surface potential distribution on nanoconvex and nanoconcave surfaces

Based on the KPFM results and Laplace's equation as illustrated in methods. The surface potential (φ) of Nanoconvex and Nanoconcave can be calculated:

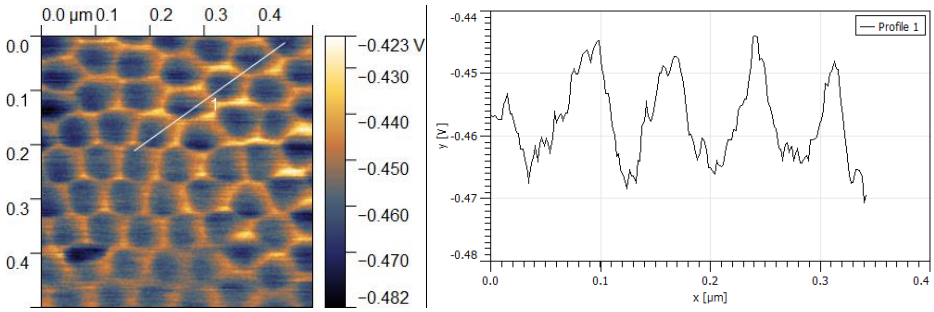

Figure 6. 9 The calibrated with HOPG absolute surface potential value of Nanoconvex

From the KPFM (sample bias) result, the topographical top point A (see Figure 6. 8 e) with coordinates $\mathrm{A}(\mathrm{r}_0, 0)$, $\Phi(\mathrm{A}) = \mathrm{P}_\mathrm{A}$ and topographical bottom point B (see Figure 6. 8 e) with coordinates $\mathrm{B}(\mathrm{r}_0, \arccos 3/5)$, $\Phi(\mathrm{B}) = \mathrm{P}_\mathrm{B}$ have,

$$\varphi(A) - \varphi(B) = 17.94\, mV = 0.018\, V = 0.02V$$

$$\varphi(A) = -460mV = -0.46V$$

$$\varphi(B) = -440mV = -0.44V$$

Then we have,

$$b_1 = 0.05{r_0}^2$$

$$b_0 = 0.51r_0$$

where

$$\varphi(r, \theta) = \frac{-0.51r_0}{r} + \frac{0.05{r_0}^2}{r^2} cos\, \theta \qquad \text{Equation 6. 14}$$

The electric field can be written as follows:

$$E_r = -\frac{\partial \varphi}{\partial r} = \frac{-0.51r_0}{r^2} + \frac{0.1{r_0}^2\, cos\, \theta}{r^3} \qquad \text{Equation 6. 15}$$

$$E_\theta = -\frac{\partial \varphi}{\partial \theta} = sin\, \theta \frac{0.05{r_0}^2}{r^2} \qquad \text{Equation 6. 16}$$

then we have

$$E_A^2 = E_{r_0}^2 + E_0^2 = (\frac{-0.51r_0}{{r_0}^2})^2 + (\frac{0.1}{r_0})^2 + 2\frac{-0.51r_0}{{r_0}^2}\frac{0.1}{r_0} \qquad \text{Equation 6. 17}$$

$$E_B^2 = E_{r_0}^2 + E_{arccos3/5}^2 = (\frac{-0.51r_0}{{r_0}^2})^2 + (\frac{0.06}{r_0})^2 + \frac{0.12\times -0.51r_0}{r_0^3} + 0.0016 \qquad \text{Equation 6. 18}$$

$$E_A^2 - E_B^2 = \frac{0.0064}{{r_0}^2} + \frac{0.08\times -0.51 r_0}{{r_0}^3} - 0.0016 < 0 \qquad \text{Equation 6. 19}$$

Clearly, $\mathrm{E_A^2} < \mathrm{E_B^2}$. Hence, electrons distributed at the nanoconvex surface top (A area, Figure 6. 8 e) have less density than that at $\theta = \arccos 3/5$ area (B), and $\theta = \arccos 3/5$ area can generate more attractive Coulomb forces to charged proteins. However, this equilibrium of electron distribution does not include the introduction of externally charged proteins—electrons are prone to transfer and redistribute, whereas the proteins are induced.

Similarly, the surface potential of nanoconcave surfaces can be calculated using the same method.

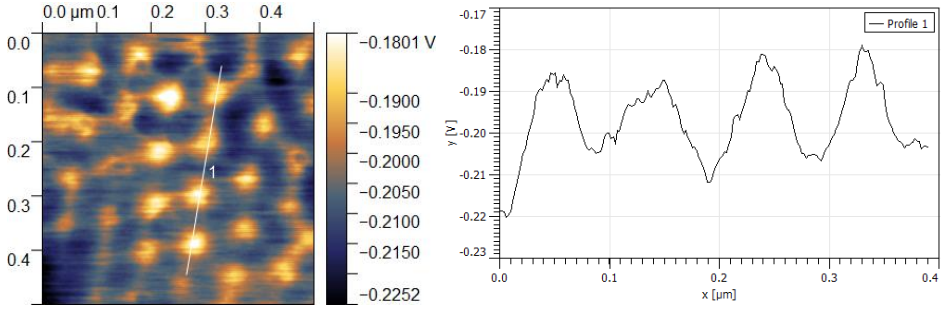

Figure 6. 10 The calibrated with HOPG absolute surface potential value of Nanoconcave

From the KPFM (sample bias) result, the topographical top point A with coordinates $\mathrm{A}(\mathrm{r_0}, \pi)$, $\Phi\,(\mathrm{A}) = \mathrm{P_A}$ and topographical bottom point B with coordinates $\mathrm{B}(\mathrm{r_0}, \pi - \arccos 3/5)$, $\Phi\,(\mathrm{B}) = \mathrm{P_B}$ have,

$$\varphi(A) - \varphi(B) = 18.92\,mV = 0.019\,V = 0.02V$$

$$\varphi(A) = -185mV = -0.19V$$

$$\varphi(B) = -205mV = -0.21V$$

Then we have,

$$b_1 = -0.05{r_0}^2$$

$$b_0 = -0.24r_0$$

where

$$\varphi(r,\theta) = -\frac{0.24r_0}{r} - \frac{0.05{r_0}^2}{r^2}cos\,\theta \qquad \text{Equation 6. 19}$$

The electric field can be written as follows:

$$E_r = -\frac{\partial\varphi}{\partial r} = -\frac{0.24r_0}{r^2} - \frac{0.1{r_0}^2\,cos\,\theta}{r^3} \qquad \text{Equation 6. 20}$$

$$E_\theta = -\frac{\partial\varphi}{\partial\theta} = -sin\,\theta\,\frac{0.05{r_0}^2}{r^2} \qquad \text{Equation 6. 21}$$

then we have

$$E_A^2 = E_{r_0}^2 + E_0^2 = (\frac{-0.24r_0}{{r_0}^2})^2 + (\frac{0.1}{r_0})^2 + 2\frac{-0.24r_0}{{r_0}^2}\frac{0.1}{r_0} \qquad \text{Equation 6. 22}$$

$$E_B^2 = E_{r_0}^2 + E_{\pi-arccos3/5}^2 = (\frac{-0.24r_0}{{r_0}^2})^2 + (\frac{0.06}{r_0})^2 + \frac{-0.24r_0}{{r_0}^2}\frac{0.12}{r_0} + 0.0016 \qquad \text{Equation 6. 23}$$

$$E_A^2 - E_B^2 < 0 \qquad \text{Equation 6. 24}$$

Hence, electrons distributed at the nanoconvex surface top (A area, see Figure 6. 8 e) are of less density than that at $\theta = \pi - \arccos 3/5$ area (B), and the $\theta = \pi - \arccos 3/5$ area can generate more attractive Coulomb forces for charged proteins.

To summarise, the aforementioned calculation can illustrate the surface charge during the initial stage and after protein inducement.

6.3.4 Human osteoblasts initial attachment on Nanoflat, Nanoconvex and Nanoconcave

As the afore-mentioned method illustrated, human osteoblasts were cultured for 3 hours to investigate the initial attachment on nanoflat (control), nanoconvex and nanoconcave surfaces.

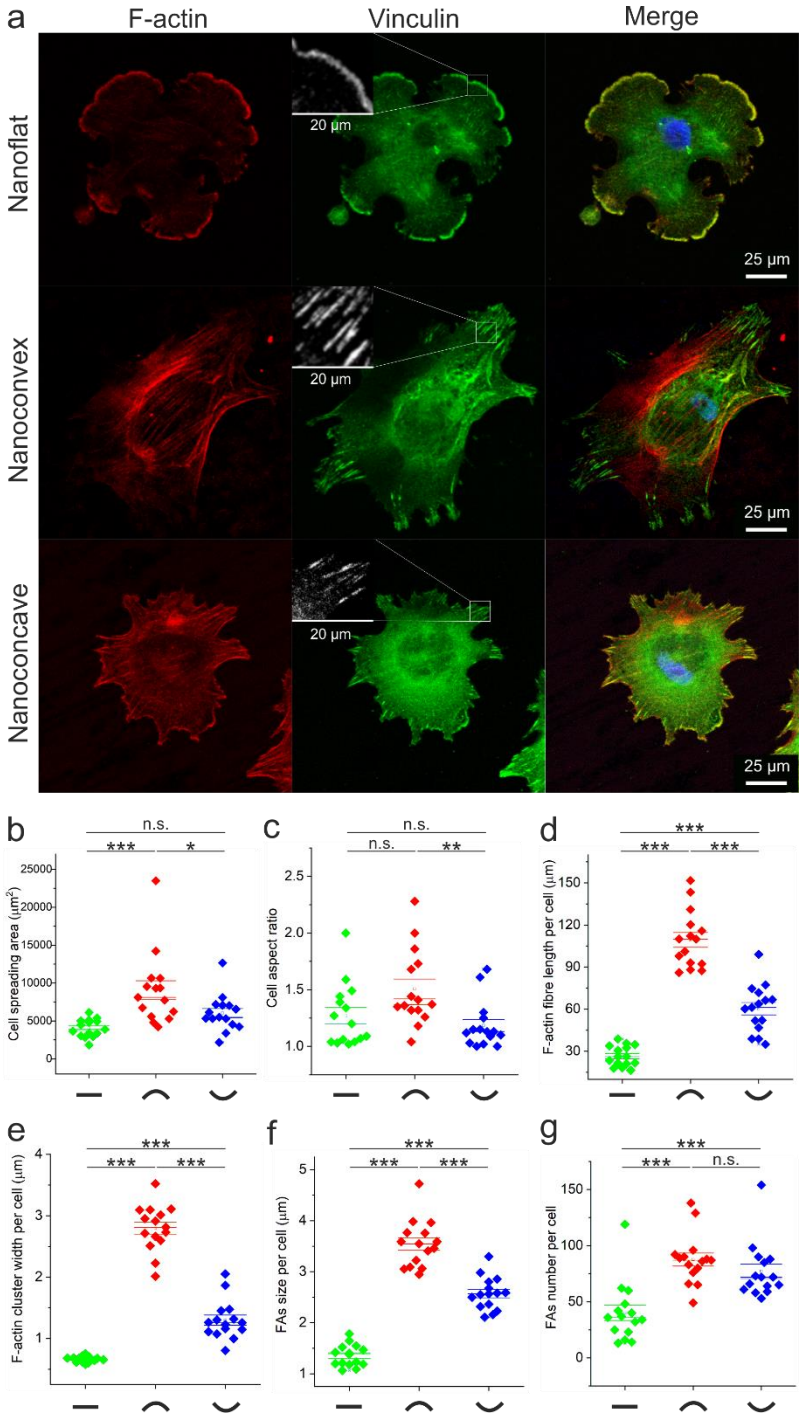

Figure 6. 11 Actin (red), vinculin (green), and cell nucleus (blue) fluorescence images of osteoblasts after culture 3 h. a, cytoskeleton arrangement. b, c, d, e, f and g, cytoskeletal measurements

From the morphological analysis of osteoblasts shown in Figure 6. 11, the cells on nanoflat surfaces had a round or square shape. Although the stress fibres were

obvious and numerous, the arrangement of the actin cytoskeleton was not well organised, with one direction in terms of osteoblast elongation. Ascribed to the short actin fibres, and no fibre was grown that crossed the nuclear region and reached another side, the cell cytoskeleton was more 'spherical' than nanoconvex and nanoconcave. The cytoskeleton arrangement of osteoblasts on nanoconvex surfaces was shown to be well organised; the right image of the nanoconvex surface illustrates that the surface adhesion spots were clearly seen and grown with well-developed stress fibre–actin. The cell has a spindle shape due to the organised, strong and long actin fibres. However, the spreading size of osteoblasts on the nanoconvex surface was smaller than the spreading area on nanoconcave and nanoflat surfaces, indicating a reduced spreading behaviour compared to cells on nanoconcave surfaces. The elongated osteoblasts were observed on nanoconcave surfaces, as the images illustrated, with the osteoblasts being clearly extended. Furthermore, the arrangement of cytoskeleton fibres was in one direction. Human osteoblast responses demonstrated that the cells on nanoconcave surfaces had improved attachment compared to nanoflat and nanoconvex ones. Although the cells displayed spreading behaviour on nanoflat surfaces, the morphology of cells was spherical. Cell morphology is an important aspect of the phenotype of a cell, and it is critical in the regulation of cell activities. The shape of healthy osteoblasts is a spindle, elongated, and with highest adhesion phenotype. Cells on nanoconcave surfaces had an elongated shape and high spreading area. In contrast, osteoblasts on nanoconvex surfaces had a decreased spreading area compared to nanoflat and nanoconcave

topographies. Thus, the nanoconcave surface displays an improvement in terms of cell attachment.

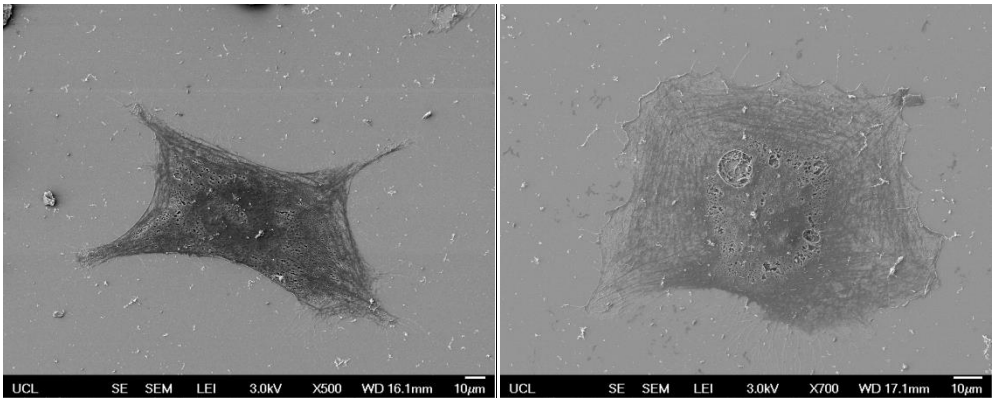

Figure 6. 12 Human osteoblasts initial attachment and spreading on Nanoflat

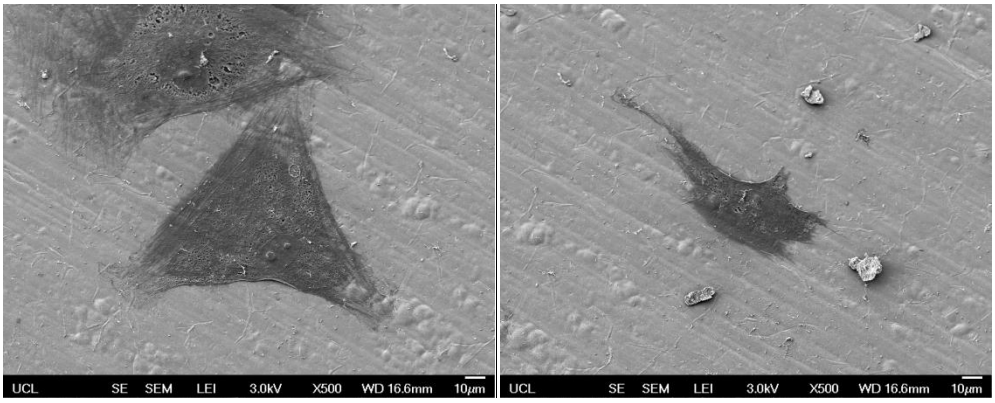

Figure 6. 13 Human osteoblasts initial attachment and spreading on Nanoconvex

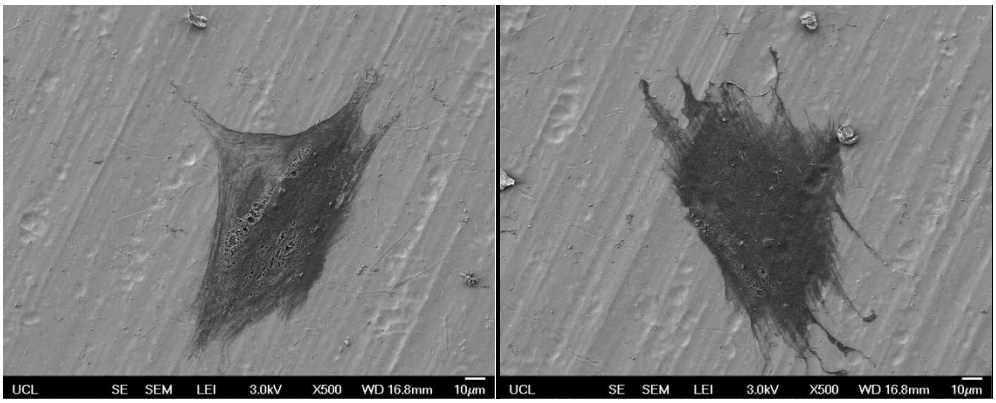

Figure 6. 14 Human osteoblasts initial attachment and spreading on Nanoconcave

Morphological characteristics of human osteoblasts on Nanoflat, Nanoconvex and Nanoconcave were observed by SEM as illustrated in Figure 6. 12 to 14. Compared

with cytoskeleton arrangement observed by confocal microscope, the skeleton measured by SEM has exhibited similar trend.

6.4 Discussion

It is widely known that cellular behaviours are strongly influenced by proteins arranged outside the plasma membrane, such as the ECM. Furthermore, the original distribution of charged proteins (before cell attach or at the moment of cell attachment) is strongly affected by attractions due to the nanotopography, such as Coulomb's force. This is the attractive or repulsive force between oppositely or similarly charged objects. As aforementioned with respect to the theoretical mechanism of attractive forces, the various distribution of electrons can lead to a change in Coulomb's force. However, as aforementioned, methods such as mask anodisation generate nanopillars with inconstant curvature at the top of the pillars. While the charged protein approaches the material surface, the electron is prone to concentrate at sharp/angle areas, leading to nonconstant Coulomb forces. The sharp area produces stronger Coulomb forces than flat areas, whereas the curvature may be more influential than the nano pillar/pit size. This issue could cause similar-dimension nanopillars to display different attractive forces (see Figures 6. 15 and 6. 16).

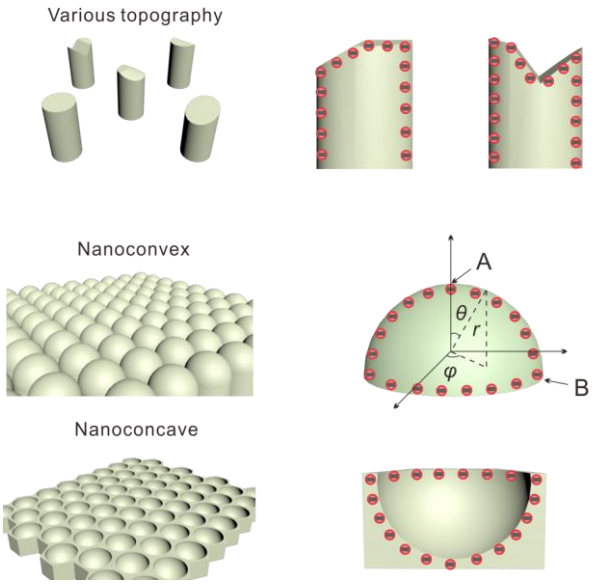

Figure 6. 15 Electron distribution when electrostatic balance on nano pillar/pits, the electron is distributed uniform on surface of material

Due to the inconstant Coulomb attractive forces, the charged proteins can be distributed to various locations on different nanopillars/nanopits. Although the size of nanopillars/nanopits is relatively homogeneous, the attracted ECM may be quite different for each subunit (see Figure 6. 16). The various nanotopographies not only strongly affect cell focal adhesion, but also influence filopodia extension. Filopodia are fine, integrin–containing, cell membrane projections with a tip diameter on the nanoscale, with 8 nm minimum sense.

The advantages of nanoconvex and nanoconcave surfaces include a uniform distribution of electrons because the cation mediated fibronectin is attracted by the electrons on the surface—the electrons will re-distribute, and the re-distributed electrons can also cause a corresponding change in Coulomb's force between the material and fibronectin. Hence, the two attractive parts are involved in dynamic interactions.

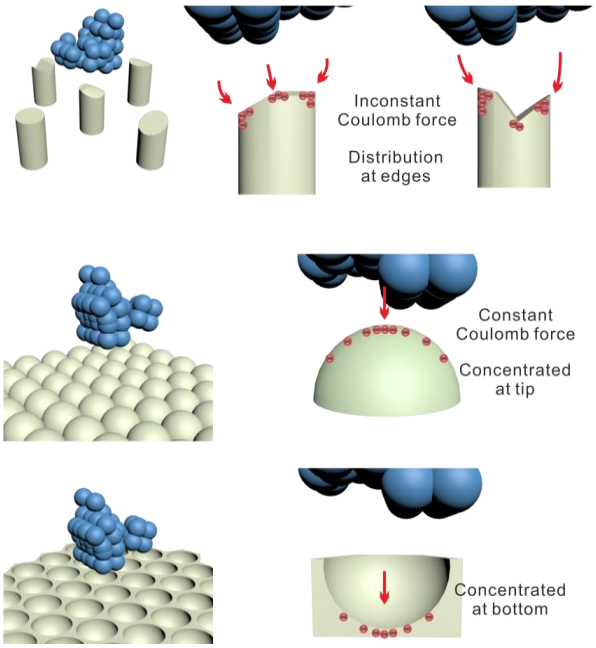

Figure 6. 16 Electron concentrated at the sharp edge on nano pillar/pits while charged protein adsorption when induce external charged protein

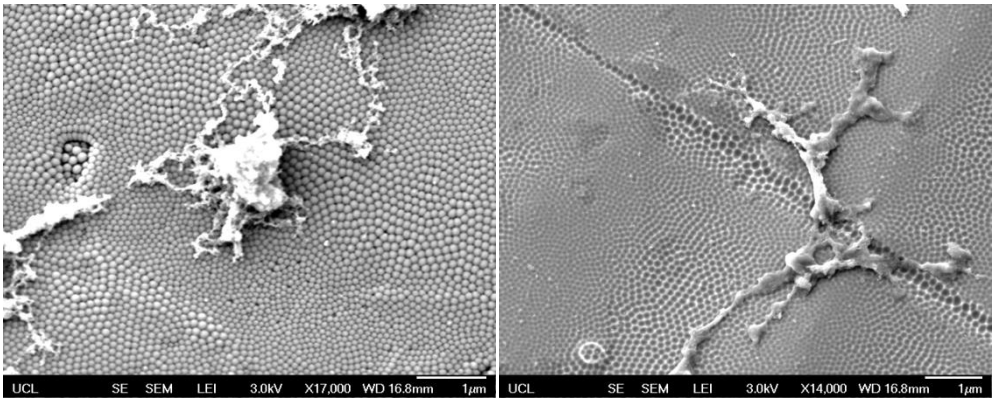

Figure 6. 17 SEM images of fibronectin adsorption on Nanoconvex and Nanoconcave

As aforementioned, fibronectin distribution on materials influences osteoblasts attachment by affecting adhesion arrangement that changes the cytoskeletal tension. Although SEM can directly observe the anchoring fibronectin, the distribution does not accurately reflect in situ distribution, because the interaction determined by surface charge, and the charge affected by the environment applied on material. Moreover, the high vacuum environment of SEM can also influence the fibronectin. Because of

this, the in situ fibronectin adsorption was estimated by simulation method. These corresponding dynamic relations between electrons and fibronectin is illustrated in Figure 6. 18. The left image indicates the electron distribution on each region on a nanoconvex subunit when the fibronectin attracts and moves from 100 nm to 5 nm to the surface of a subunit. For instance, point A is the top of a subunit on a nanoconvex surface (Figure 6. 8), and when the fibronectin moves vertically towards to one subunit on the nanoconvex surface (from A to A'), the electrons are significantly concentrated. Meanwhile, when the fibronectin moves vertically towards the subunit, the electrons are prone to escape from point B. This dynamic causes an extremely high concentration of electrons at region A, leading to a large Coulomb force generation between region A and fibronectin. Hence, the fibronectin was probably adsorbed onto the A region. In contrast, the dynamic of the nanoconcave surface is illustrated in the right image, the electron distribution of region A is opposite to the distribution of region B on the nanoconcave surface subunit. The electrons are mainly distributed at region B when the fibronectin is 100 nm distance from the surface of the concave surface; because the fibronectin is moved from 100 to 5 nm, the electrons tend to redistribute to region A (A') and escapes from region B (B'). Although the electron density of region A' is higher than that of region B', the difference between A' (0.012 c/m^2) and B' (0.0105 c/m^2) is not as significant as the difference for the nanoconvex surface. Hence, the electrons on the nanoconcave surface are redistributed more 'uniformly' than on the nanoconvex surface. The difference of A' (0.13 c/m^2) and B' (<0.001 c/m^2) on the nanoconvex surface can be as high as 0.13

c/m^2. The homogeneously distributed electrons can cause a mild and uniform Coulomb force generation; the fibronectin may be adsorbed onto each region on the nanoconcave surface, resulting in a more uniform distribution of fibronectin on the nanoconcave topography.

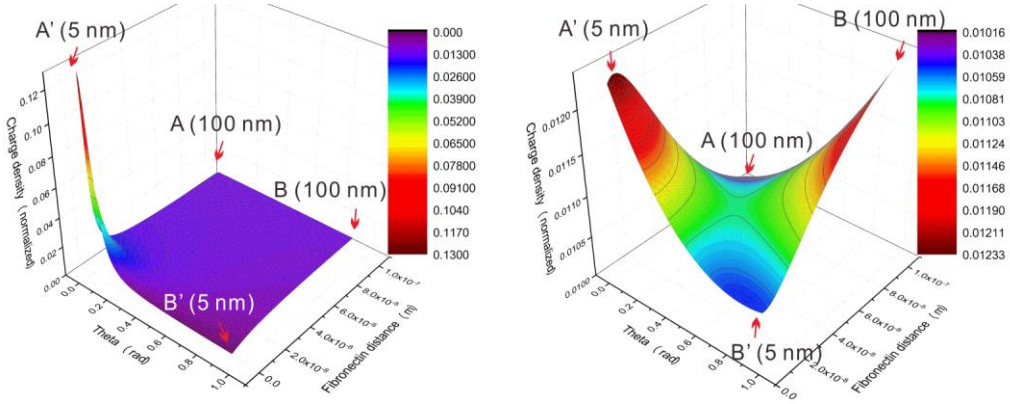

Figure 6. 18 Dynamic of surface charge density of different areas while fibronectin vertically moves to a subunit on Nanoconvex (left) and Nanoconcave (right)

The dynamics of electron motion in each subunit on nanoconvex and nanoconcave surfaces is also illustrated in Figure 6. 19. The electrons' migration is clearly from bottom (B) to top (A) on the nanoconvex surface, leading to the electrons becoming extremely concentrated at top region. The concentrated electrons generate a high Coulomb force, which increases the possibility of attracting fibronectin to this region. Although one hypothesis of the dynamic model is that the fibronectin is above the subunit at different locations, the distribution of electrons on the material surface may also be valuable for reference to other located fibronectins. Due to the Coulomb's attraction, on the top region (A) the nanoconvex surface is 100 folds more than the bottom region (B), and almost all fibronectins are possibly attracted at A. However, due to the quadrupolar charge of fibronectin, the minimum distance between

fibronectins could be several nm, leading to each convex subunit having a 'maximum' load of fibronectins, and these attracted fibronectins are rather concentrated at the top area (A). Although the bottom region on a subunit on a concave surface is also featured with concentrated electrons; the difference between top (B, 0.0105 c/m^2) and bottom (A, 0.012 c/m^2) areas is quite limited, leading to the possibility of fibronectin-attraction areas being almost equal.

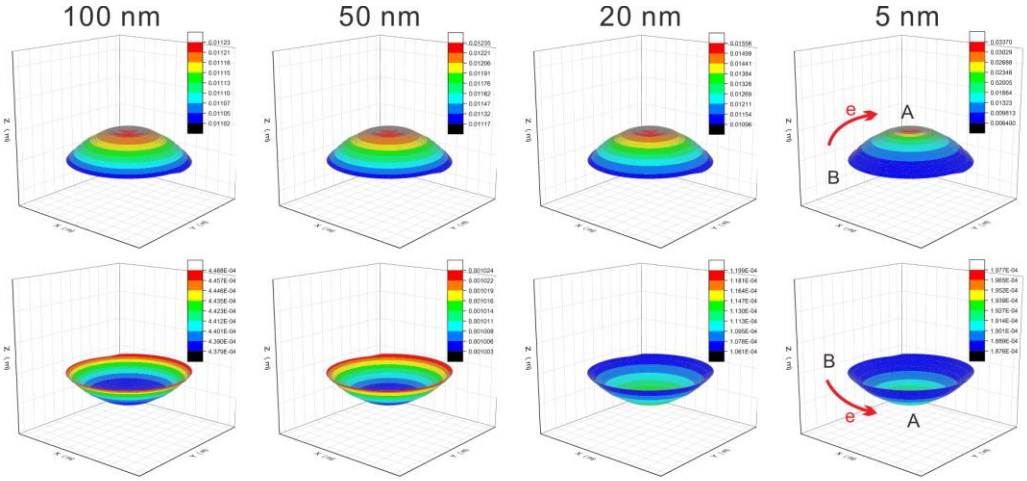

Figure 6. 19 Dynamic of surface charge on one subunit while fibronectin vertically moves to surface on Nanoconvex and Nanoconcave

To illustrate the two different fibronectin distributions, please see Figure 6. 20; the different attraction mechanisms cause the varying cellular responses through different fibronectin behaviours on convex and concave surfaces.

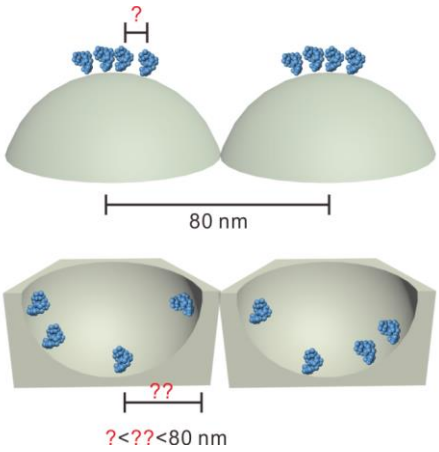

Figure 6. 20 The possibly fibronectin distribution on Nanoconvex and Nanoconcave

6.5 Conclusion

Cellular material interactions are still largely unknown. It has been well documented that material topography can influence cellular behaviours. From the osteoblast responses to Ti, NT and SO-NT, improved attachment was observed on NT and SO-NT. Furthermore, fibronectin adsorption on nano-featured materials was estimated by human osteoblasts' initial attachment, and the dynamics of the Coulomb force mechanism was illustrated by simulation. It was concluded that the Coulomb force of nanoconvex surfaces was concentrated at the top region, leading to a strong attraction, whereas the Coulomb force of nanoconcave surfaces was mild and distributed more uniformly, which may explain the different levels of initial cell attachment.

Chapter 7

7. Conclusion and Future work

The success of orthopaedic implant is strongly depends on the proper integration of bone to biomaterial surface. From retrieval cases study, it is demonstrated that the bone screws integration is a dominated factor leading to implant failure. In order to achieve bone-implant integration, a titanium oxide nanotubes layer was induced to titanium substrate to enhance its osteointegration. Although the cell responses to NT are positive, the weak mechanical bonding of NT layer to substrate has been well documented and became an obstacle to its applications. In order to achieve better mechanical bonding, SO-NT modified titanium was fabricated and characterized systematically in this study. The SO-NT modified titanium has demonstrated with an improved biotribological and biocorrosive performance. Although both NT and SO-NT have proven the promotion of osteoblasts attachment. However, the mechanism of cell nanotubes interactions are still unclear. Therefore, Nanoconvex, Nanoconcave and Nanoflat nanotopographies were fabricated for investigating cell-nanomaterial interactions. The preliminary study of human osteoblast initial attachment on Nanoflat, Nanoconvex and Nanoconcave topographies demonstrated the Nanoconcave can improve cell attachment. As the cell morphology on it displayed spindle shape, the cells on Nanoflat were well-spreading but with sphere shape, while cells on Nanoconvex has proven to be the minimum spreading areas. A model of fibronectin

adsorption on Nanoconvex, Nanoconcave and Nanoflat was proposed to describe the protein-material interact mechanism. The Coulomb's force on these topographies were comparatively quantified by this theoretical calculation model. It was found the fibronectin could distribute uniformly on Nanoconcave that may contributed to improve cells attachment. By contrast, the fibronectin was agglomerated on Nanoconvex top area, and resulted in a reduced cells attachment. This model, combined with experimental results, could be well exploited in study cell-material interactions.

7. 1 Osteointegration and TiO_2 nanotubes

Different with the creation micro featured roughness on implants, the nano featured topographical implant has attracted much attention, as the surface microtopography effectively influences osteoblast behaviors in terms of differentiation and proliferation, and the expression of differentiation markers and the local production of growth factors and cytokines [177]. Cell adhesion is one of the initial stages for subsequent proliferation and differentiation of osteoblastic cells producing bone tissue. It has been well documented that osteoblasts cell adhesion, growth and differentiation are related to surface energy and roughness [178, 179]. Furthermore, osteoblasts adhesion at bone implant interface is affected by surface charactors of materials properties according to local mesoscale, microscale and nanoscale topographical patterns, charge distribution and chemistry features. Cells are inherently sensitive to their surroundings, and respond to environment features at all length scales from macro down to the molecular. Typical cell membrane is covered by specific carbohydrate structures and

at least six different receptor systems that can be activated by interactions with adjacent cells, ligands in the surrounding ECM and signaling molecules. Moreover, hundreds of proteins involve in the composite stimulation of cell receptors [160]. For instance, the ECM plays a major role in regulating growth factor signaling, acting as a local reservoir for latent forms, and rapidly releasing and activating them on demand [180]. One important assumption is the attraction between the negatively charged titanium surface and a negatively charged osteoblast is mediated by charged proteins with a distinctive quadrupolar internal charge distribution. Thus, a high surface charge density leads to more efficient for cation-mediated attraction between fibronectin molecules and the titanium surface [59]. Moreover, it was documented the osteoblast morphology in the smallest nanorough region was rounder and has less diffuse F-actin filaments, while filopods extending from cells remained near their origin [181].

Recently, the titanium implants surface was modified by a self-assembled layer of vertically oriented NT, with diameters between 15 nm and 100 nm. NT exhibited with increased roughness than bare titanium surface. Furthermore, It was shown that adhesion, spreading, growth, and differentiation of cells on nanotube surfaces depend on the diameter of the nanotubes [57]. The nanotube with diameter of 15 nm seemed to be more appropriate for differentiation of mesenchymal, endothelial, and smooth muscle cells in comparison to 70–100 nm nanotubes and to amorphous (smooth) TiO_2 surfaces [85]. However, other researchers reported converse results with hMSCs culturing that the small nanotubes with 30 nm diameter size promoted adhesion without noticeable differentiation, whereas the larger nanotubes, 70–100 nm in

diameter elicited a dramatic stem cell elongation (10 fold increased), which induced cytoskeletal stress and selective differentiation into osteoblasts-like cells [55].

The above mentioned NT findings are valid generally for the cell response to different topographical nanorough surfaces, and could in future have an important impact on the design and composition of implant surfaces [16]. Therefore, these findings must be connected to the increased strength of attractive interactions per unit area in nanorough implant surfaces. However, the experimental investigation of cell nanomaterial interface with unknowing dynamic and mechanisms, down to molecular is difficult to achieve. The question of how cells detect and respond to the nanofeatured topography on implant surface is still largely unsolved [160].

Among many nanotopography created by researchers, the NT attracted much attention due to its feasible fabrication by anodization and great improves osteointegration. Furthermore, the nanotube structure can mimic the natural bone embeded mineral crystals which is designed and assembled in nanoscales building blocks [36]. In addition, the three dimensional nanotubes structure can be bio-functioned used as templates/media to load antibiotics at the site of implantation for in-situ drug delivery at bone implant interface, and can also enhance osteoblast differentiation when tubes filled with gentamicin [41]. However, there are still many unsolved problems of NT from the clinical usage in orthopaedic implants, it has been documented the drawback of NT layer is the poor interfacial adhesion between tubes layer and Ti substrate that TiO_2 nanostructure are prone to peel off [68, 90, 91]. Due to the fabrication process of NT, the nanotubes are 'growth' from the titanium substrate. The

external energy is quite limited (only the voltage applied), the fabrication process is 'mild and control' electrochemistry reactions, both the reasons leads to the adhesion strength of nanotubes layer is weak. However, what if increase the voltage applied to accelerate electrochemical procedure, the ions transferring would become intense, leads to generate disordered TiO_2 thick layer without any nanotubes. The paradoxical problem between ordering structure and adhesion strength is exist due to the fabrication method of NT. Compared with plasma spray coating, especially thermo spraying, the high speed jet (800 m/s) combined with high temperature (14000 K) can spray powder with super high energy to adhesion on substrate. Under the massive energy, each molten droplet splats onto the surface, forming a pancake-like structure that rapidly solidifies. Because of the fabrication process, plasma spray method can generate super strong adhesive strength coating. Although plasma spray method can greatly improve the wear resistance of substrate, the method of plasma spray is impossible to control the nano structure of coating. Thus, no coating technology can perfectly combined ordering nano structure and super strong mechanical stability. In substantial, the precise nano structure fabrication depends on mild and controlled chemical/physical procedure (anodization), and the strong mechanical stability coating needs to generated by intense external energy (thermo/kinetic) inducement. This leads to the coating with highly ordering nano structure and strong mechanical stability can never be generated.

Orthopaedic implants materials are required to be with improved osteointegration, with cell instructive functional and high wear resistance. Beside the requirements of

cell microenvironment aforementioned, the shear and external stress can be the mechanical decisive factors in terms of implants coating application. It is important to balance each property and improve both performance of the materials.

7. 2 Biotribological and biocorrosive improvement of SO-NT

As the bare study or report of biotribology behavior of NT, the degrade mechanism of NT under shear is still unknown. Although the friction at bone implant interface is mild, the constant friction may also break the NT and trapped at adjacent bone tissue. Wear debris released in around bone tissue under mechanical removal resulting inflammatory reactions which could cause implants failure [92, 93]. In the thesis, a method by multi anodization steps were carried out to create an interfacial bonding layer that improved mechanical behaviour of NT. According to the bonding layer was strongly bonded bottom of nanotubes and titanium substrate, and the hyper fine grains in bonding layer dissipated the external stress. For example, volume loss of SO-NT growth on pure titanium sheet decreased 85% than that of conversional NT. Moreover, the corrosion resistance of SO-NT were also enhanced because the presence of bonding layer. Compared with the method applied on titanium, SO-NT on Ti_6Al_4V exhibited more enhancement both mechanical stability and corrosion resistance. As the bonding layer 'sealed' the micro pits generated by first anodization step on Ti_6Al_4V alloy substrate, the 'sealed' SO-NT displayed significant improvement. Apart from the properties that improved, another one obvious advantage is SO-NT have maintained the conversional NT topography. As aforementioned in Chapter four,

the contradiction between highly ordered nano topography and strong mechanical stability have been well balanced. The SO-NT is featured with highly arrangement of nano structure, and with excellent mechanical performance. The balance depends on separated anodization to multiple steps. Anodization process in fluorine contained electrolyte generates ordered arrangement of nanotubes on titanium, anodization in phosphate generates hyperfine bonding layer. Moreover, each of anodization step needs to be controlled the ions transfer rate which determined by parameters as voltage, electrolyte concentration and temperature.

Furthermore, the procedure of SO-NT fabrication is simple, without any extra facility involves. The other main advantage of SO-NT fabrication is the method can also applied on different shape titanium based implants, a facile method with widely orthopaedic implants applications.

To summarize, SO-NT technology has further potential applicability in orthopaedic implants, not only retains biological advantages of conversional NT, but also greatly improved the defects of NT.

7. 3 Cell-nanomaterials interactions

Apart from the mechanical weakness of NT, another main limitation of NT is the controversy of MSC responses to different size NT. Although cell nanomaterials interactions were widely researched, the mechanisms of ECM adsorption to material and ECM cell membrane were largely unknown. Due to studies by molecular dynamic simulation, the electrostatic force, Coulomb's force plays dominate role in proteins

attraction. In the thesis, we generated Nanoflat, Nanoconvex and Nanoconcave to investigate the cell initial attachment on these nanotopographies. It has widely known the material can affect cell behaviours from mechanical properties, chemical composition and surface topography. Nanoflat, Nanoconvex and Nanoconcave were designed and fabricated with identical chemical composition and mechanical properties. Meanwhile, due to the composition is TiO_2, the responses of cells are more valuable to implant surface technique, compared to culture cells on silicon and other materials. From the results, the cell morphological analysis has shown human osteoblasts on Nanoconcave were featured with elongated shape and high spreading area, whereas the osteoblasts on Nanoconvex has decreased spreading area than that on Nanoflat and Nanoconcave. It was observed the stress fiber in cells on Nanoflat were short and arranged with various direction, indicates the mechanotransduction of cell was also influenced by focal adhesion. It can speculate that due to the weak Coulomb's force produced by Nanoflat topography, it is impossible to 'anchor' the fibronectin, the unstable fibronectin can be sensed by linked integrin and influence the cytoskeleton formation. The KPFM measurement has demonstrated the absolute potential difference of Nanoflat was only 6 mV, whereas the value of Nanoconcave and Nanoconvex were around 18-20 mV. The threshold of Coulomb's force to 'Anchor' fibronectin is one of the preconditions to improve cell initial attachment, another important precondition is the 'proper' arrangement of fibronectin. This could be speculated by the comparison cell response between Nanoconvex and Nanoconcave. As the simulation model has proved, the Coulomb's

force generated on convex was much higher than that on concave, and the top region can generate extremely high force. However, the increased attraction has not improve the cell attachment as the spreading area of osteoblasts were smaller than area on Nanoconcave. Indicates the adsorpted fibronectin arrangement also affected cell attachment. Ascribed to the different Coulomb's generated on Nanoconvex and Nanoconcave, the fibronectin adsorption were different, the fibronectin on Nanoconcave was distributed more uniform, whereas the distribution on Nanoconvex was concentrated at top region (illustrated in Chapter six). The fibronectin distribution on Nanoconcave was more homogenous as the Coulomb's force generated was uniform. The fibronectin distribution could be another dominate factor to influence cells response. Based on the experiments, the Nanoconcave topography exhibited the well initial attachment, with largest cell spreading and well organized cytoskeleton arrangement, and the mechanisms are illustrated aforementioned.

7. 4 Future work

One of limitations is the lack of wide comparison for mechanical of NT and SO-NT on various implants surface. For example, orthopaedic devices can be divided into two categories, include trauma fixation systems and artificial joint replacements. Although both categories implants present mechanical issues at interface, the conditions and characters are huge different. Various load, torque, shear applied on different implants generates various mechanical conditions. In the thesis, only the interface of screw was discussed. Further, the fretting of bone implant interface is featured with low

frequency (1 Hz), and long term for decades. Due to the time limitation, screw fretting experiments were setup with higher frequency (10 Hz) and short term (60 min). Only mild damage was observed on each sample. However, if the prolong procedure, thermo can be generated by fretting may heat the bone that affect the mechanical behavior because of high frequency.

Furthermore, the degradation of implant at interface is a combination of mechanical, chemical and biological degradation. In the thesis, we mainly focus on mechanical simulation, however, the truly environment is more complex. Tissue fluid around implants is also corrosive to implant surface and refreshable by metabolism, and the pH also changes by tissue responses. Moreover, the other dominated factor is immunological response, involves proteins, cells, enzymes response from biological perspective and organs, lymph, bone marrow and blood response from medical perspective. All factors play roles and influence the implant environment. Therefore, a multi-functional bioreactor is necessary to setup, to systematically evaluate the implant behaviors in vivo.

Another limitation is the impossible measurement of the *in-situ* cell material interactions, such as the fibronectin *in-situ* distribution at ECM-material interface. The *in-situ* distribution can be only estimated (simulated) by theoretical calculation, and because of this, we developed a model to evaluate the interactions. The surface charge of material could be various changed under different environment, however, it is impossible to test surface charge while specimens immersed in liquid. Furthermore, the adsorpted fibronectin may displaced after dried specimens, leads to the

unknowing locations of *in-situ* fibronectin adsorption. Although these technical issues create barriers to observe ECM-material interface, we proposed a novel model to illustrate the fibronectin attraction on nanotopographies by calculate Coulomb' s force. Although we pointed out that the homogenous arrangement of fibronectin can improve the osteoblast attachment, the optimized fibronectin arrangement is still unknown. Thus, the further research of investigate fibronectin arrangement is needed to further reveal the ECM-material interface, and based on that, a nanotopography featured surface implant can be manufactured and release into orthopaedic market.

Reference

1. Kurtz, S.; Ong, K.; Lau, E.; Mowat, F.; Halpern, M., Projections of primary and revision hip and knee arthroplasty in the United States from 2005 to 2030. *J Bone Joint Surg Am* 2007, 89A, 780-785.
2. GlobalData Global Orthopedics Market: 2017 Review. https://www.medicaldevice-network.com/comment/global-orthopedics-market-2017-review/
3. Elias, C. N.; Lima, J. H. C.; Valiev, R.; Meyers, M. A., Biomedical applications of titanium and its alloys. *Jom-Us* 2008, 60, 46-49.
4. Yao, C.; Slamovich, E. B.; Webster, T. J., Enhanced osteoblast functions on anodized titanium with nanotube-like structures. *J Biomed Mater Res A* 2008, 85A, 157-166.
5. Niinomi, M., Mechanical properties of biomedical titanium alloys. *Mat Sci Eng a-Struct* 1998, 243, 231-236.
6. Feng, B.; Weng, J.; Yang, B. C.; Qu, S. X.; Zhang, X. D., Characterization of surface oxide films on titanium and adhesion of osteoblast. *Biomaterials* 2003, 24, 4663-4670.
7. Park, I. S.; Woo, T. G.; Jeon, W. Y.; Park, H. H.; Lee, M. H.; Bae, T. S.; Seol, K. W., Surface characteristics of titanium anodized in the four different types of electrolyte. *Electrochim Acta* 2007, 53, 863-870.
8. Oh, S.; Daraio, C.; Chen, L. H.; Pisanic, T. R.; Finones, R. R.; Jin, S., Significantly accelerated osteoblast cell growth on aligned TiO2 nanotubes. *J Biomed Mater Res A* 2006, 78A, 97-103.
9. Salata, O., Applications of nanoparticles in biology and medicine. *Journal of nanobiotechnology* 2004, 2, 3.
10. Lundborg, G.; Skalak, R.; Branemark, P. I.; Heinegard, D.; Maloney, W.; Hansson, T., Osseointegration in skeletal reconstruction and joint replacement - General discussion. *Osseointegration In Skeletal Reconstruction And Joint Replacement* 1997, 215-225.
11. Branemark, R.; Branemark, P. I.; Rydevik, B.; Myers, R. R., Osseointegration in skeletal reconstruction and rehabilitation: A review. *J Rehabil Res Dev* 2001, 38, 175-181.
12. Mavrogenis, A. F.; Dimitriou, R.; Parvizi, J.; Babis, G. C., Biology of implant osseointegration. *J Musculoskel Neuron* 2009, 9, 61-71.
13. Meyer, U.; Joos, U.; Mythili, J.; Stamm, T.; Hohoff, A.; Fillies, T.; Stratmann, U.; Wiesmann, H. P., Ultrastructural characterization of the implant/bone interface of immediately loaded dental implants. *Biomaterials* 2004, 25, 1959-1967.
14. Berglundh, T.; Abrahamsson, I.; Lang, N. P.; Lindhe, J., De novo alveolar bone formation adjacent to endosseous implants - A model study in the dog. *Clin Oral Implan Res* 2003, 14, 251-262.

15. Murai, K.; Takeshita, F.; Ayukawa, Y.; Kiyoshima, T.; Suetsugu, T.; Tanaka, T., Light and electron microscopic studies of bone-titanium interface in the tibiae of young and mature rats. *J Biomed Mater Res* 1996, 30, 523-533.
16. Franchi, M.; Fini, M.; Martini, D.; Orsini, E.; Leonardi, L.; Ruggeri, A.; Giavaresi, G.; Ottani, V., Biological fixation of endosseous implants. *Micron* 2005, 36, 665-671.
17. Probst, A.; Spiegel, H. U., Cellular mechanisms of bone repair. *J Invest Surg* 1997, 10, 77-86.
18. Giori, N. J.; Ryd, L.; Carter, D. R., Mechanical Influences on Tissue Differentiation at Bone-Cement Interfaces. *J Arthroplasty* 1995, 10, 514-522.
19. Gulati, K.; Ramakrishnan, S.; Aw, M. S.; Atkins, G. J.; Findlay, D. M.; Losic, D., Biocompatible polymer coating of titania nanotube arrays for improved drug elution and osteoblast adhesion. *Acta Biomater* 2012, 8, 449-456.
20. Escada, A. L. A.; Machado, J. P. B.; Schneider, S. G.; Rezende, M. C. R. A.; Claro, A. P. R. A., Biomimetic calcium phosphate coating on Ti-7.5Mo alloy for dental application. *J Mater Sci-Mater M* 2011, 22, 2457-2465.
21. Li, L. H.; Kong, Y. M.; Kim, H. W.; Kim, Y. W.; Kim, H. E.; Heo, S. J.; Koak, J. Y., Improved biological performance of Ti implants due to surface modification by micro-arc oxidation. *Biomaterials* 2004, 25, 2867-2875.
22. Fielding, G. A.; Roy, M.; Bandyopadhyay, A.; Bose, S., Antibacterial and biological characteristics of silver containing and strontium doped plasma sprayed hydroxyapatite coatings. *Acta Biomater* 2012, 8, 3144-3152.
23. Kazemzadeh-Narbat, M.; Noordin, S.; Masri, B. A.; Garbuz, D. S.; Duncan, C. P.; Hancock, R. E.; Wang, R., Drug release and bone growth studies of antimicrobial peptide-loaded calcium phosphate coating on titanium. *Journal of biomedical materials research. Part B, Applied biomaterials* 2012, 100, 1344-52.
24. Klein, C. P. A. T.; Wolke, J. G. C.; Deblieckhogervorst, J. M. A.; Degroot, K., Features Of Calcium-Phosphate Plasma-Sprayed Coatings - an In-Vitro Study. *J Biomed Mater Res* 1994, 28, 961-967.
25. Gross, K. A.; Berndt, C. C., In-Vitro Testing Of Plasma-Sprayed Hydroxyapatite Coatings. *J Mater Sci-Mater M* 1994, 5, 219-224.
26. Hayashi, K.; Inadome, T.; Mashima, T.; Sugioka, Y., Comparison Of Bone-Implant Interface Shear-Strength Of Solid Hydroxyapatite And Hydroxyapatite-Coated Titanium Implants. *J Biomed Mater Res* 1993, 27, 557-563.
27. Faghihi-Sani, M. A.; Arbabi, A.; Mehdinezhad-Roshana, A., Crystallization of hydroxyapatite during hydrothermal treatment on amorphous calcium phosphate layer coated by PEO technique. *Ceram Int* 2013, 39, 1793-1798.
28. Dzhurinskiy, D.; Gao, Y.; Yeung, W. K.; Strumban, E.; Leshchinsky, V.; Chu, P. J.; Matthews, A.; Yerokhin, A.; Maev, R. G., Characterization and corrosion evaluation of TiO2:n-HA coatings on titanium alloy formed by plasma electrolytic oxidation. *Surf Coat Tech* 2015, 269, 258-265.
29. Harrison, N.; Field, J. R.; Quondamatteo, F.; Curtin, W.; McHugh, P. E.; Mc Donnell, P., Preclinical trial of a novel surface architecture for improved primary fixation of cementless orthopaedic implants. *Clin Biomech* 2014, 29, 861-868.

30. Huang, Y.; Zha, G. Y.; Luo, Q. J.; Zhang, J. X.; Zhang, F.; Li, X. H.; Zhao, S. F.; Zhu, W. P.; Li, X. D., The construction of hierarchical structure on Ti substrate with superior osteogenic activity and intrinsic antibacterial capability. *Scientific reports* 2014, 4.
31. Dalby, M. J.; Gadegaard, N.; Oreffo, R. O., Harnessing nanotopography and integrin–matrix interactions to influence stem cell fate. *Nat Mater* 2014, 13, 558.
32. Swami, N.; Cui, Z. W.; Nair, L. S., Titania Nanotubes: Novel Nanostructures for Improved Osseointegration. *J Heat Trans-T Asme* 2011, 133.
33. Balasundaram, G.; Webster, T. J., Nanotechnology and biomaterials for orthopedic medical applications. *Nanomedicine-Uk* 2006, 1, 169-176.
34. Friedrich, C. R.; Kolati, M.; Moser, T.; Sukotjo, C.; Shokuhfar, T., Survivability of TiO2 nanotubes on the surface of bone screws. *Surf Innov* 2014, 2, 60-68.
35. Brammer, K. S.; Frandsen, C. J.; Jin, S., TiO2 nanotubes for bone regeneration. *Trends Biotechnol* 2012, 30, 315-322.
36. Wang, F.; Shi, L.; He, W. X.; Han, D.; Yan, Y.; Niu, Z. Y.; Shi, S. G., Bioinspired micro/nano fabrication on dental implant-bone interface. *Appl Surf Sci* 2013, 265, 480-488.
37. Zhang, L. J.; Webster, T. J., Nanotechnology and nanomaterials: Promises for improved tissue regeneration. *Nano Today* 2009, 4, 66-80.
38. Mendonca, G.; Mendonca, D. B. S.; Aragao, F. J. L.; Cooper, L. F., Advancing dental implant surface technology - From micron- to nanotopography. *Biomaterials* 2008, 29, 3822-3835.
39. Li, Y.; Lee, I. S.; Cui, F. Z.; Choi, S. H., The biocompatibility of nanostructured calcium phosphate coated on micro-arc oxidized titanium. *Biomaterials* 2008, 29, 2025-2032.
40. Palin, E.; Liu, H. N.; Webster, T. J., Mimicking the nanofeatures of bone increases bone-forming cell adhesion and proliferation. *Nanotechnology* 2005, 16, 1828-1835.
41. Popat, K. C.; Eltgroth, M.; LaTempa, T. J.; Grimes, C. A.; Desai, T. A., Decreased Staphylococcus epidermis adhesion and increased osteoblast functionality on antibiotic-loaded titania nanotubes. *Biomaterials* 2007, 28, 4880-4888.
42. Dalby, M. J.; Gadegaard, N.; Oreffo, R. O. C., Harnessing nanotopography and integrin-matrix interactions to influence stem cell fate. *Nat Mater* 2014, 13, 558-569.
43. Oh, S.; Daraio, C.; Chen, L. H.; Pisanic, T. R.; Finones, R. R.; Jin, S., Significantly accelerated osteoblast cell growth on aligned TiO2 nanotubes. *Journal of Biomedical Materials Research Part A: An Official Journal of The Society for Biomaterials, The Japanese Society for Biomaterials, and The Australian Society for Biomaterials and the Korean Society for Biomaterials* 2006, 78, 97-103.
44. Adachi, M.; Murata, Y.; Harada, M.; Yoshikawa, S., Formation of titania nanotubes with high photo-catalytic activity. *Chem Lett* 2000, 942-943.
45. Gong, D.; Grimes, C. A.; Varghese, O. K.; Hu, W. C.; Singh, R. S.; Chen, Z.; Dickey, E. C., Titanium oxide nanotube arrays prepared by anodic oxidation. *J Mater Res* 2001, 16, 3331-3334.

46. Mohamed, A. E.; Rohani, S., Modified TiO2 nanotube arrays (TNTAs): progressive strategies towards visible light responsive photoanode, a review. *Energ Environ Sci* 2011, 4, 1065-1086.
47. Yin, H.; Liu, H.; Shen, W. Z., The large diameter and fast growth of self-organized TiO2 nanotube arrays achieved via electrochemical anodization. *Nanotechnology* 2010, 21.
48. Macak, J. M.; Schmuki, P., Anodic growth of self-organized anodic TiO2 nanotubes in viscous electrolytes. *Electrochim Acta* 2006, 52, 1258-1264.
49. Cai, Q. Y.; Paulose, M.; Varghese, O. K.; Grimes, C. A., The effect of electrolyte composition on the fabrication of self-organized titanium oxide nanotube arrays by anodic oxidation. *J Mater Res* 2005, 20, 230-236.
50. Yang, Y.; Wang, X. H.; Li, L. T., Synthesis and photovoltaic application of high aspect-ratio TiO2 nanotube arrays by anodization. *J Am Ceram Soc* 2008, 91, 3086-3089.
51. Shankar, K.; Mor, G. K.; Prakasam, H. E.; Yoriya, S.; Paulose, M.; Varghese, O. K.; Grimes, C. A., Highly-ordered TiO2 nanotube arrays up to 220 mu m in length: use in water photoelectrolysis and dye-sensitized solar cells. *Nanotechnology* 2007, 18.
52. Roy, P.; Berger, S.; Schmuki, P., TiO2 Nanotubes: Synthesis and Applications. *Angew Chem Int Edit* 2011, 50, 2904-2939.
53. Wang, D. A.; Yu, B.; Wang, C. W.; Zhou, F.; Liu, W. M., A Novel Protocol Toward Perfect Alignment of Anodized TiO2 Nanotubes. *Adv Mater* 2009, 21, 1964-1967.
54. Shin, D. H.; Shokuhfar, T.; Choi, C. K.; Lee, S. H.; Friedrich, C., Wettability changes of TiO2 nanotube surfaces. *Nanotechnology* 2011, 22.
55. Oh, S.; Brammer, K. S.; Li, Y. S. J.; Teng, D.; Engler, A. J.; Chien, S.; Jin, S., Stem cell fate dictated solely by altered nanotube dimension. *P Natl Acad Sci USA* 2009, 106, 2130-2135.
56. von der Mark, K.; Bauer, S.; Park, J.; Schmuki, P., Another look at "Stem cell fate dictated solely by altered nanotube dimension". *P Natl Acad Sci USA* 2009, 106, E60-E60.
57. Park, J.; Bauer, S.; von der Mark, K.; Schmuki, P., Nanosize and vitality: TiO2 nanotube diameter directs cell fate. *Nano Lett* 2007, 7, 1686-1691.
58. Peng, Z. X.; Ni, J. H.; Zheng, K.; Shen, Y. D.; Wang, X. Q.; He, G.; Jin, S. H.; Tang, T. T., Dual effects and mechanism of TiO2 nanotube arrays in reducing bacterial colonization and enhancing C3H10T1/2 cell adhesion. *Int J Nanomed* 2013, 8, 3093-3105.
59. Gongadze, E.; Kabaso, D.; Bauer, S.; Slivnik, T.; Schmuki, P.; van Rienen, U.; Iglic, A., Adhesion of osteoblasts to a nanorough titanium implant surface. *Int J Nanomed* 2011, 6, 1801-1816.
60. Wang, N.; Li, H. Y.; Lu, W. L.; Li, J. H.; Wang, J. S.; Zhang, Z. T.; Liu, Y. R., Effects of TiO2 nanotubes with different diameters on gene expression and osseointegration of implants in minipigs. *Biomaterials* 2011, 32, 6900-6911.

61. Salou, L.; Hoornaert, A.; Louarn, G.; Layrolle, P., Enhanced osseointegration of titanium implants with nanostructured surfaces: An experimental study in rabbits. *Acta Biomater* 2015, 11, 494-502.
62. Albu, S. P.; Ghicov, A.; Macak, J. M.; Hahn, R.; Schmuki, P., Self-organized, free-standing TiO2 nanotube membrane for flow-through photocatalytic applications. *Nano Lett* 2007, 7, 1286-1289.
63. Paulose, M.; Shankar, K.; Yoriya, S.; Prakasam, H. E.; Varghese, O. K.; Mor, G. K.; Latempa, T. A.; Fitzgerald, A.; Grimes, C. A., Anodic growth of highly ordered TiO2 nanotube arrays to 134 mu m in length. *J Phys Chem B* 2006, 110, 16179-16184.
64. Albu, S. P.; Ghicov, A.; Aldabergenova, S.; Drechsel, P.; LeClere, D.; Thompson, G. E.; Macak, J. M.; Schmuki, P., Formation of Double-Walled TiO2 Nanotubes and Robust Anatase Membranes. *Adv Mater* 2008, 20, 4135-+.
65. Yu, J. G.; Dai, G. P.; Cheng, B., Effect of Crystallization Methods on Morphology and Photocatalytic Activity of Anodized TiO2 Nanotube Array Films. *J Phys Chem C* 2010, 114, 19378-19385.
66. Wang, D. A.; Liu, L. F.; Zhang, F. X.; Tao, K.; Pippel, E.; Domen, K., Spontaneous Phase and Morphology Transformations of Anodized Titania Nanotubes Induced by Water at Room Temperature. *Nano Lett* 2011, 11, 3649-3655.
67. Hahn, R.; Schmidt-Stein, F.; Salonen, J.; Thiemann, S.; Song, Y. Y.; Kunze, J.; Lehto, V. P.; Schmuki, P., Semimetallic TiO2 Nanotubes. *Angew Chem Int Edit* 2009, 48, 7236-7239.
68. Schmidt-Stein, F.; Thiemann, S.; Berger, S.; Hahn, R.; Schmuki, P., Mechanical properties of anatase and semi-metallic TiO2 nanotubes. *Acta Mater* 2010, 58, 6317-6323.
69. Lai, M.; Cai, K. Y.; Zhao, L.; Chen, X. Y.; Hou, Y. H.; Yang, Z. X., Surface Functionalization of TiO2 Nanotubes with Bone Morphogenetic Protein 2 and Its Synergistic Effect on the Differentiation of Mesenchymal Stem Cells. *Biomacromolecules* 2011, 12, 1097-1105.
70. Gao, A.; Hang, R. Q.; Huang, X. B.; Zhao, L. Z.; Zhang, X. Y.; Wang, L.; Tang, B.; Ma, S. L.; Chu, P. K., The effects of titania nanotubes with embedded silver oxide nanoparticles on bacteria and osteoblasts. *Biomaterials* 2014, 35, 4223-4235.
71. Zhang, Y.; Lan, Z.; Bo, L.; Yong, H., Enhancement in Sustained Release of Antimicrobial Peptide from Dual-Diameter-Structured TiO2 Nanotubes for Long-Lasting Antibacterial Activity and Cytocompatibility. *Acs Appl Mater Inter* 2017, 9, 9449-9461.
72. Mookherjee, N.; Hancock, R. E. W., Cationic host defence peptides: Innate immune regulatory peptides as a novel approach for treating infections. *Cell Mol Life Sci* 2007, 64, 922-933.
73. Hilpert, K.; Elliott, M. R.; Volkmer-Engert, R.; Henklein, P.; Donini, O.; Zhou, Q.; Winkler, D. F. H.; Hancock, R. E. W., Sequence requirements and an optimization strategy for short antimicrobial peptides. *Chem Biol* 2006, 13, 1101-1107.
74. Cherkasov, A.; Hilpert, K.; Jenssen, H.; Fjell, C. D.; Waldbrook, M.; Mullaly, S. C.; Volkmer, R.; Hancock, R. E. W., Use of Artificial Intelligence in the Design of Small

Peptide Antibiotics Effective against a Broad Spectrum of Highly Antibiotic-Resistant Superbugs. *Acs Chem Biol* 2009, 4, 65-74.
75. Mani, G.; Johnson, D. M.; Marton, D.; Feldman, M. D.; Patel, D.; Ayon, A. A.; Agrawal, C. M., Drug delivery from gold and titanium surfaces using self-assembled monolayers. *Biomaterials* 2008, 29, 4561-4573.
76. Kokubun, K.; Matsumura, S.; Yudasaka, M.; Iijima, S.; Shiba, K., Immobilization of a carbon nanomaterial-based localized drug-release system using a bispecific material-binding peptide. *Int J Nanomed* 2018, 13, 1643-1652.
77. Peter, B.; Pioletti, D. P.; Laib, S.; Bujoli, B.; Pilet, P.; Janvier, P.; Guicheux, J.; Zambelli, P. Y.; Bouler, J. M.; Gauthier, O., Calcium phosphate drug delivery system: influence of local zoledronate release on bone implant osteointegration. *Bone* 2005, 36, 52-60.
78. Moseke, C.; Hage, F.; Vorndran, E.; Gbureck, U., TiO2 nanotube arrays deposited on Ti substrate by anodic oxidation and their potential as a long-term drug delivery system for antimicrobial agents. *Appl Surf Sci* 2012, 258, 5399-5404.
79. Peng, L. L.; Mendelsohn, A. D.; LaTempa, T. J.; Yoriya, S.; Grimes, C. A.; Desai, T. A., Long-Term Small Molecule and Protein Elution from TiO2 Nanotubes. *Nano Lett* 2009, 9, 1932-1936.
80. Wang, G. M.; Feng, H. Q.; Hu, L. S.; Jin, W. H.; Hao, Q.; Gao, A.; Peng, X.; Li, W.; Wong, K. Y.; Wang, H. Y.; Li, Z.; Chu, P. K., An antibacterial platform based on capacitive carbon-doped TiO2 nanotubes after direct or alternating current charging. *Nat Commun* 2018, 9.
81. Bauer, S.; Schmuki, P.; von der Mark, K.; Park, J., Engineering biocompatible implant surfaces Part I: Materials and surfaces. *Prog Mater Sci* 2013, 58, 261-326.
82. Lee, K.; Mazare, A.; Schmuki, P., One-Dimensional Titanium Dioxide Nanomaterials: Nanotubes. *Chem Rev* 2014, 114, 9385-9454.
83. Bauer, S.; Park, J.; von der Mark, K.; Schmuki, P., Improved attachment of mesenchymal stem cells on super-hydrophobic TiO2 nanotubes. *Acta Biomater* 2008, 4, 1576-1582.
84. Bauer, S.; Park, J.; Faltenbacher, J.; Berger, S.; von der Mark, K.; Schmuki, P., Size selective behavior of mesenchymal stem cells on ZrO2 and TiO2 nanotube arrays. *Integr Biol-Uk* 2009, 1, 525-532.
85. Park, J.; Bauer, S.; Schmuki, P.; von der Mark, K., Narrow Window in Nanoscale Dependent Activation of Endothelial Cell Growth and Differentiation on TiO2 Nanotube Surfaces. *Nano Lett* 2009, 9, 3157-3164.
86. Wooley, P. H.; Schwarz, E. M., Aseptic loosening. *Gene therapy* 2004, 11, 402-7.
87. Geetha, M.; Singh, A. K.; Asokamani, R.; Gogia, A. K., Ti based biomaterials, the ultimate choice for orthopaedic implants - A review. *Prog Mater Sci* 2009, 54, 397-425.
88. Raphel, J.; Holodniy, M.; Goodman, S. B.; Heilshorn, S. C., Multifunctional coatings to simultaneously promote osseointegration and prevent infection of orthopaedic implants. *Biomaterials* 2016, 84, 301-314.

89. Jin, Z.; Stone, M.; Ingham, E.; Fisher, J., (v) Biotribology. *Current Orthopaedics* 2006, 20, 32-40.
90. Yu, D. L.; Zhu, X. F.; Xu, Z.; Zhong, X. M.; Gui, Q. F.; Song, Y.; Zhang, S. Y.; Chen, X. Y.; Li, D. D., Facile Method to Enhance the Adhesion of TiO2 Nanotube Arrays to Ti Substrate. *Acs Appl Mater Inter* 2014, 6, 8001-8005.
91. Xiong, J. Y.; Wang, X. J.; Li, Y. C.; Hodgson, P. D., Interfacial Chemistry and Adhesion between Titanium Dioxide Nanotube Layers and Titanium Substrates. *J Phys Chem C* 2011, 115, 4768-4772.
92. Schwarz, E. M.; Lu, A. P.; Goater, J. J.; Benz, E. B.; Kollias, G.; Rosier, R. N.; Puzas, J. E.; O'Keefe, R. J., Tumor necrosis factor-alpha/nuclear transcription factor-kappa B signaling in periprosthetic osteolysis. *J Orthopaed Res* 2000, 18, 472-480.
93. Rader, C. P.; Sterner, T.; Jakob, F.; Schutze, N.; Eulert, J., Cytokine response of human macrophage-like cells after contact with polyethylene and pure titanium particles. *J Arthroplasty* 1999, 14, 840-848.
94. Gonzalez, J. E. G.; Mirza-Rosca, J. C., Study of the corrosion behavior of titanium and some of its alloys for biomedical and dental implant applications. *J Electroanal Chem* 1999, 471, 109-115.
95. Yu, W. Q.; Qiu, J.; Xu, L.; Zhang, F. Q., Corrosion behaviors of TiO2 nanotube layers on titanium in Hank's solution. *Biomed Mater* 2009, 4.
96. Saji, V. S.; Choe, H. C.; Brantley, W. A., An electrochemical study on self-ordered nanoporous and nanotubular oxide on Ti-35Nb-5Ta-7Zr alloy for biomedical applications. *Acta Biomater* 2009, 5, 2303-2310.
97. Choi, J. S.; Wehrspohn, R. B.; Lee, J.; Gosele, U., Anodization of nanoimprinted titanium: a comparison with formation of porous alumina. *Electrochim Acta* 2004, 49, 2645-2652.
98. Zhu, X. L.; Chen, J.; Scheideler, L.; Reichl, R.; Geis-Gerstorfer, J., Effects of topography and composition of titanium surface oxides on osteoblast responses. *Biomaterials* 2004, 25, 4087-4103.
99. Korduba, L. A.; Wang, A., The effect of cross-shear on the wear of virgin and highly-crosslinked polyethylene. *Wear* 2011, 271, 1220-1223.
100. Standard Test Method for Wear Testing with a Pin-on-Disk Apparatus ASTM G-99. 2016.
101. Vieira, A. C.; Ribeiro, A. R.; Rocha, L. A.; Celis, J. P., Influence of pH and corrosion inhibitors on the tribocorrosion of titanium in artificial saliva. *Wear* 2006, 261, 994-1001.
102. Jones, F. H., Teeth and bones: applications of surface science to dental materials and related biomaterials. *Surf Sci Rep* 2001, 42, 79-205.
103. Marino, C. E. B.; Mascaro, L. H., EIS characterization of a Ti-dental implant in artificial saliva media: dissolution process of the oxide barrier. *J Electroanal Chem* 2004, 568, 115-120.

104. Hacisalihoglu, I.; Samancioglu, A.; Yildiz, F.; Purcek, G.; Alsaran, A., Tribocorrosion properties of different type titanium alloys in simulated body fluid. *Wear* 2015, 332, 679-686.
105. Rho, J. Y.; Pharr, G. M., Effects of drying on the mechanical properties of bovine femur measured by nanoindentation. *Journal of materials science. Materials in medicine* 1999, 10, 485-8.
106. Parker, M. J.; Gurusamy, K. S., Internal fixation versus arthroplasty for intracapsular proximal femoral fractures in adults. *Cochrane Database of Systematic Reviews* 2006.
107. Han, S. K.; Song, H. S.; Kim, R.; Kang, S. H., Clinical results of treatment of garden type 1 and 2 femoral neck fractures in patients over 70-year old. *Eur J Trauma Emerg S* 2016, 42, 191-196.
108. Selvan, V. T.; Oakley, M. J.; Rangan, A.; Al-Lami, M. K., Optimum configuration of cannulated hip screws for the fixation of intracapsular hip fractures: a biomechanical study. *Injury-International Journal Of the Care Of the Injured* 2004, 35, 136-141.
109. Khoo, C.; Haseeb, A.; Ajit Singh, V., Cannulated Screw Fixation For Femoral Neck Fractures : A 5-year Experience In A Single Institution. *Malaysian orthopaedic journal* 2014, 8, 14-21.
110. Johansson, Å.; Strömqvist, B.; Bauer, G.; Hansson, L. I.; Pettersson, H., Improved operations for femoral neck fracture: a radiographic evaluation. *Acta orthopaedica Scandinavica* 1986, 57, 505-509.
111. Lindequist, S., Cortical screw support in femoral neck fractures: a radiographic analysis of 87 fractures with a new mensuration technique. *Acta orthopaedica Scandinavica* 1993, 64, 289-293.
112. Swiontkowski, M. F.; Harrington, R. M.; Keller, T. S.; Van Patten, P. K., Torsion and bending analysis of internal fixation techniques for femoral neck fractures: the role of implant design and bone density. *Journal of orthopaedic research* 1987, 5, 433-444.
113. Linke, B.; Schwieger, K.; Bursic, D.; Dutoit, C.; Ulrich, D.; Gautier, E. In *Treatment of unstable femoral neck fractures: is the dynamic hip screw a superior alternative to 3 cannulated screws*, Orthopaedic Trauma Association Annual Meeting (Poster 55), 2004; pp 403-407.
114. Madsen, F.; Linde, F.; Andersen, E.; Birke, H.; Hvass, I.; Poulsen, T. D., Fixation of displaced femoral neck fractures: a comparison between sliding screw plate and four cancellous bone screws. *Acta Orthopaedica Scandinavica* 1987, 58, 212-216.
115. Wu, C. C.; Chen, W. J., Minimally displaced intra-capsular femoral neck fractures in the elderly--comparison of multiple threaded pins and sliding compression screws surgical techniques. *Journal of orthopaedic surgery* 2003, 11, 129-36.
116. Rupprecht, M.; Grossterlinden, L.; Ruecker, A. H.; de Oliveira, A. N.; Sellenschloh, K.; Nuchtern, J.; Puschel, K.; Morlock, M.; Rueger, J. M.; Lehmann, W., A comparative biomechanical analysis of fixation devices for unstable femoral neck

fractures: the Intertan versus cannulated screws or a dynamic hip screw. *The Journal of trauma* 2011, 71, 625-34.
117. Lee, Y. S.; Chen, S. H.; Tsuang, Y. H.; Huang, H. L.; Lo, T. Y.; Huang, C. R., Internal fixation of undisplaced femoral neck fractures in the elderly: a retrospective comparison of fixation methods. *The Journal of trauma* 2008, 64, 155-62.
118. Bhandari, M.; Devereaux, P. J.; Swiontkowski, M. F.; Tornetta, P.; Obremskey, W.; Koval, K. J.; Nork, S.; Sprague, S.; Schemitsch, E. H.; Guyatt, G. H., Internal fixation compared with arthroplasty for displaced fractures of the femoral neck - A meta-analysis. *J Bone Joint Surg Am* 2003, 85A, 1673-1681.
119. Bosch, U.; Schreiber, T.; Krettek, C., Reduction and fixation of displaced intracapsular fractures of the proximal femur. *Clin Orthop Relat R* 2002, 59-71.
120. Goriainov, V.; Cook, R.; Latham, J. M.; Dunlop, D. G.; Oreffo, R. O. C., Bone and metal: An orthopaedic perspective on osseointegration of metals. *Acta Biomater* 2014, 10, 4043-4057.
121. Pommer, B.; Frantal, S.; Willer, J.; Posch, M.; Watzek, G.; Tepper, G., Impact of dental implant length on early failure rates: a meta-analysis of observational studies. *J Clin Periodontol* 2011, 38, 856-863.
122. Satterthwaite, J.; Rickman, L., Retrieval of a fractured abutment screw thread from an implant: A case report. *Brit Dent J* 2008, 204, 177-180.
123. Ibrahim, M. Z.; Sarhan, A. A. D.; Yusuf, F.; Hamdi, M., Biomedical materials and techniques to improve the tribological, mechanical and biomedical properties of orthopedic implants - A review article. *J Alloy Compd* 2017, 714, 636-667.
124. Rodrigues, D. C.; Urban, R. M.; Jacobs, J. J.; Gilbert, J. L., In Vivo Severe Corrosion and Hydrogen Embrittlement of Retrieved Modular Body Titanium Alloy Hip-Implants. *J Biomed Mater Res B* 2009, 88B, 206-219.
125. Tritschler, B.; Forest, B.; Rieu, J., Fretting corrosion of materials for orthopaedic implants: a study of a metal/polymer contact in an artificial physiological medium. *Tribol Int* 1999, 32, 587-596.
126. Geringer, J.; Forest, B.; Combrade, P., Fretting-corrosion of materials used as orthopaedic implants. *Wear* 2005, 259, 943-951.
127. Lukina, E.; Kollerov, M.; Meswania, J.; Khon, A.; Panin, P.; Blunn, G. W., Fretting corrosion behavior of nitinol spinal rods in conjunction with titanium pedicle screws. *Mat Sci Eng C-Mater* 2017, 72, 601-610.
128. Walker, P. R.; Leblanc, J.; Sikorska, M., Effects Of Aluminum And Other Cations on the Structure Of Brain And Liver Chromatin. *Biochemistry-Us* 1989, 28, 3911-3915.
129. Aragon, P. J.; Hulbert, S. F., Corrosion Of Ti-6a1-4v In Simulated Body-Fluids And Bovine Plasma. *J Biomed Mater Res* 1972, 6, 155-&.
130. Schutz, M.; Sudkamp, N. P., Revolution in plate osteosynthesis: new internal fixator systems. *Journal of orthopaedic science : official journal of the Japanese Orthopaedic Association* 2003, 8, 252-8.

131. Chen, C. S.; Chen, W. J.; Cheng, C. K.; Jao, S. H.; Chueh, S. C.; Wang, C. C., Failure analysis of broken pedicle screws on spinal instrumentation. *Medical engineering & physics* 2005, 27, 487-96.
132. Yokoyama, K.; Ichikawa, T.; Murakami, H.; Miyamoto, Y.; Asaoka, K., Fracture mechanisms of retrieved titanium screw thread in dental implant. *Biomaterials* 2002, 23, 2459-2465.
133. Azevedo, C. R. F., Failure analysis of a commercially pure titanium plate for osteosynthesis. *Eng Fail Anal* 2003, 10, 153-164.
134. Kaab, M. J.; Frenk, A.; Schmeling, A.; Schaser, K.; Schutz, M.; Haas, N. P., Locked internal fixator: sensitivity of screw/plate stability to the correct insertion angle of the screw. *Journal of orthopaedic trauma* 2004, 18, 483-7.
135. Patel, P. S.; Shepherd, D. E.; Hukins, D. W., The effect of screw insertion angle and thread type on the pullout strength of bone screws in normal and osteoporotic cancellous bone models. *Medical engineering & physics* 2010, 32, 822-8.
136. Gardner, M. J.; Brophy, R. H.; Campbell, D.; Mahajan, A.; Wright, T. M.; Helfet, D. L.; Lorich, D. G., The mechanical behavior of locking compression plates compared with dynamic compression plates in a cadaver radius model. *Journal of orthopaedic trauma* 2005, 19, 597-603.
137. Kanchanomai, C.; Phiphobmongkol, V.; Muanjan, P., Fatigue failure of an orthopedic implant - A locking compression plate. *Eng Fail Anal* 2008, 15, 521-530.
138. Goldberg, J. R.; Gilbert, J. L.; Jacobs, J. J.; Bauer, T. W.; Paprosky, W.; Leurgans, S., A multicenter retrieval study of the taper interfaces of modular hip prostheses. *Clin Orthop Relat R* 2002, 149-161.
139. Asri, R. I. M.; Harun, W. S. W.; Samykano, M.; Lah, N. A. C.; Ghani, S. A. C.; Tarlochan, F.; Raza, M. R., Corrosion and surface modification on biocompatible metals: A review. *Materials science & engineering. C, Materials for biological applications* 2017, 77, 1261-1274.
140. Koziolek, M.; Grimm, M.; Becker, D.; Iordanov, V.; Zou, H.; Shimizu, J.; Wanke, C.; Garbacz, G.; Weitschies, W., Investigation of pH and Temperature Profiles in the GI Tract of Fasted Human Subjects Using the Intellicap((R)) System. *Journal of pharmaceutical sciences* 2015, 104, 2855-63.
141. Jones, R. L.; Wing, S. S.; Syrett, B. C., Stress-Corrosion Cracking And Corrosion Fatigue Of Some Surgical Implant Materials In a Physiological Saline Environment. *Corrosion* 1978, 34, 226-236.
142. Bundy, K. J.; Marek, M.; Hochman, R. F., In vivo and in vitro studies of the stress-corrosion cracking behavior of surgical implant alloys. *J Biomed Mater Res* 1983, 17, 467-87.
143. Cserhati, P.; Kazar, G.; Manninger, J.; Fekete, K.; Frenyo, S., Non-operative or operative treatment for undisplaced femoral neck fractures: a comparative study of 122 non-operative and 125 operatively treated cases. *Injury* 1996, 27, 583-8.

144. Haidukewych, G. J.; Rothwell, W. S.; Jacofsky, D. J.; Torchia, M. E.; Berry, D. J., Operative treatment of femoral neck fractures in patients between the ages of fifteen and fifty years. *J Bone Joint Surg Am* 2004, 86-A, 1711-6.
145. Rogmark, C.; Flensburg, L.; Fredin, H., Undisplaced femoral neck fractures--no problems? A consecutive study of 224 patients treated with internal fixation. *Injury* 2009, 40, 274-6.
146. Angelini, M.; McKee, M. D.; Waddell, J. P.; Haidukewych, G.; Schemitsch, E. H., Salvage of failed hip fracture fixation. *Journal of orthopaedic trauma* 2009, 23, 471-8.
147. Lakkol, S.; Boddu, K.; Buckle, C.; Kavarthapu, V.; Li, P. In *SIGNIFICANT FIXATION FAILURE IN INTERNAL FIXATION OF UNDISPLACED INTRACAPSULAR HIP FRACTURE*, Orthopaedic Proceedings, The British Editorial Society of Bone & Joint Surgery: 2014; pp 17-17.
148. Manohara, R.; Liang, S.; Huang, D.; Krishna, L., Cancellous screw fixation for undisplaced femoral neck fractures in the elderly. *Journal of orthopaedic surgery* 2014, 22, 282-6.
149. Della Valle, C.; Parvizi, J.; Bauer, T. W.; Dicesare, P. E.; Evans, R. P.; Segreti, J.; Spangehl, M.; Watters, W. C., 3rd; Keith, M.; Turkelson, C. M.; Wies, J. L.; Sluka, P.; Hitchcock, K.; American Academy of Orthopaedic, S., Diagnosis of periprosthetic joint infections of the hip and knee. *The Journal of the American Academy of Orthopaedic Surgeons* 2010, 18, 760-70.
150. Thiele, O. C.; Eckhardt, C.; Linke, B.; Schneider, E.; Lill, C. A., Factors affecting the stability of screws in human cortical osteoporotic bone: a cadaver study. *J Bone Joint Surg Br* 2007, 89, 701-5.
151. Swiontkowski, M. F.; Harrington, R. M.; Keller, T. S.; Van Patten, P. K., Torsion and bending analysis of internal fixation techniques for femoral neck fractures: the role of implant design and bone density. *Journal of orthopaedic research : official publication of the Orthopaedic Research Society* 1987, 5, 433-44.
152. Filipov, O.; Gueorguiev, B., Unique stability of femoral neck fractures treated with the novel biplane double-supported screw fixation method: a biomechanical cadaver study. *Injury* 2015, 46, 218-26.
153. Walker, E.; Mukherjee, D. P.; Ogden, A. L.; Sadasivan, K. K.; Albright, J. A., A biomechanical study of simulated femoral neck fracture fixation by cannulated screws: effects of placement angle and number of screws. *American journal of orthopedics* 2007, 36, 680-4.
154. Neoh, K. G.; Hu, X.; Zheng, D.; Kang, E. T., Balancing osteoblast functions and bacterial adhesion on functionalized titanium surfaces. *Biomaterials* 2012, 33, 2813-22.
155. Rho, J. Y.; Ashman, R. B.; Turner, C. H., Young's modulus of trabecular and cortical bone material: ultrasonic and microtensile measurements. *Journal of biomechanics* 1993, 26, 111-9.

156. Macak, J. M.; Tsuchiya, H.; Taveira, L.; Ghicov, A.; Schmuki, P., Self-organized nanotubular oxide layers on Ti-6Al-7Nb and Ti-6Al-4V formed by anodization in NH4F solutions. *J Biomed Mater Res A* 2005, 75, 928-33.
157. Ward, B. C.; Webster, T. J., The effect of nanotopography on calcium and phosphorus deposition on metallic materials in vitro. *Biomaterials* 2006, 27, 3064-74.
158. Goodman, S. B., Wear particles, periprosthetic osteolysis and the immune system. *Biomaterials* 2007, 28, 5044-5048.
159. Barril, S.; Debaud, N.; Mischler, S.; Landolt, D., A tribo-electrochemical apparatus for in vitro investigation of fretting-corrosion of metallic implant materials. *Wear* 2002, 252, 744-754.
160. Stevens, M. M.; George, J. H., Exploring and engineering the cell surface interface. *Science* 2005, 310, 1135-1138.
161. Bonnans, C.; Chou, J.; Werb, Z., Remodelling the extracellular matrix in development and disease. *Nature reviews. Molecular cell biology* 2014, 15, 786-801.
162. Sanz-Herrera, J. A.; Reina-Romo, E., Cell-biomaterial mechanical interaction in the framework of tissue engineering: insights, computational modeling and perspectives. *International journal of molecular sciences* 2011, 12, 8217-8244.
163. Smeets, R.; Kolk, A.; Gerressen, M.; Driemel, O.; Maciejewski, O.; Hermanns-Sachweh, B.; Riediger, D.; Stein, J. M., A new biphasic osteoinductive calcium composite material with a negative Zeta potential for bone augmentation. *Head & face medicine* 2009, 5, 13.
164. Monsees, T. K.; Barth, K.; Tippelt, S.; Heidel, K.; Gorbunov, A.; Pompe, W.; Funk, R. H. W., Effects of different titanium alloys and nanosize surface patterning on adhesion, differentiation, and orientation of osteoblast-like cells. *Cells Tissues Organs* 2005, 180, 81-95.
165. Ngandu Mpoyi, E.; Cantini, M.; Reynolds, P. M.; Gadegaard, N.; Dalby, M. J.; Salmerón-Sánchez, M., Protein adsorption as a key mediator in the nanotopographical control of cell behavior. *Acs Nano* 2016, 10, 6638-6647.
166. Dalby, M. J.; García, A. J.; Salmeron-Sanchez, M., Receptor control in mesenchymal stem cell engineering. *Nature Reviews Materials* 2018, 3, 17091.
167. Cavalcanti-Adam, E. A.; Aydin, D.; Hirschfeld-Warneken, V. C.; Spatz, J. P., Cell adhesion and response to synthetic nanopatterned environments by steering receptor clustering and spatial location. *HFSP journal* 2008, 2, 276-85.
168. Cavalcanti-Adam, E. A.; Volberg, T.; Micoulet, A.; Kessler, H.; Geiger, B.; Spatz, J. P., Cell spreading and focal adhesion dynamics are regulated by spacing of integrin ligands. *Biophys J* 2007, 92, 2964-2974.
169. Bershadsky, A.; Tint, I.; Neyfakh Jr, A.; Vasiliev, J., Focal contacts of normal and RSV-transformed quail cells: Hypothesis of the transformation-induced deficient maturation of focal contacts. *Experimental cell research* 1985, 158, 433-444.
170. Biggs, M. J.; Richards, R. G.; Gadegaard, N.; Wilkinson, C. D.; Oreffo, R. O.; Dalby, M. J., The use of nanoscale topography to modulate the dynamics of adhesion formation in primary osteoblasts and ERK/MAPK signalling in STRO-1+ enriched skeletal stem cells. *Biomaterials* 2009, 30, 5094-5103.

171. Kanchanawong, P.; Shtengel, G.; Pasapera, A. M.; Ramko, E. B.; Davidson, M. W.; Hess, H. F.; Waterman, C. M., Nanoscale architecture of integrin-based cell adhesions. *Nature* 2010, 468, 580-4.
172. McBeath, R.; Pirone, D. M.; Nelson, C. M.; Bhadriraju, K.; Chen, C. S., Cell shape, cytoskeletal tension, and RhoA regulate stem cell lineage commitment. *Developmental cell* 2004, 6, 483-95.
173. Kilian, K. A.; Bugarija, B.; Lahn, B. T.; Mrksich, M., Geometric cues for directing the differentiation of mesenchymal stem cells. *Proceedings of the National Academy of Sciences* 2010, 107, 4872-4877.
174. Dalby, M. J.; Gadegaard, N.; Tare, R.; Andar, A.; Riehle, M. O.; Herzyk, P.; Wilkinson, C. D.; Oreffo, R. O., The control of human mesenchymal cell differentiation using nanoscale symmetry and disorder. *Nat Mater* 2007, 6, 997-1003.
175. Tsimbouri, P. M.; McMurray, R. J.; Burgess, K. V.; Alakpa, E. V.; Reynolds, P. M.; Murawski, K.; Kingham, E.; Oreffo, R. O.; Gadegaard, N.; Dalby, M. J., Using nanotopography and metabolomics to identify biochemical effectors of multipotency. *Acs Nano* 2012, 6, 10239-10249.
176. Sjöström, T.; McNamara, L. E.; Meek, R. D.; Dalby, M. J.; Su, B., 2D and 3D nanopatterning of titanium for enhancing osteoinduction of stem cells at implant surfaces. *Advanced healthcare materials* 2013, 2, 1285-1293.
177. Le Guehennec, L.; Lopez-Heredia, M. A.; Enkel, B.; Weiss, P.; Amouriq, Y.; Layrolle, P., Osteoblastic cell behaviour on different titanium implant surfaces. *Acta Biomater* 2008, 4, 535-543.
178. Cooper, L. F.; Masuda, T.; Yliheikkila, P. K.; Felton, D. A., Generalizations regarding the process and phenomenon of osseointegration. Part II. In vitro studies. *Int J Oral Max Impl* 1998, 13, 163-174.
179. Anselme, K., Osteoblast adhesion on biomaterials. *Biomaterials* 2000, 21, 667-681.
180. Taipale, J.; KeskiOja, J., Growth factors in the extracellular matrix. *Faseb J* 1997, 11, 51-59.
181. Puckett, S.; Pareta, R.; Webster, T. J., Nano rough micron patterned titanium for directing osteoblast morphology and adhesion. *Int J Nanomedicine* 2008, 3, 229-41.

Bibliography

►Guang Wu, **Jiajun Luo (co-first author)** Hongze Liang, Yinghua Yan, Chaozong Liu, Hui Tan, Lingling Zhao*, 'Nanoparticle Enhanced Bamboo-like Tubular Nanofibers for Active Capture of Particulate Matter', *Journal of Polymer Science Part A* (2019), 57(11): 1216-1223. Published.

►**Jiajun Luo**, Bianhong Li, Sara Ajami, Shuanhong Ma*, Feng Zhou, Chaozong Liu*, 'Engineering Interface-Bonded Ti-TiO_2 Nanotubes with Enhanced Wear Resistance & Corrosion Resistance', *Journal of Bionic Engineering* (2019), Accepted.

►**Jiajun Luo**, Shudong Zhao, Xiangsheng Gao, Chaozong Liu*, 'Effects of Fibronectin Adsorption on Osteoblast Attachment on Nanoflat, Nanoconvex and Nanocave', *Nature Communications*, In draft.

►**Jiajun Luo**, Changyou Yan, Maryam Tamaddon, Shuanhong Ma*, Xiaolong Wang, Feng Zhou, Chaozong Liu*, 'Improving the Fretting Wear & Corrosion Behavior of Ti_6Al_4V Bone screw by Decorating Structure Optimised TiO_2 Nanotubes Layer', *Journal of Materials Science & Technology* (2019), Accepted.

►**Jiajun Luo**, Sara Ajami, Shuanhong Ma, Shen-Mao Chen, Feng Zhou*, Hai-Ming Yu*, Pei-Wen Wang, Xue-Dong Yao, Chaozong Liu*, 'Fretting Corrosion of Screws Contribute to the Fixation Failure of Femoral Neck A Case Report', *Biosurface and Biotribology* (2019), Accepted.

►**Jiajun Luo**, Changyou Yan, Sara Ajami, Shen-Mao Chen, Shuanhong Ma, Xiaolong Wang, Feng Zhou*, Hai-Ming Yu*, Pei-Wen Wang, Xue-Dong Yao,

Chaozong Liu*, 'Fatigue Accessment of Retrieval Fractured Cortical Bone Screw', *Journal of Biomedical research part B: Applied Biomaterials* (2019), In draft.

►Luyao Gao, Shuanhong Ma*, **Jiajun Luo**, Guangjie Bao, Yang Wu, Feng Zhou, Yongmin Liang, 'Synthesizing Functional Biomacromolecular Wet Adhesive with Typical Gel-Sol Transition and Shear-Thinning Features', *ACS Biomaterials Science & Engineering* (2019), Accepted.

►Feng Zhou, **Jiajun Luo**, Shuanhong Ma, Chaozong Liu, 'A Method of Improve Mechanical Stability on Ti Based Medical Alloy by Anodisation', Chinese Patent(2018), (Application No.CN201810487868.7)

►Feng Zhou, **Jiajun Luo**, Shuanhong Ma, Chaozong Liu, 'A Method of Test Fretting Behavior of Orthopaedic Bone Screws', Chinese Patent(2019), (In Progress)